NASA/CR-2014-218258

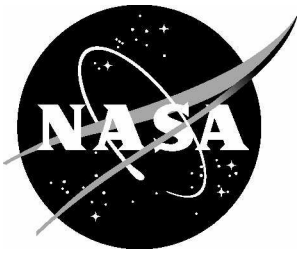

CFD Analysis of Flexible Thermal Protection System Shear Configuration Testing in the LCAT Facility

Paul G. Ferlemann
Analytical Mechanics Associates, Inc., Hampton, Virginia

May 2014

NASA STI Program . . . in Profile

Since its founding, NASA has been dedicated to the advancement of aeronautics and space science. The NASA scientific and technical information (STI) program plays a key part in helping NASA maintain this important role.

The NASA STI program operates under the auspices of the Agency Chief Information Officer. It collects, organizes, provides for archiving, and disseminates NASA's STI. The NASA STI program provides access to the NASA Aeronautics and Space Database and its public interface, the NASA Technical Report Server, thus providing one of the largest collections of aeronautical and space science STI in the world. Results are published in both non-NASA channels and by NASA in the NASA STI Report Series, which includes the following report types:

- TECHNICAL PUBLICATION. Reports of completed research or a major significant phase of research that present the results of NASA programs and include extensive data or theoretical analysis. Includes compilations of significant scientific and technical data and information deemed to be of continuing reference value. NASA counterpart of peer-reviewed formal professional papers, but having less stringent limitations on manuscript length and extent of graphic presentations.

- TECHNICAL MEMORANDUM.
  Scientific and technical findings that are preliminary or of specialized interest, e.g., quick release reports, working papers, and bibliographies that contain minimal annotation. Does not contain extensive analysis.

- CONTRACTOR REPORT.
  Scientific and technical findings by NASA-sponsored contractors and grantees.

- CONFERENCE PUBLICATION.
  Collected papers from scientific and technical conferences, symposia, seminars, or other meetings sponsored or co-sponsored by NASA.

- SPECIAL PUBLICATION.
  Scientific, technical, or historical information from NASA programs, projects, and missions, often concerned with subjects having substantial public interest.

- TECHNICAL TRANSLATION.
  English-language translations of foreign scientific and technical material pertinent to NASA's mission.

Specialized services also include organizing and publishing research results, distributing specialized research announcements and feeds, providing information desk and personal search support, and enabling data exchange services.

For more information about the NASA STI program, see the following:

- Access the NASA STI program home page at *http://www.sti.nasa.gov*

- E-mail your question to help@sti.nasa.gov

- Fax your question to the NASA STI Information Desk at 443-757-5803

- Phone the NASA STI Information Desk at 443-757-5802

- Write to:
  STI Information Desk
  NASA Center for AeroSpace Information
  7115 Standard Drive
  Hanover, MD 21076-1320

NASA/CR-2014-218258

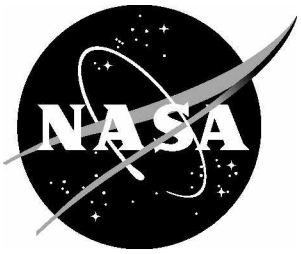

CFD Analysis of Flexible Thermal Protection System Shear Configuration Testing in the LCAT Facility

Paul G. Ferlemann
Analytical Mechanics Associates, Inc., Hampton, Virginia

National Aeronautics and
Space Administration

Langley Research Center
Hampton, Virginia 23681-2199

Prepared for Langley Research Center
under Contract NNL12AA09C

May 2014

Available from:

NASA Center for AeroSpace Information
7115 Standard Drive
Hanover, MD 21076-1320
443-757-5802

Introduction

NASA has interest in technologies for aerodynamically assisted deceleration of high-mass entry vehicles. Typical entry vehicle aeroshells are limited in size by the launch vehicle shroud. In contrast, a hypersonic inflatable aerodynamic decelerator (HIAD) is a concept which can be packed in a stowed configuration. [1] "Prior to atmospheric entry, the HIAD is deployed to produce a drag device many times larger than the launch shroud diameter. The large surface area of the inflatable aeroshell provides deceleration of high-mass entry vehicles at relatively low ballistic coefficients. Even for these low ballistic coefficients there is still appreciable heating, requiring the HIAD to employ a thermal protection system (TPS). This TPS must be capable of surviving the heat pulse, and the rigors of fabrication handling, high density packing, deployment, and aerodynamic loading." [2]

Prior to flight testing, ground testing and analysis were necessary to characterize the performance of various flexible TPS (FTPS) candidates. Test techniques have been developed and FTPS tests have been performed in the 8-Foot High Temperature Tunnel (8' HTT) at NASA Langley Research Center, the Laser Hardened Materials Evaluation Laboratory (LHMEL) at Wright-Patterson Air Force Base, and the Panel Test Facility (PTF) at NASA Ames Research Center. These testing efforts, including overviews of the facilities and selected results, are presented in [3]. This reference also identified the Boeing Large Core Arc Tunnel (LCAT) as an attractive facility in terms of aerothermal performance (heat flux, surface pressure, and aerodynamic shear force) and presented predicted aerothermal performance envelopes relevant to HIAD flight trajectories. An overview of the LCAT facility, test conditions and methodology, and selected thermal results of several FTPS layups are presented in [4].

This paper documents results of computational analysis performed after the shear (wedge) configuration tests. The primary objectives were to predict the shear force on the sample and the sensitivity of all surface properties to the shape of the sample. Bumps of 0.05, 0.10, and 0.15 inches were created to approximate the shape of some fabric samples during testing. A large amount of information was extracted from the CFD solutions for comparison between runs and also current or future flight simulations.

Geometry

The only geometry provided was for the circular to semi-elliptical facility throat section, shown in Figures 1 and 2. The circular entrance has a diameter of 1.5 inches. The throat has an area of 0.785 square inches. The geometry for the facility nozzle expansion section, test cabin, and sample holder was created in Pointwise as part of the grid generation process. The facility nozzle expansion section has a flat bottom wall, 5.1 degree vertical expansion on the top wall, a lateral divergence half-angle of 10 degrees, and an exit area of 10.24 square inches. The 4 inch square fabric samples were mounted 2 inches from the leading edge of a 9 inch wide by 11 inch long flat plate. An all metal calibration plate of the same dimensions was instrumented with 9 pressure taps and 9 heat flux gauges. The square leading edge of the plate was 0.150 inches downstream of the nozzle exit and 0.050 inches below the nozzle bottom wall. However, a compression wave was generated for the current runs since the plate was mounted at 2.5 degrees relative to the bottom wall of the nozzle.

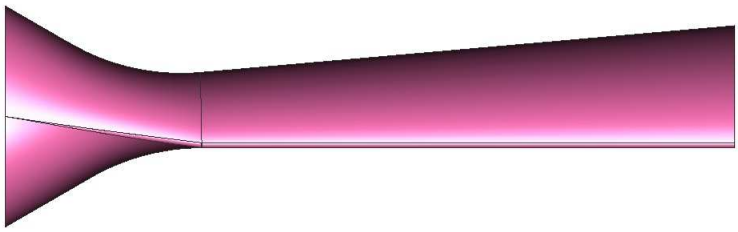

Figure 1: Side view of facility nozzle throat section.

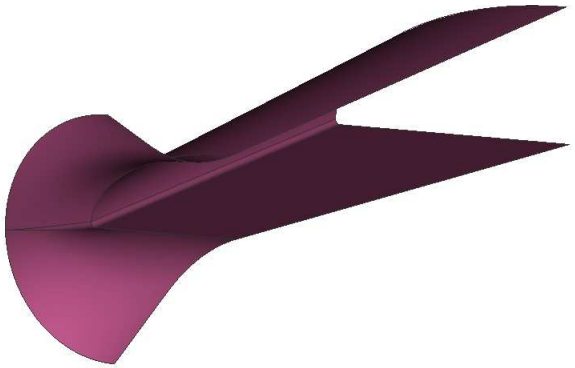

Figure 2: Three dimensional view of facility nozzle throat section.

Grid Generation

Since the VULCAN [5-6] CFD code was selected (based on prior experience and confidence predicting attached turbulent hypersonic boundary layers), a structured grid was required. Pointwise was used as the grid generation software.[7] Fortunately, the facility nozzle and sample holder were straightforward to grid. However, a non-C0 patch was used to change the grid topology between the exit of the facility nozzle and the leading edge of the calibration plate. This facilitated a wrapping grid in the nozzle and a nearly orthogonal grid above the calibration plate. The only other complication was determining the test cabin volume which needed to be modeled. For the calibration plate a nominal streamwise grid spacing of 0.05 inches was used. This produced 216 cells along the length of the plate. Laterally the grid spacing varied from 0.05 inches at the edge of the plate to 0.1 inches at the centerline. This produced 64 cells for the half-width. Above the plate 164 cells were used to cover 10.26 inches. The wall clustering spacings were 0.005 inches and 0.02 inches, at the beginning and end of the plate, respectively. With the use of the hyperbolic tangent stretching function, this resulted in 24 to 40 cells in the boundary layer above the FTPS sample area for all cases. For a cold wall it also produced a y-plus range from 9.4 to 37 above the sample area. The grid for the facility nozzle had 1.69 million cells and the calibration plate/test cabin section had 4.43 million cells. While the level of boundary layer resolution was believed to be sufficient, no formal grid convergence study was performed.

In addition to a flat surface to model the metal calibration plate, 3 bumps were created to approximate the shape of FTPS samples during testing. Various layups and materials pillowed out to different levels as they became hot. For grid generation, these were generated with parabolic curves parallel to the flat plate at the center of the sample and with the intersection of the start and end point tangents at 25% and 75% of the sample length. Bumps with a center height of 0.05, 0.10, and 0.15 inches were created.

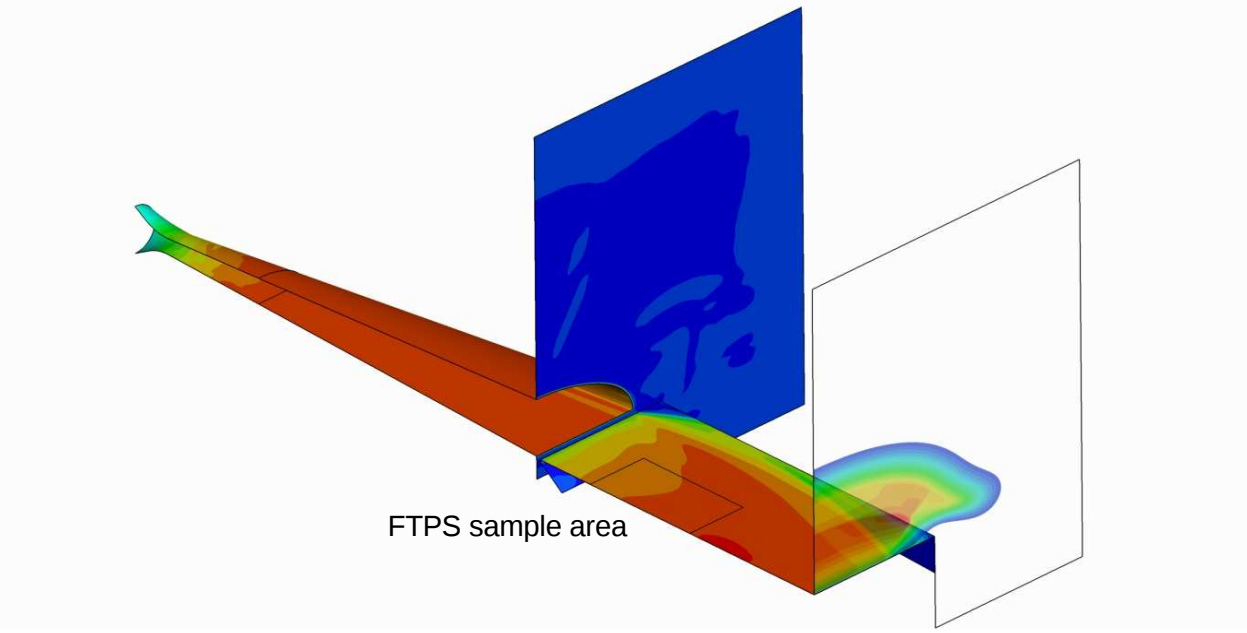

Figure 3: Computational domain for FTPS (shear configuration) testing in the LCAT facility.

Computational Model

The computational domain is shown in Figure 3 and assumed spanwise symmetry. The flow was assumed to be turbulent thermally perfect air. The Menter baseline turbulence model was used with wall matching functions. The facility nozzle was solved with isothermal walls at 500 °F. The facility nozzle was solved in 2 sections with an elliptic solution approach used for the throat section and a space marching approach used for the expansion section. The test cabin section was solved in a separate calculation. This facilitated the reuse of the facility nozzle exit plane for multiple simulations of the sample holder. A wall temperature of 80 °F was used for the water cooled calibration plate. For all cases the subsonic outflow pressure into the test cabin was set at 22 Torr (0.425 psi, 2933 kPa). The figure shows the modeled extent of the test cabin and the supersonic region of the plume at the end of the calibration plate. Solutions were converged to a steady state (total heat load not changing) using Edward's low dissipation flux split scheme and the diagonalized approximate factorization solver. Each solution of the sample holder region required approximately 20 hours with 14 processors.

Determination of Inflow Conditions

Ideally, all provided experimental boundary condition information would be applicable to the computational model. This information included: air mass flow, static pressure at the most upstream wall of the heater, calculated facility nozzle exit average flow total enthalpy, and measured static pressure and cold wall heat flux on the calibration plate. However, the flow entering the converging section of the facility throat section is likely complex with a swirl component and flow profiles which vary with arc power and facility configuration. With the time and resources available, the simplest modeling approach was selected to maximize confidence in the calculated shear to the sample area. Therefore, only the calibration plate (center) pressure and heat flux measurements were used to determine uniform facility plenum conditions for the computational model. This required between 3 and 7 iterations in order to match the pressure and heat flux data. More complex facility nozzle inflow conditions and thermal boundary conditions which produce the same calibration plate pressure and heat flux would be expected to

have a relatively small affect on the predicted wall shear. Therefore, the intent was not to predict the calibration plate data given the available facility nozzle conditions, but rather to use the calibration data to determine the facility inflow conditions required by the numerical model and then investigate trends with test condition, variations in loads over the FTPS sample area and sensitivities to the FTPS shape and surface temperature.

General Flow Characteristics

Two photographs of the flow over different FTPS samples are shown in Figure 4. A shock wave is created at the leading edge of the sample holder since it was at 2.5 degrees relative to the bottom surface of the facility nozzle. Shock waves are also created at the beginning and end of the FTPS sample. Computational images of the flow structure at the centerline based on density gradients are also included. Of course, the strength of the shock wave from the sample increases as the bump height increases.

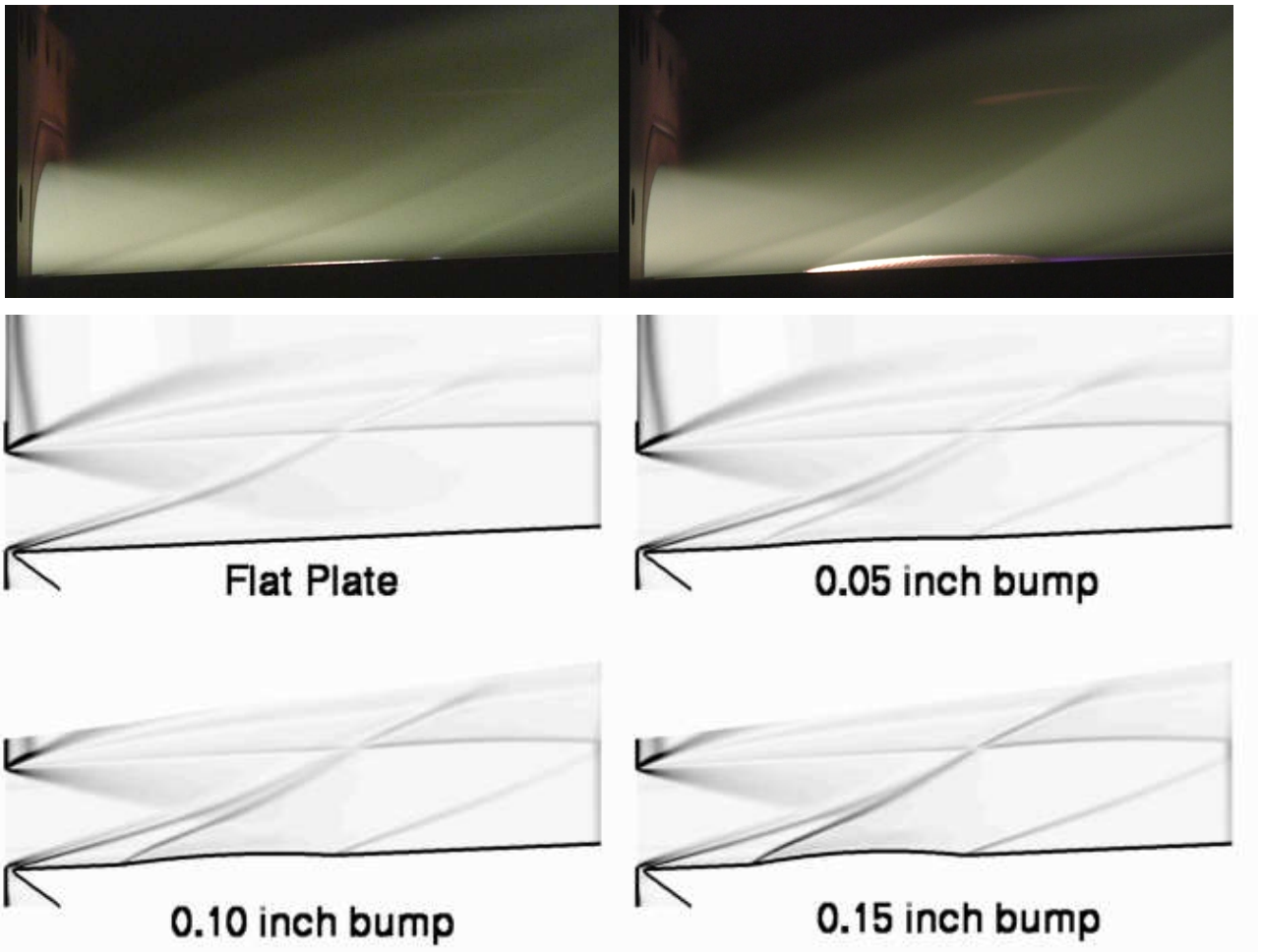

Figure 4: Photographs of flow during testing and contours of computational density gradients.

The accompanying Mach number contours at the centerline are shown in Figure 5. The flux-conservative one-dimensional facility nozzle exit Mach number was 3.27. The expansion fan from the top of the facility nozzle reaches the plate near the end of the FTPS sample area. Contours in a crossflow plane at the center of the sample are included in Figure 6. The plume covers the entire width of the 9 inch wide calibration plate (or 11.43 cm half-width). The Mach number at the boundary layer edge is shown in Figure 7 and varies from 3.4 to 4.1 over the sample area.

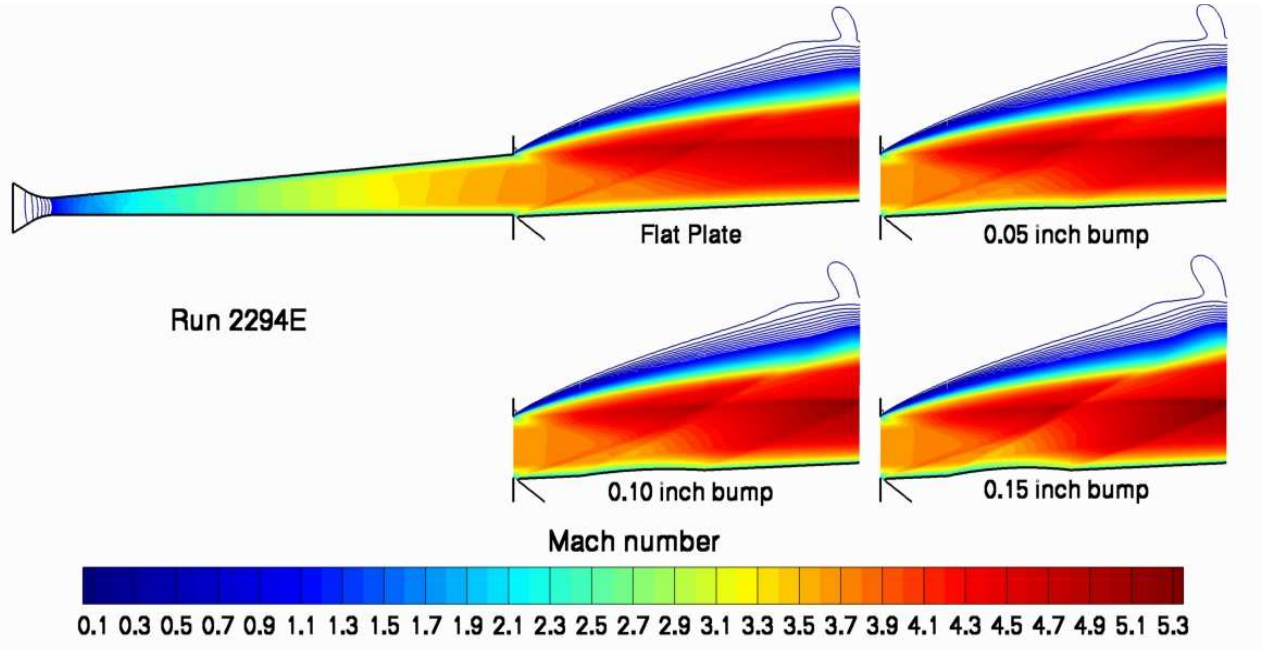

Figure 5: Centerline Mach number contours.

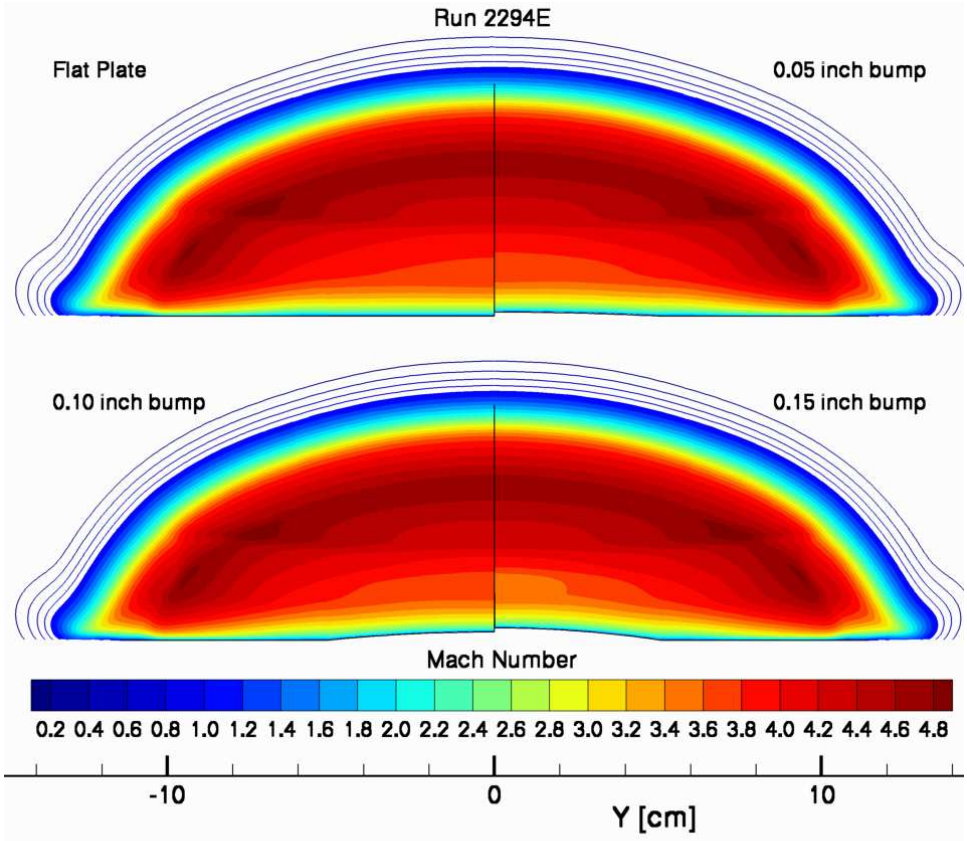

Figure 6: Mach number contours in a crossflow plane at the center of the sample area.

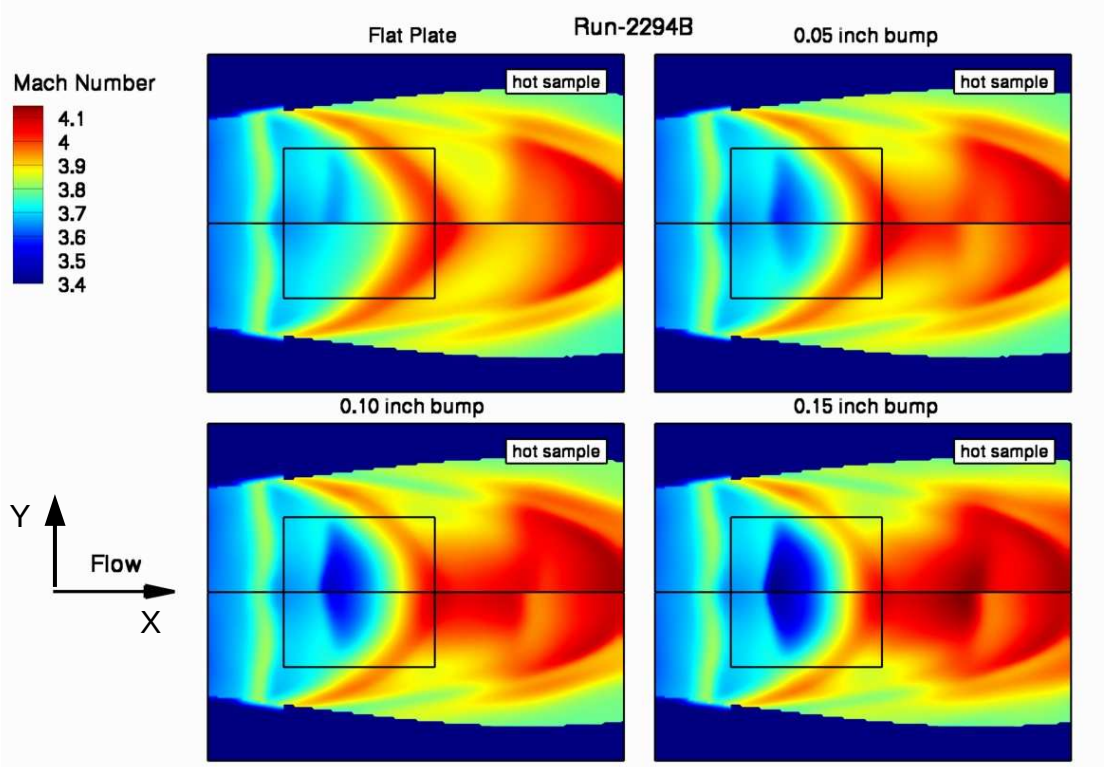

Figure 7: Boundary layer edge Mach number variation (square FTPS sample area shown).

Test Conditions [4]

The HIAD project has invested in ground tests to evaluate the aerothermal performance of various FTPS candidates for use in inflatable high-drag, down-mass technology. In the LCAT test series, material layups were subjected to aerothermal loads commensurate with peak re-entry conditions enveloping a range of HIAD mission trajectories. Four test conditions were calibrated in the LCAT facility for both shear and stagnation testing to provide a range of conditions for evaluating the FTPS. These conditions included peak heating rates above the unmargined smooth wall maximum heating prediction. This was done to account for increased localized heating which could result from geometry variations resulting from the underlying structural support, surface features such as seams and penetrations, and surface distortions resulting from wrinkles or other surface imperfections. The calibrated test conditions are listed in Table 1 (actual test conditions slightly different). This document includes results for the first three conditions since the shear configuration was not tested at the 50 W/cm^2 condition.

Table 1: Calibrated LCAT shear configuration cold wall heat flux and surface pressure conditions.

Heat Flux (W/cm^2)	Surface Pressure (kPa)
20	3.1
30	4.8
40	6.6
50	4.0

Results for Run 2294B

The experimental and computational conditions for the 3.1 kPa / 20 W/cm^2 target condition are listed in Table 2. Although the nozzle exit enthalpy matched reasonably well, the computational model required 73% of the reported mass flow in order to match the calibration plate data. A flat, cold wall shear of 113 Pa at the center of the sample area was predicted for this test condition.

Table 2: Facility and calibration plate information for Run 2294B.

	Plenum Pressure (kPa)	Total Air Flow (kg/s)	Nozzle Exit Enthalpy (MJ/kg)	At Center of Calibration Plate		
				Pressure (kPa)	Heat Flux (W/cm^2)	Shear (Pa)
Experiment	608[a]	0.179	5.234	3.03	20.1	N/A
CFD Model	445[b]	0.131	5.254			113

a.) at most upstream wall of heater.

b.) at entrance to facility nozzle throat section.

Comparisons with the experimental pressure data are shown in Figures 8 and 9. As intended, the CFD matches the center value (at X=10.160 cm, Y=1.016 cm). With streamwise distance, the CFD predicts a decreasing pressure with the same slope off-centerline. (The data at Y=1.016 cm will be referred to as the "centerline" pressure results.) The expansion wave from the top of the facility nozzle exit changes the slope of the prediction and affects the outboard regions of the sample area before the centerline. The centerline experimental data indicates a significantly lower slope. The CFD predicts a fairly uniform pressure laterally across the sample area. For the first two streamwise locations, the data indicates higher pressure on both sides of the centerline (slightly higher on the positive Y side).

Comparisons with the experimental heat flux data are shown in Figures 10 and 11. As intended, the CFD matches the center value. Except for one data point, the CFD matches the data at the first two streamwise locations fairly well. However, the CFD prediction continues to decrease, while the data at X=13.335 cm is only slightly less than the data at X=10.160 cm. Therefore, the data near the end of the sample region is under-predicted. The measured heat flux is higher on the positive Y side of the sample area at each axial location.

The same facility nozzle exit flow was used to perform seven more simulations. These included the flat plate solved with a zero heat flux boundary condition rather than a specified cold wall temperature, then three bump heights each solved with a cold and hot (adiabatic) wall.

Figure 12 shows the pressure variation over the sample holder. Surface streamlines are also included. Except for the corners at the end of the sample region, the CFD predicts nearly constant pressure laterally, but monotonically decreasing pressure axially for the sample area of the flat calibration plate. The introduction of a bump creates higher pressure on the front of the bump and lower pressure on the back. It also creates a large lateral variation, particularly at the front of the bump.

The heat flux variation over the sample holder is shown in Figure 13. While the heat flux down the centerline is the highest, the lateral variation is small compared to the streamwise variation. Of course, compared to the flat plate the introduction of a bump increases the heat flux to the first half of the sample area and decreases it to the second half.

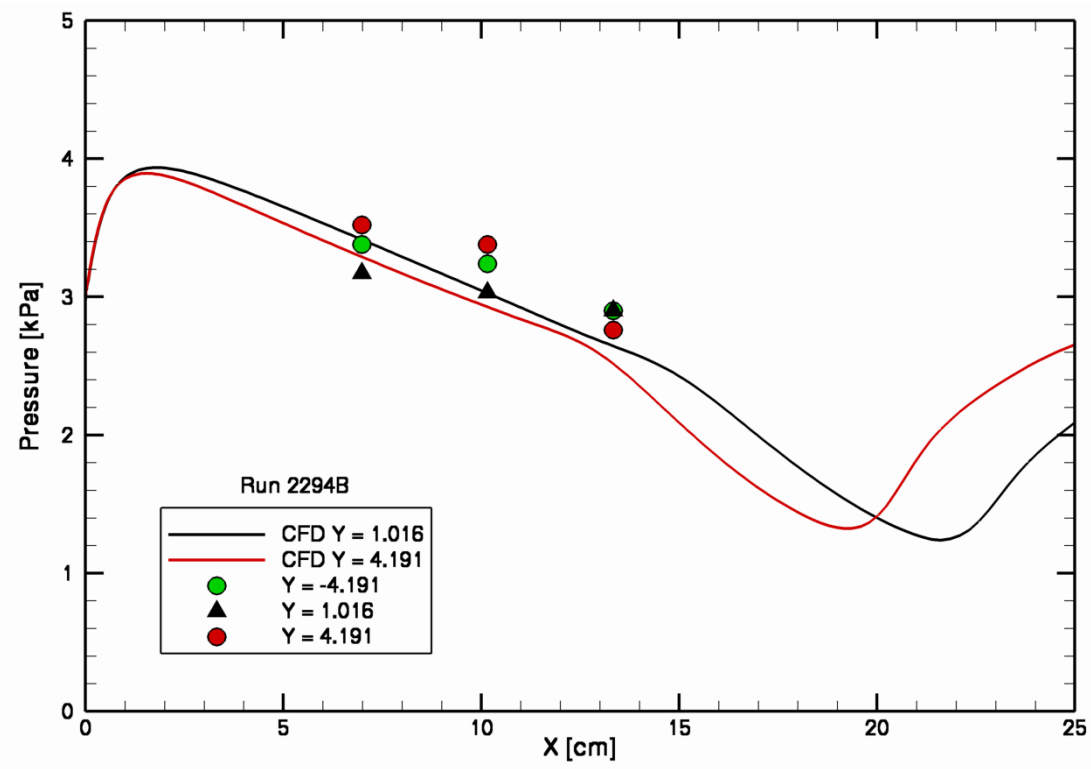

Figure 8: Streamwise comparison with Run 2294 calibration plate pressure data.

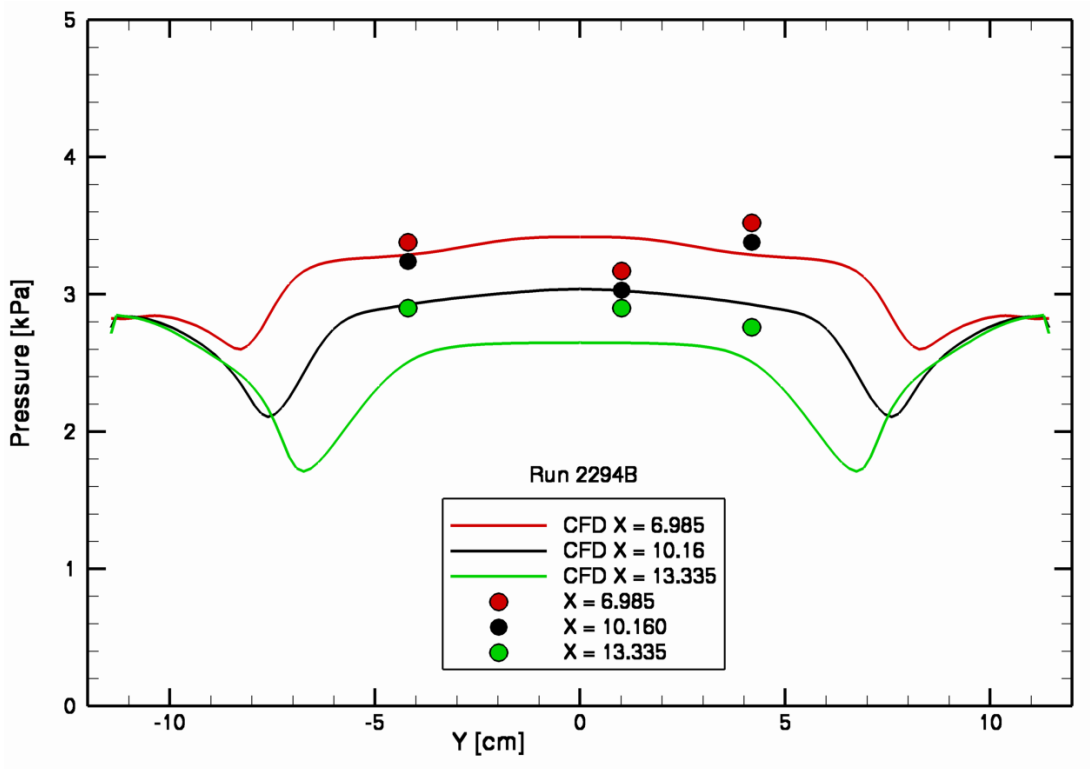

Figure 9: Lateral comparison with Run 2294 calibration plate pressure data.

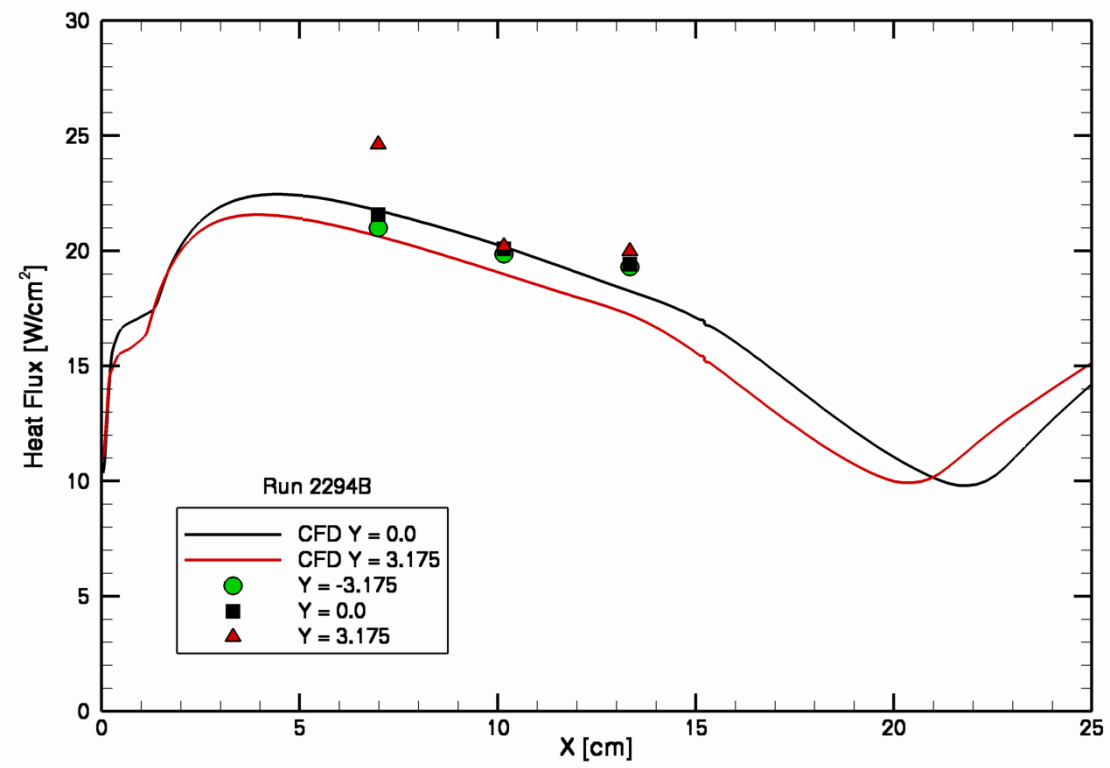

Figure 10: Streamwise comparison with Run 2294B cold wall heat flux data.

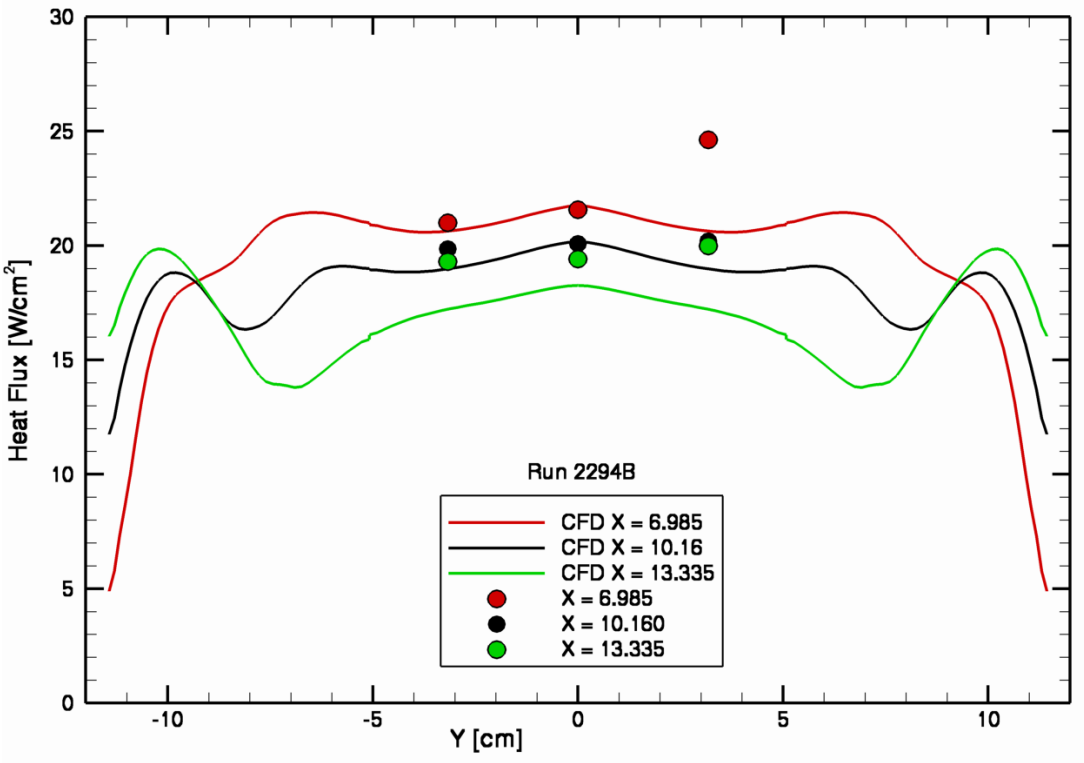

Figure 11: Lateral comparison with Run 2294B cold wall heat flux data.

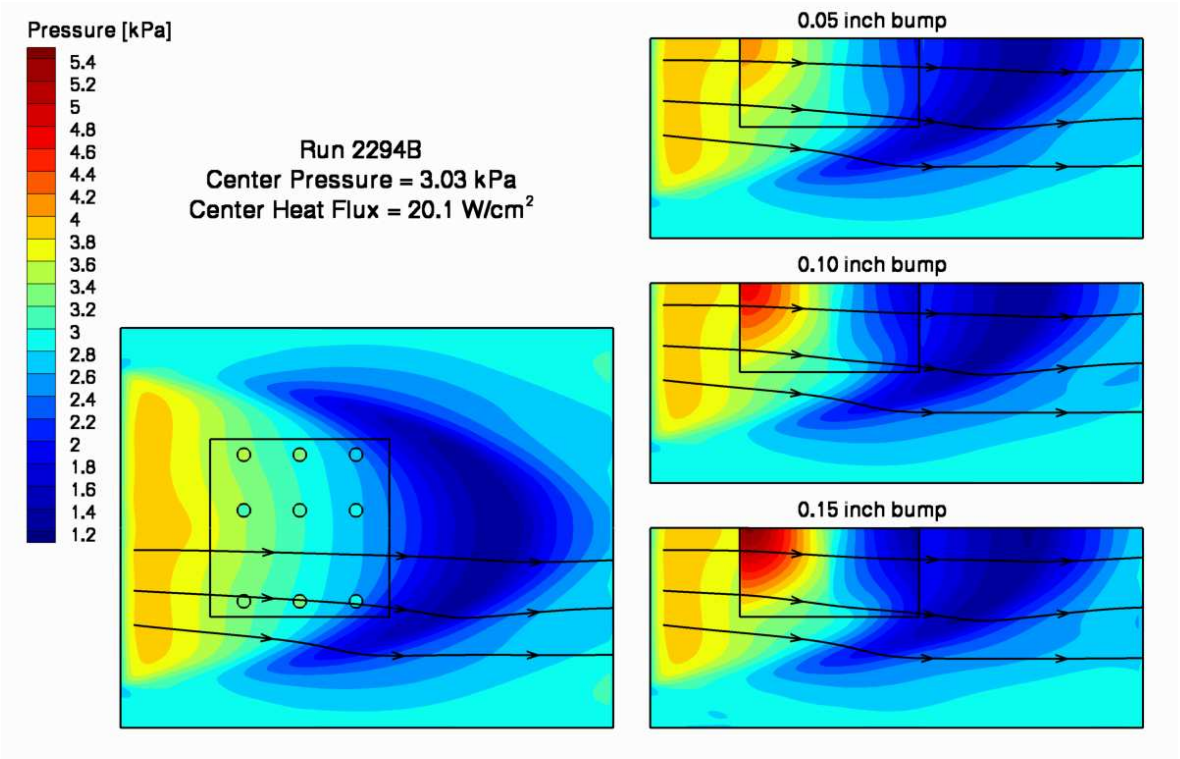

Figure 12: Run 2294B surface pressure variation (CFD inflow calibrated using center measurement).

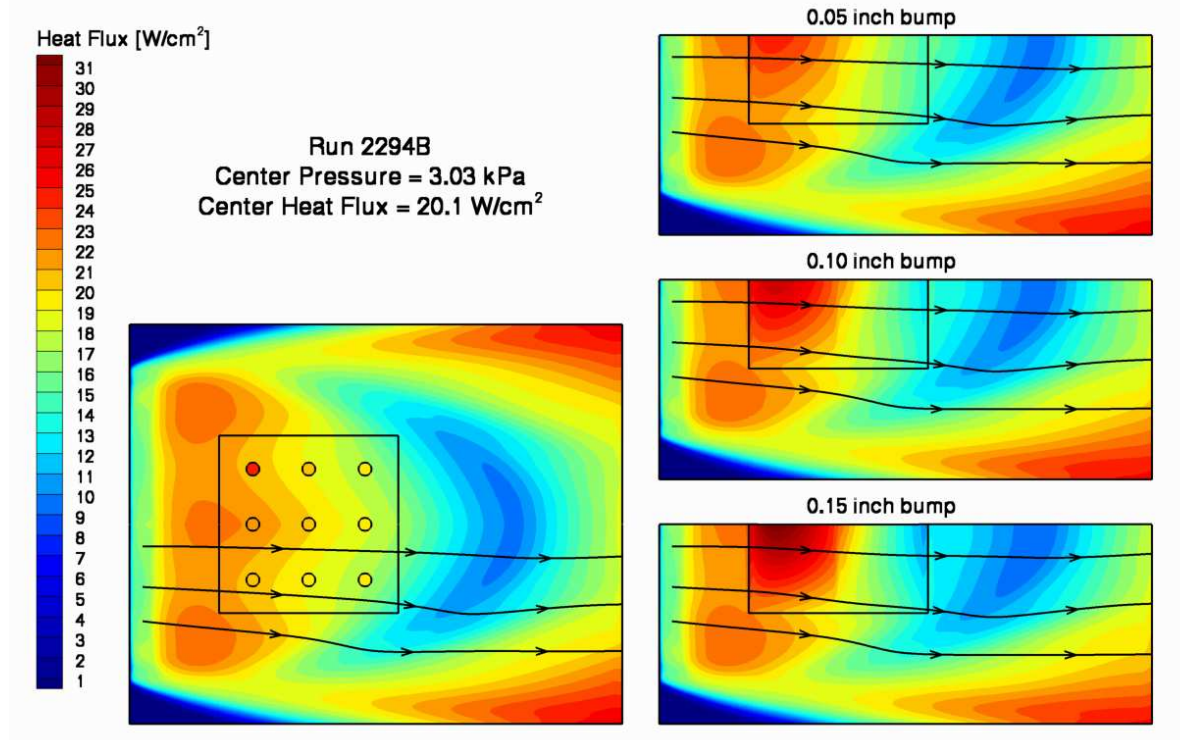

Figure 13: Run 2294B cold wall heat flux variation (CFD inflow calibrated using center measurement).

The same facility nozzle flow was used to perform calculations without allowing heat transfer to the sample area. This was done to identify the maximum surface temperature and quantify the impact of bump height. The results are shown in Figure 14. For all cases, the peak temperature is predicted to occur at the end of the sample along the centerline.

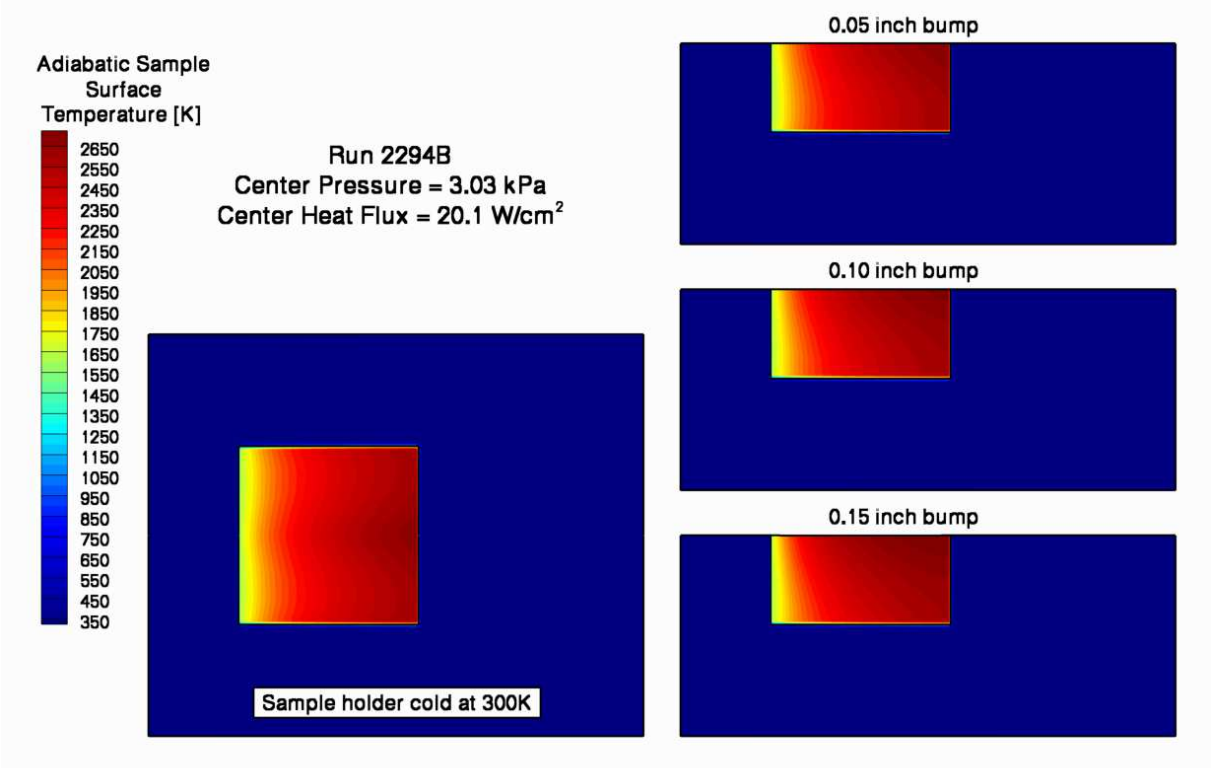

Figure 14: Run 2294B adiabatic surface temperature variation.

The predicted wall shear for all solutions is shown in Figure 15 (top is adiabatic, bottom is 80 °F). Similar to the heat flux trend, compared to the flat plate results, higher shear is predicted on the upstream part of the bump and lower shear on the downstream side. However, a greater variation is caused by the sample temperature. For solutions with an adiabatic boundary condition a large spike in shear is predicted at the surface temperature discontinuity (leading edge of the sample).

Centerline distributions have been extracted from each of the preceding four figures. The pressure trends are included in Figure 16. The expected trends include: generally decreasing pressure down the sample except for the increase caused by bumps and higher surface pressure for a hot surface temperature. Figure 17 shows the cold wall heat flux distribution. At the first measurement location (6.985 cm) the 0.15 inch bump (31.52 W/cm^2) increased the heat flux by 45% compared to a flat plate (21.75 W/cm^2). The bump heat flux results cross the flat plate results at 60.5% along the length of the sample (11.23 cm). Interestingly, this lags the bump pressure results which cross the flat plate results at 52.8% along the length of the sample (10.44 cm). The adiabatic surface temperature distribution is plotted in Figure 18. The bump height affects the shape of the curve, but the value at the end of the sample area is not strongly affected. Figure 19 shows the wall shear sensitivity to wall temperature and bump height. The cold wall bump shear results cross the flat plate results at 65.9% along the sample length. For the hot wall solutions, spikes in shear occur at the sample leading and trailing edges. In addition, for the majority of the sample area the hot versus cold trends change as the bump height increases.

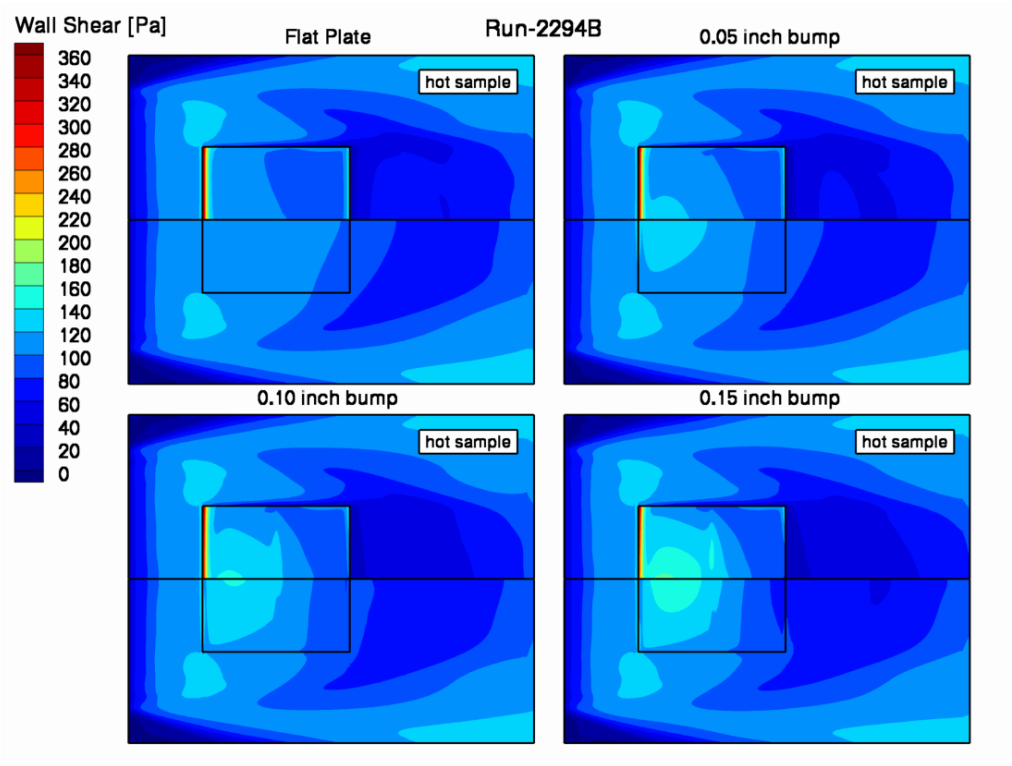

Figure 15: Run 2294B wall shear variation.

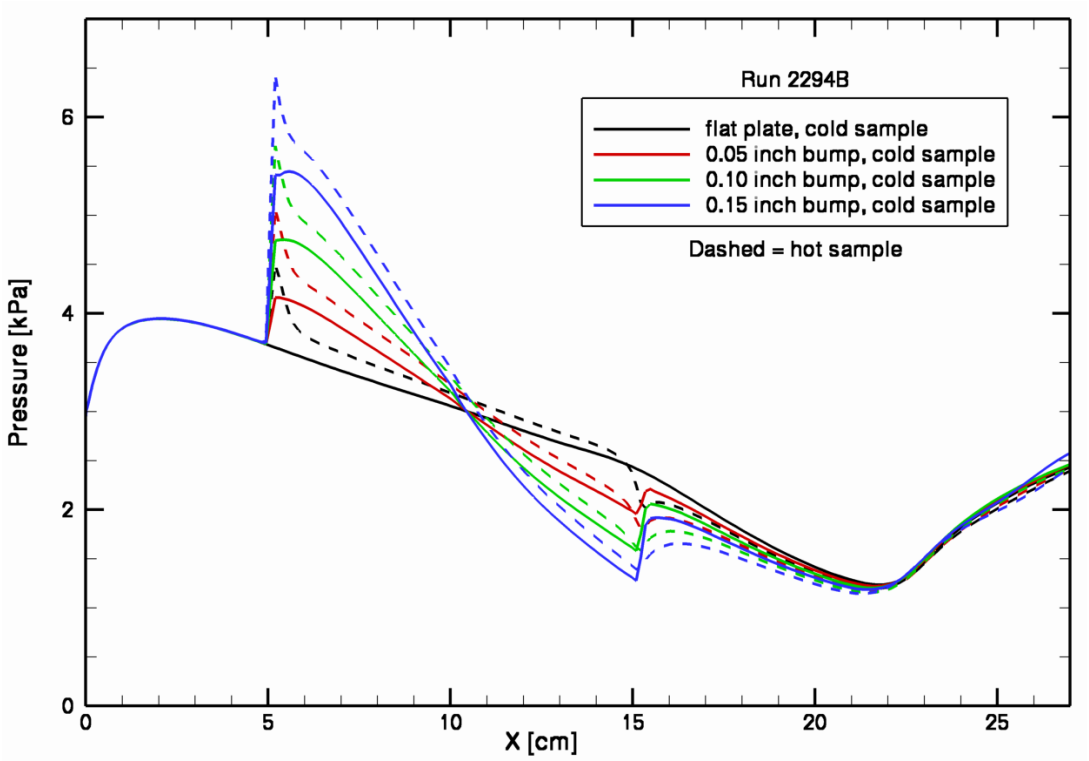

Figure 16: Run 2294B centerline pressure sensitivity to surface temperature and bump height.

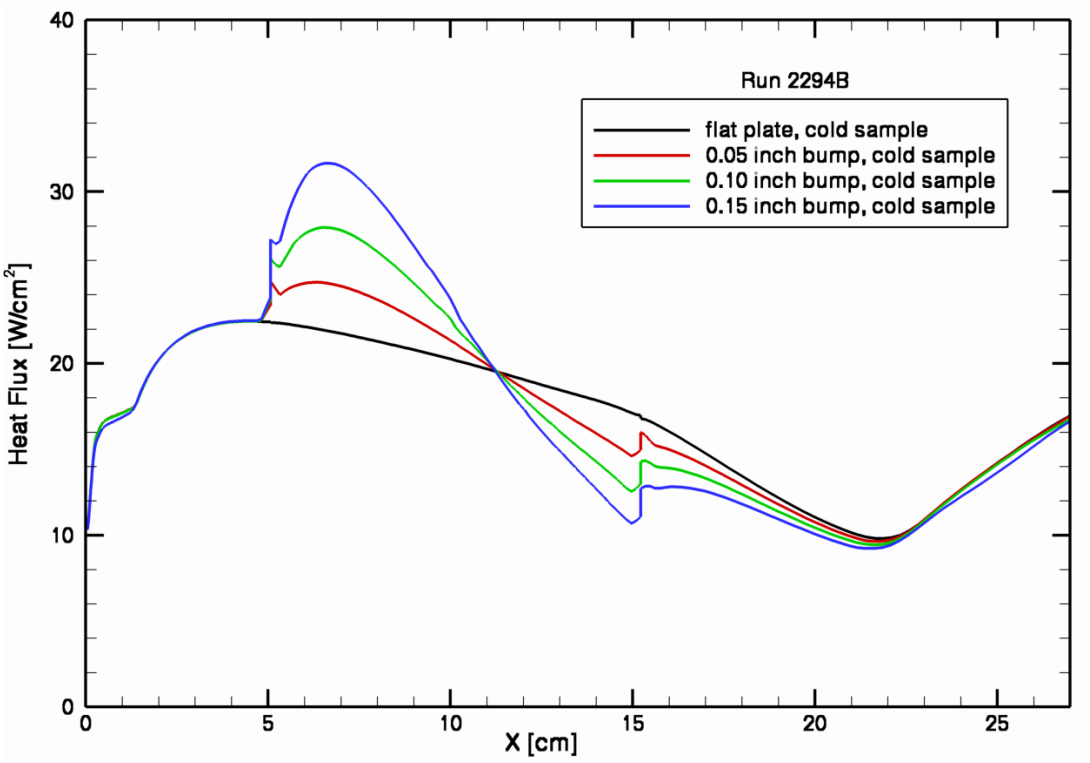

Figure 17: Run 2294B centerline cold wall heat flux sensitivity to bump height.

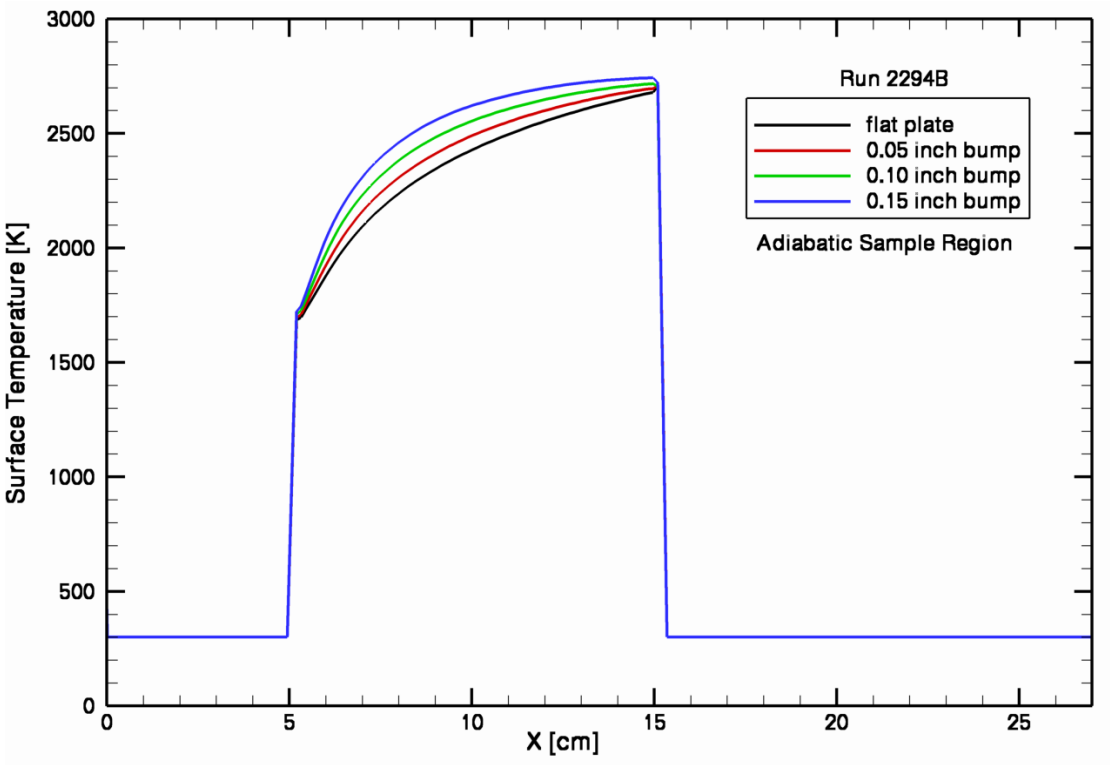

Figure 18: Run 2294B centerline adiabatic surface temperature sensitivity to bump height.

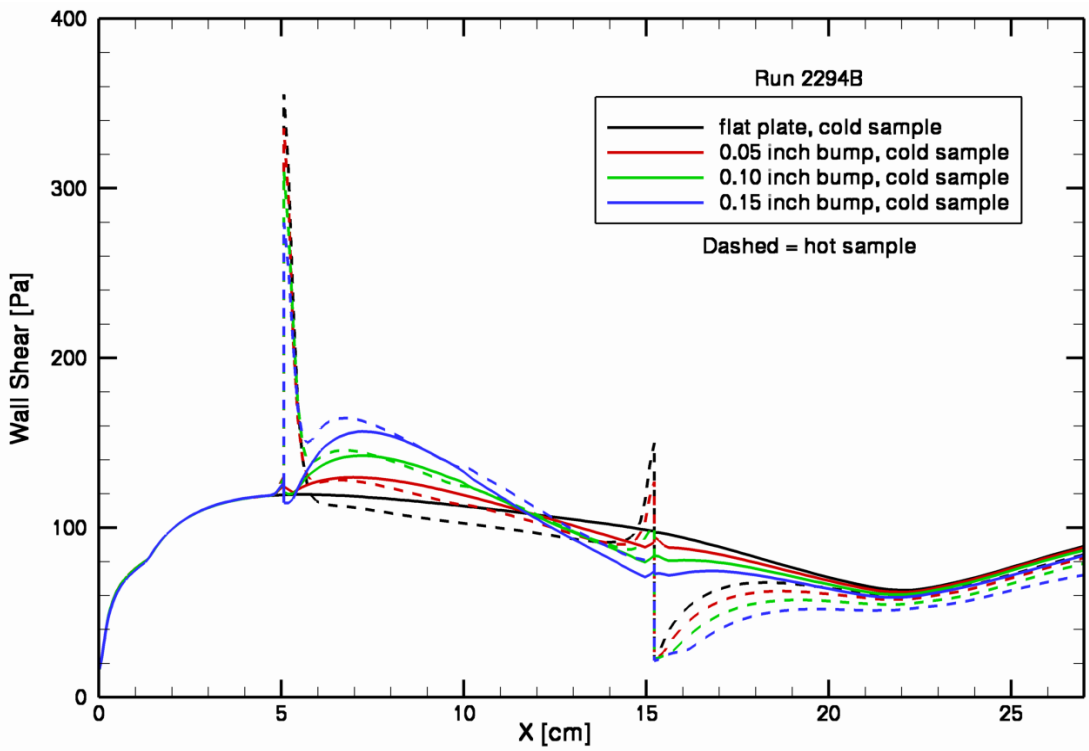

Figure 19: Run 2294B centerline wall shear sensitivity to wall temperature and bump height.

The pressure, heat flux, adiabatic wall temperature, and shear results from the previous four figures were extracted at the three instrumentation locations. Pressure trends are shown in Figure 20. Linear trends are predicted with a positive off-set for a hot surface temperature. Linear trends for heat flux are shown in Figure 21. Figure 22 shows that the predicted adiabatic surface temperature increases as the bump height increases at each streamwise location. The wall shear trends, shown in Figure 23, are the most complex. Although still linear with bump size, for a flat plate or small bump size the shear is predicted to decrease as the surface temperature increases. In contrast, for the largest bump size the shear is predicted to increase at each measurement location as the surface temperature increases. Finally, the same data is plotted as wall shear vs. surface temperature in Figure 24. This allows for the linear interpolation of wall shear predictions to other surface temperatures for each bump size at each measurement location.

Another benefit of using uniform facility plenum conditions is that it specifies a “freestream” total enthalpy which can be used to identify the boundary layer edge (99.5%). A boundary layer post-processor utility was used to extract boundary layer parameters. These can be used to compare with simulations of various flight environments. In addition, heat transfer and skin friction coefficients were calculated with locally varying boundary layer edge conditions. Results for outboard regions of the sample holder could not be computed since the boundary layer edge does not exist due to the plume shape.

The computed boundary layer thickness variations are plotted in Figure 25. The centerline comparison is included in Figure 26. It takes about 2.5 cm before the hot surface temperature produces a thickening of the boundary layer. Compared to a flat plate, the boundary layer becomes thinner on the upstream side of a bump and thicker on the downstream side. Figure 27 shows the computed boundary layer displacement thickness variations. Figure 28 shows the

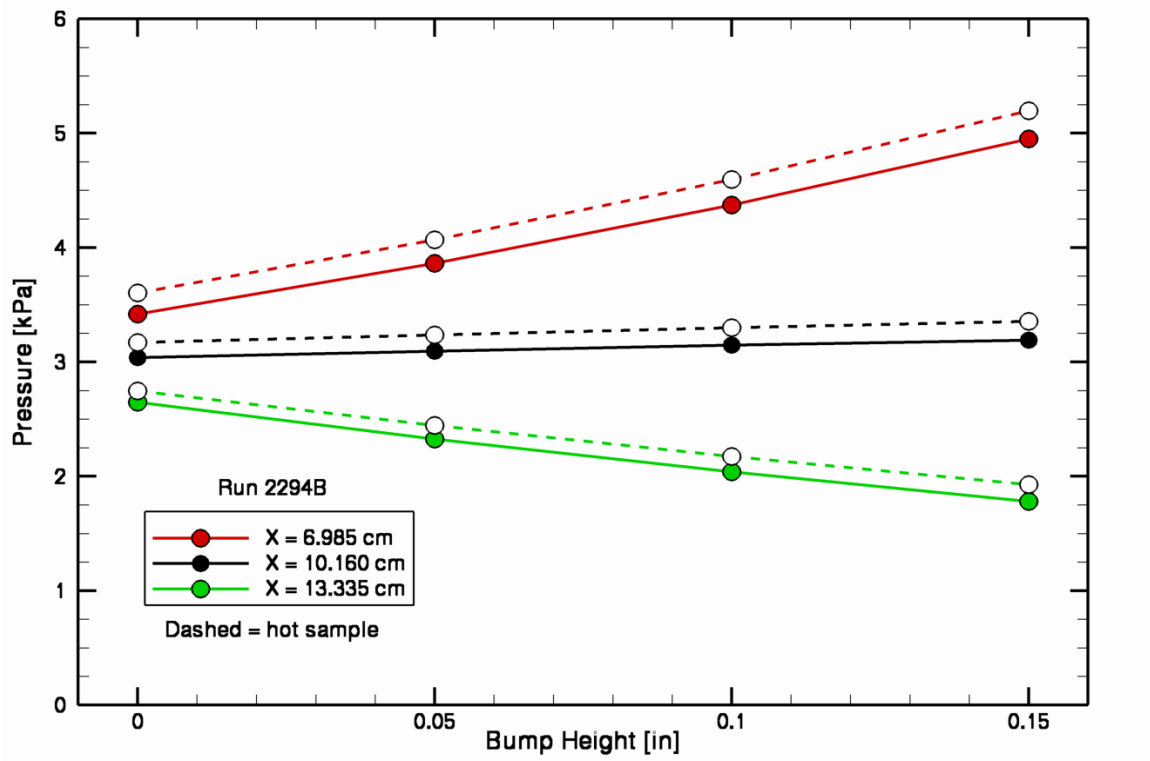

Figure 20: Run 2294B pressure sensitivity to wall temperature and bump height.

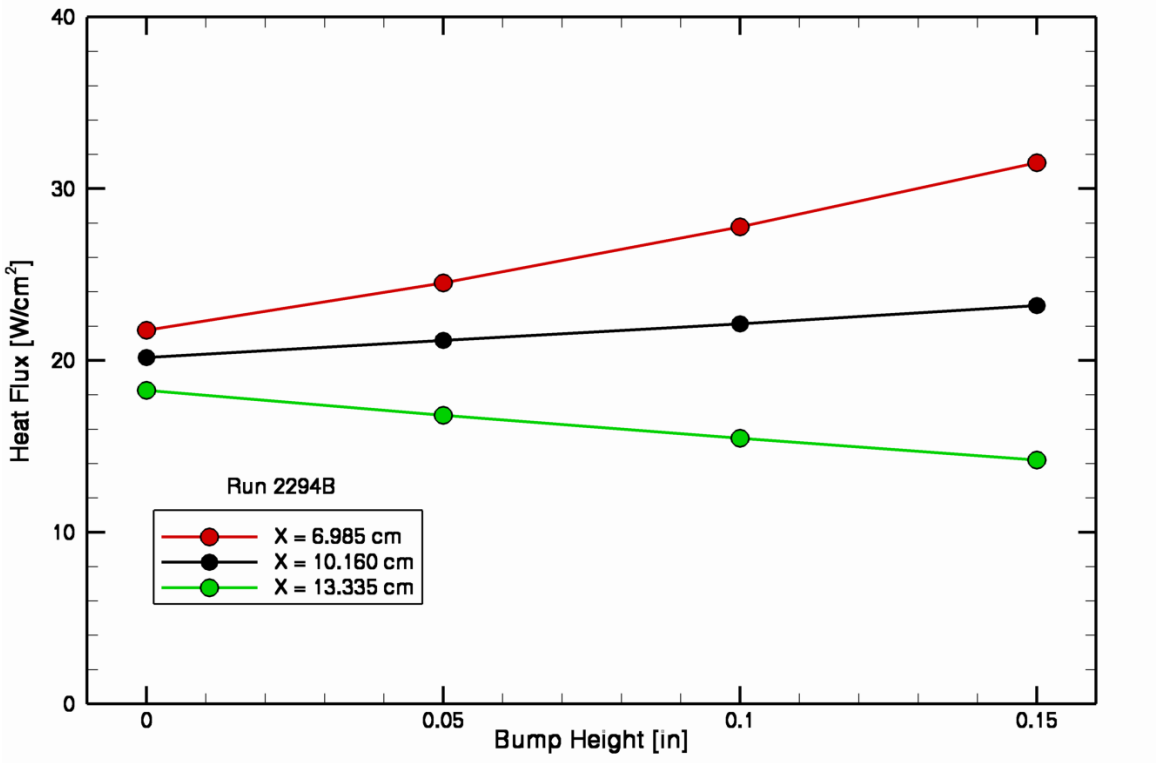

Figure 21: Run 2294B cold wall heat flux sensitivity to bump height.

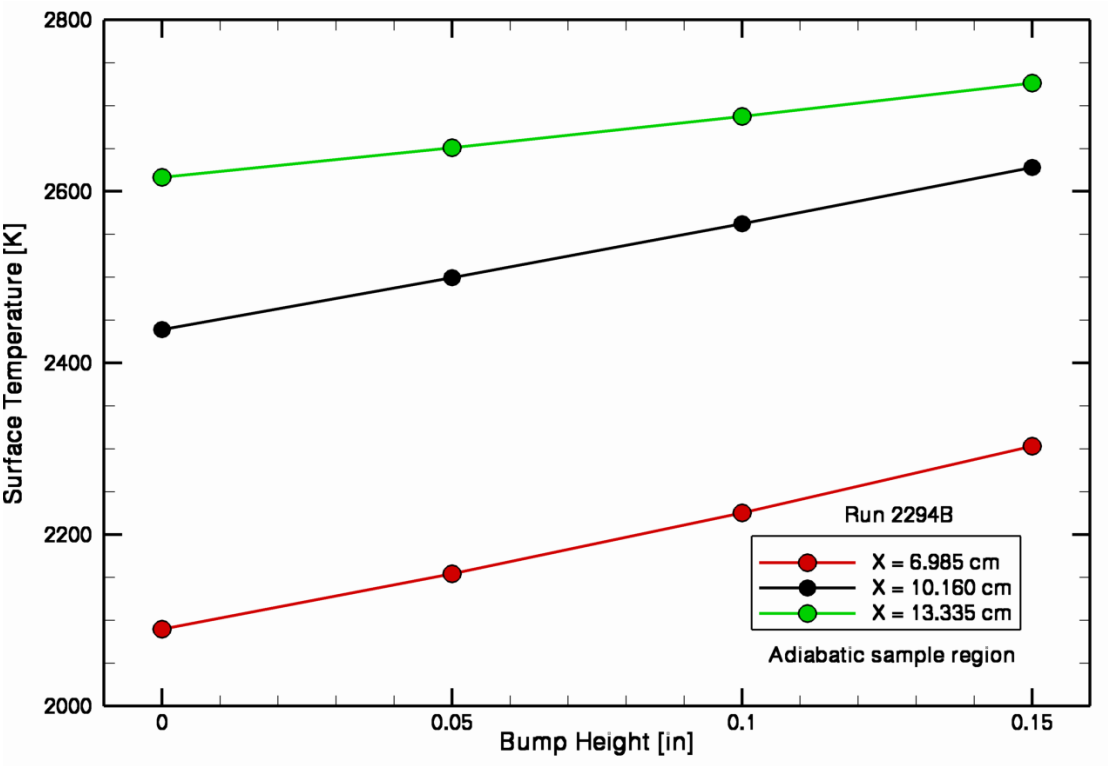

Figure 22: Run 2294B adiabatic surface temperature sensitivity to bump height.

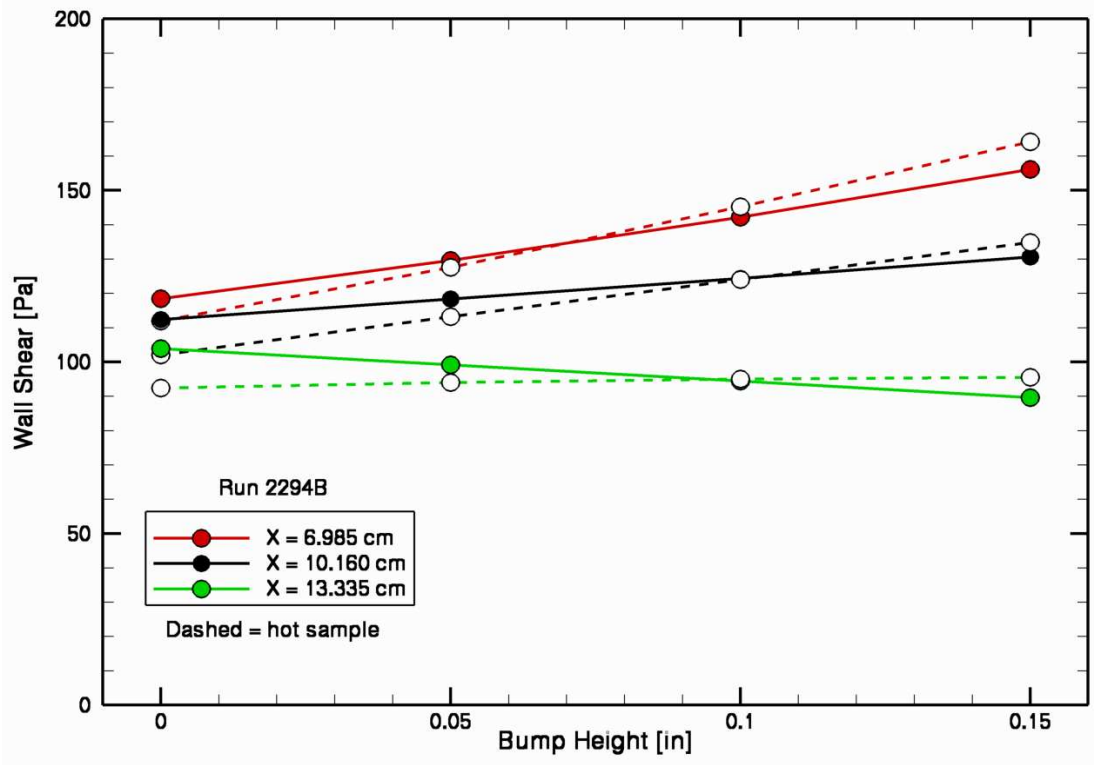

Figure 23: Run 2294B wall shear sensitivity to bump height.

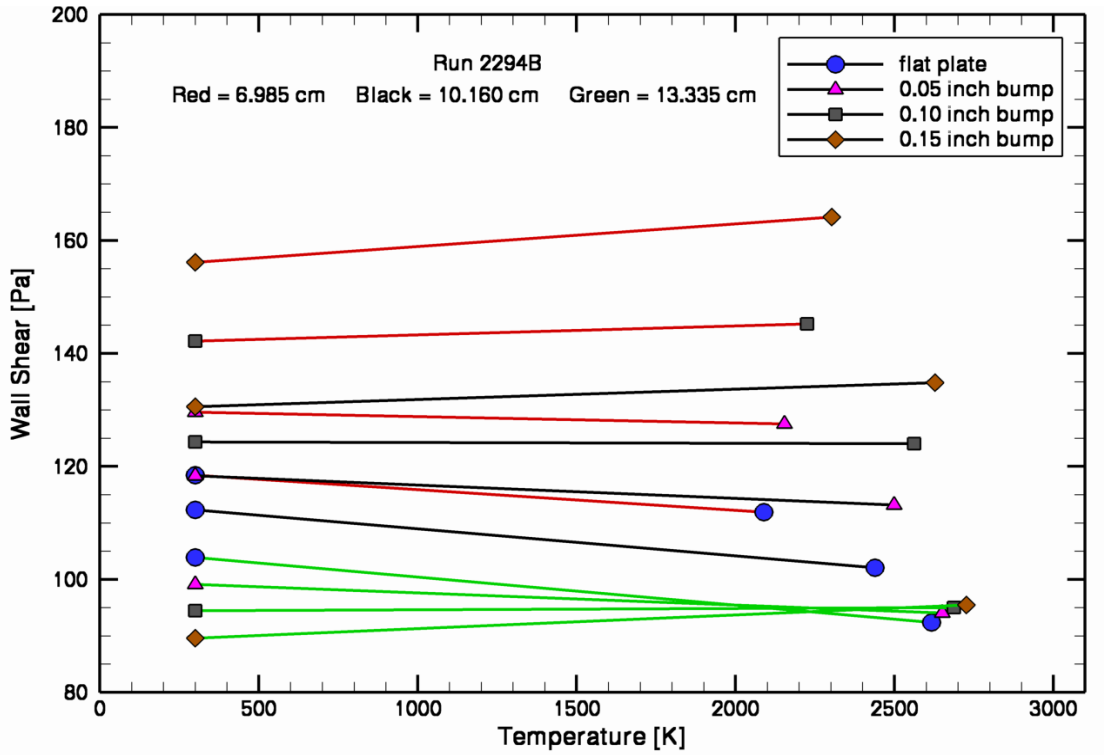

Figure 24: Run 2294B wall shear sensitivity to surface temperature.

distributions along the centerline. For a flat plate, the displacement thickness is nearly constant at approximately 2.4 mm for the first half of the sample area. As the bump height increases a sharp drop occurs at the front of the sample area. The minimum eventually becomes negative for the 0.15 inch bump, which is possible due to significant density gradients. On the downstream side of the bump the displacement thickness is greater than the flat plate case and also increases for an adiabatic surface temperature. Boundary layer momentum thickness results are plotted in Figures 29 and 30. Except near the front of the sample, increasing bump height decreases the momentum thickness. The predicted momentum thickness is not significantly affected by surface temperature. Figures 31 and 32 show the surface variations and centerline distributions of boundary layer enthalpy thickness. The adiabatic surface temperature increases the enthalpy thickness by 67% compared to the corresponding cold wall results.

The combination of surface heat transfer and shear with varying flow properties at the boundary layer edge allow the calculation of heat transfer and skin friction coefficients. The Stanton number variations and centerline distributions are plotted in Figures 33 and 34. Although the heat flux decreases along the centerline for a flat plate (Figure 17), the Stanton number remains nearly constant at 0.0025 for the first half of the sample area. At the end of the sample area, the Stanton number increases despite a decreasing heat flux. The bump results generally follow the heat flux trends but with a more complex distribution due to the varying boundary layer edge conditions. Skin friction coefficient results are included as Figures 35 and 36. Despite a continuously decreasing wall shear along the centerline for a flat plate (Figure 19), the skin friction coefficient increases along the centerline reaching a value of 0.004 at the center of the sample. Dividing the heat transfer coefficient by half of the skin friction coefficient produces predicted Reynolds analogy factor variations and distributions along the centerline shown in Figures 37 and 38. Fairly nice trends are produced which cross at a value of 1.24 at the center of the sample area.

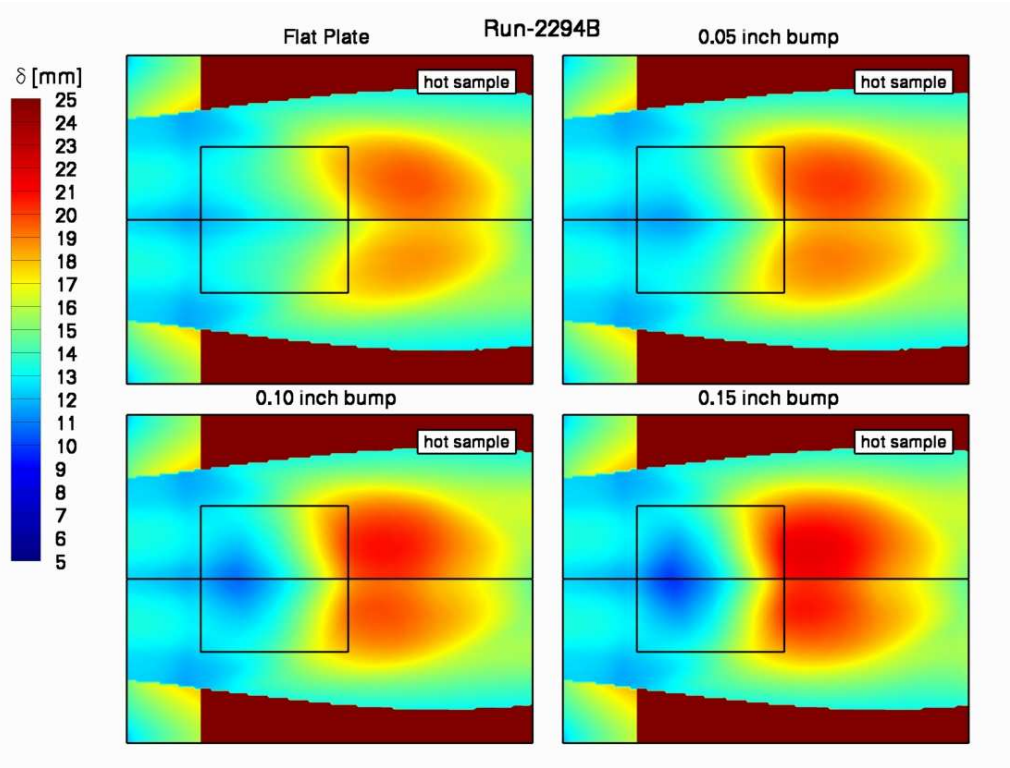

Figure 25: Run 2294B boundary layer thickness variation.

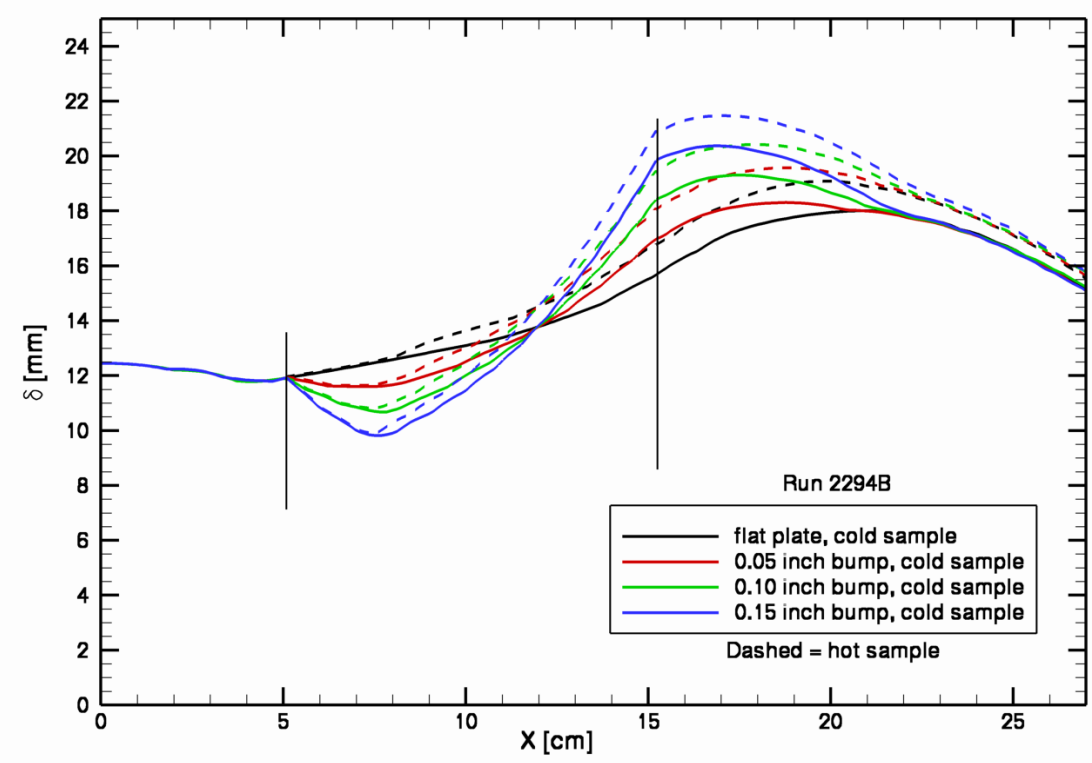

Figure 26: Run 2294B centerline boundary layer thickness comparison.

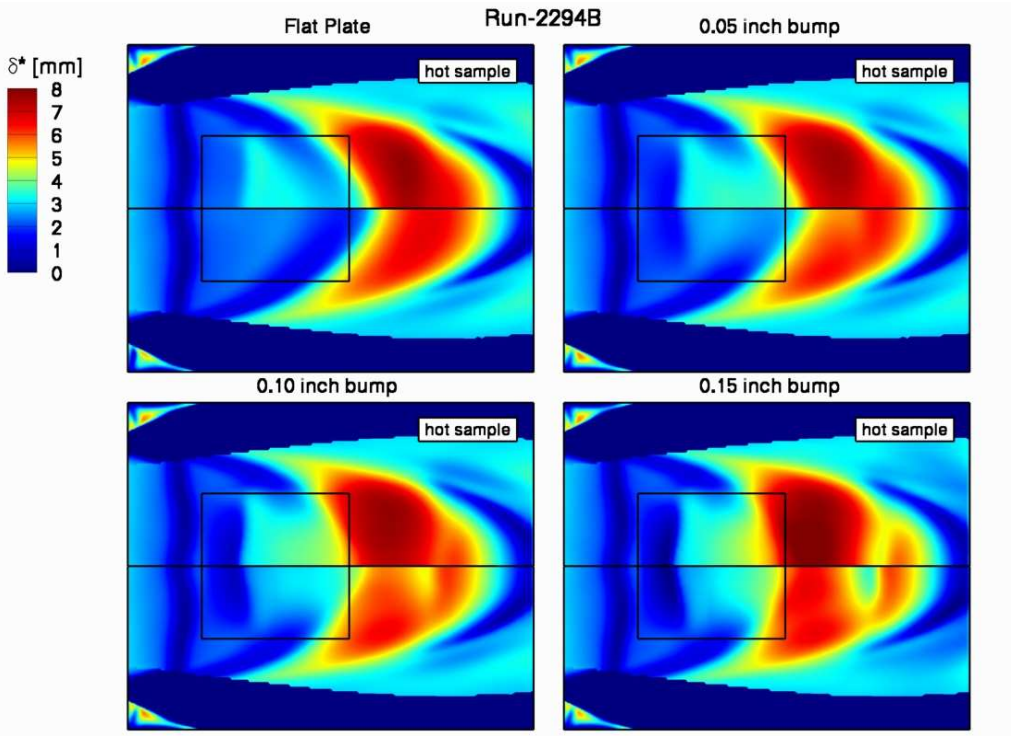

Figure 27: Run 2294B boundary layer displacement thickness variation.

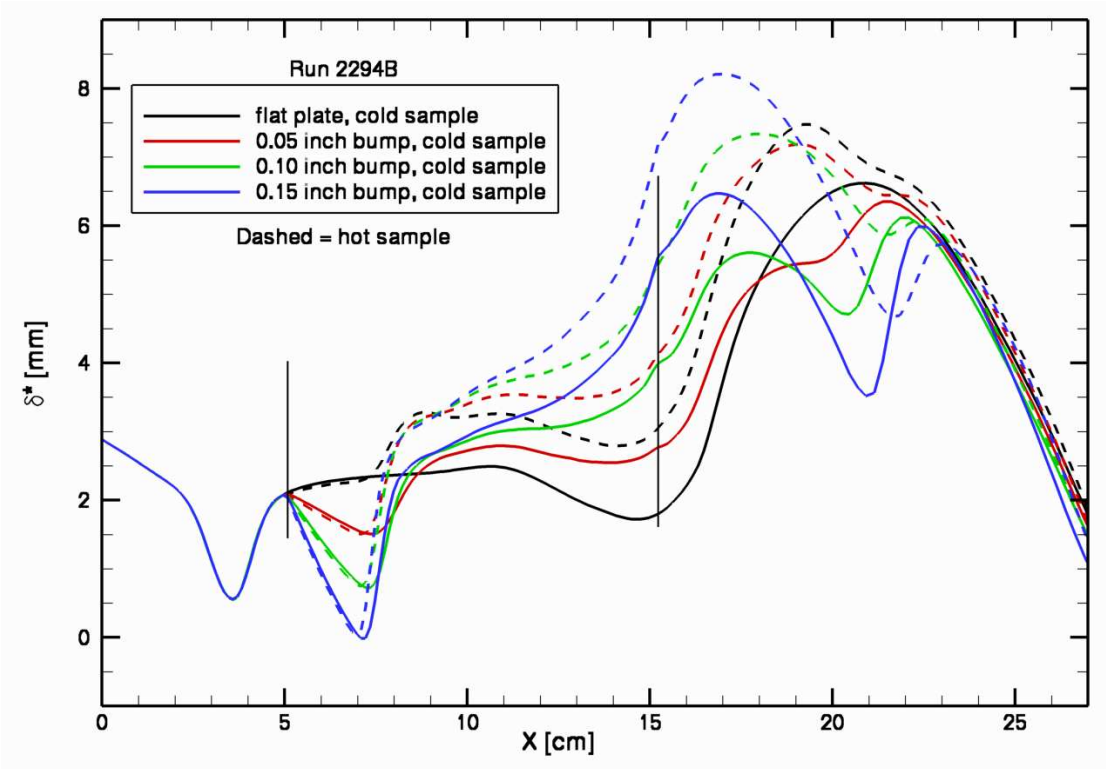

Figure 28: Run 2294B centerline boundary layer displacement thickness comparison.

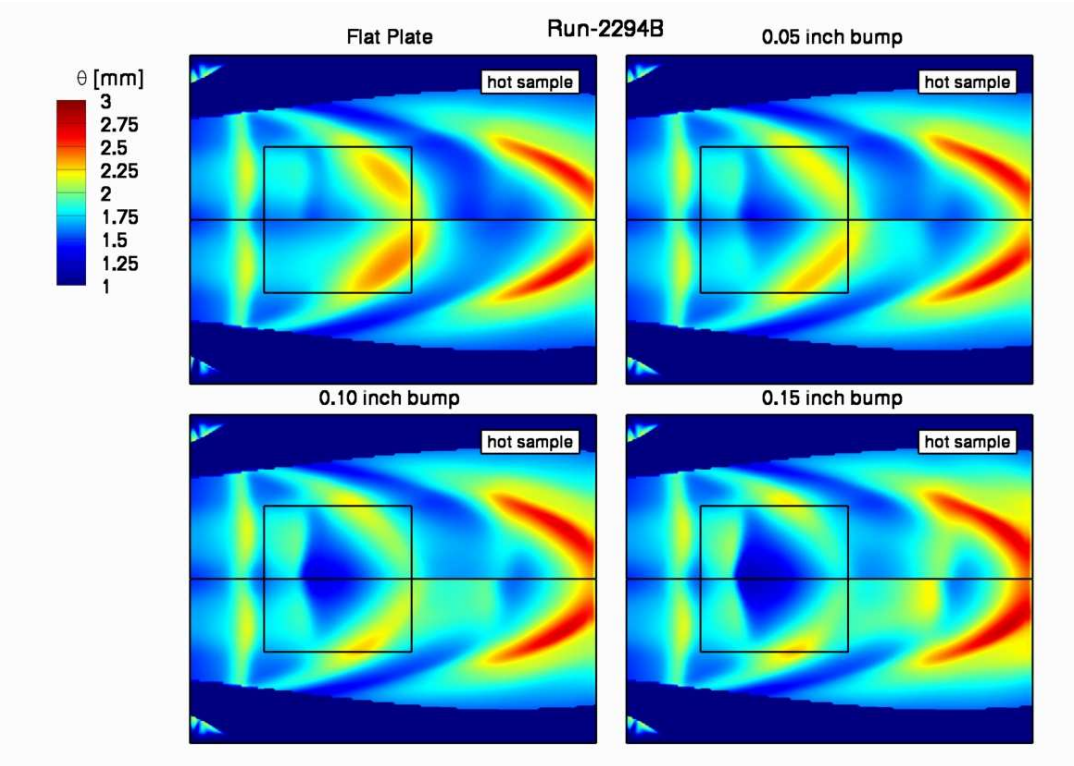

Figure 29: Run 2294B boundary layer momentum thickness variation.

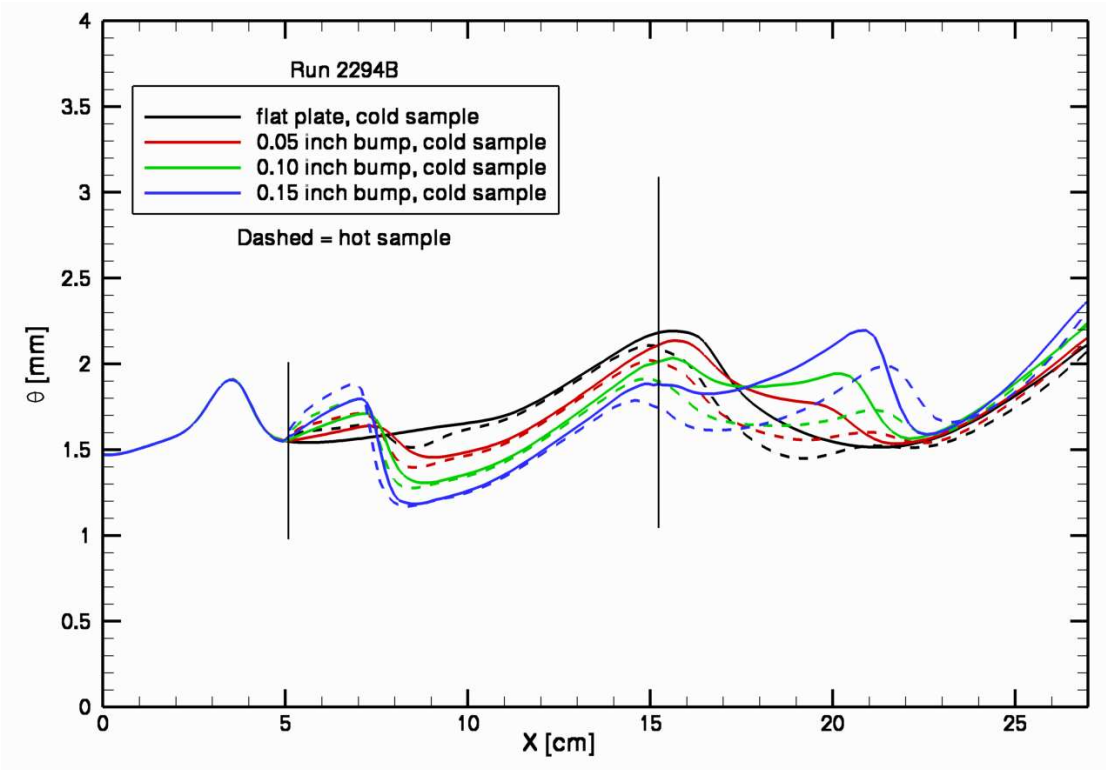

Figure 30: Run 2294B centerline boundary layer momentum thickness comparison.

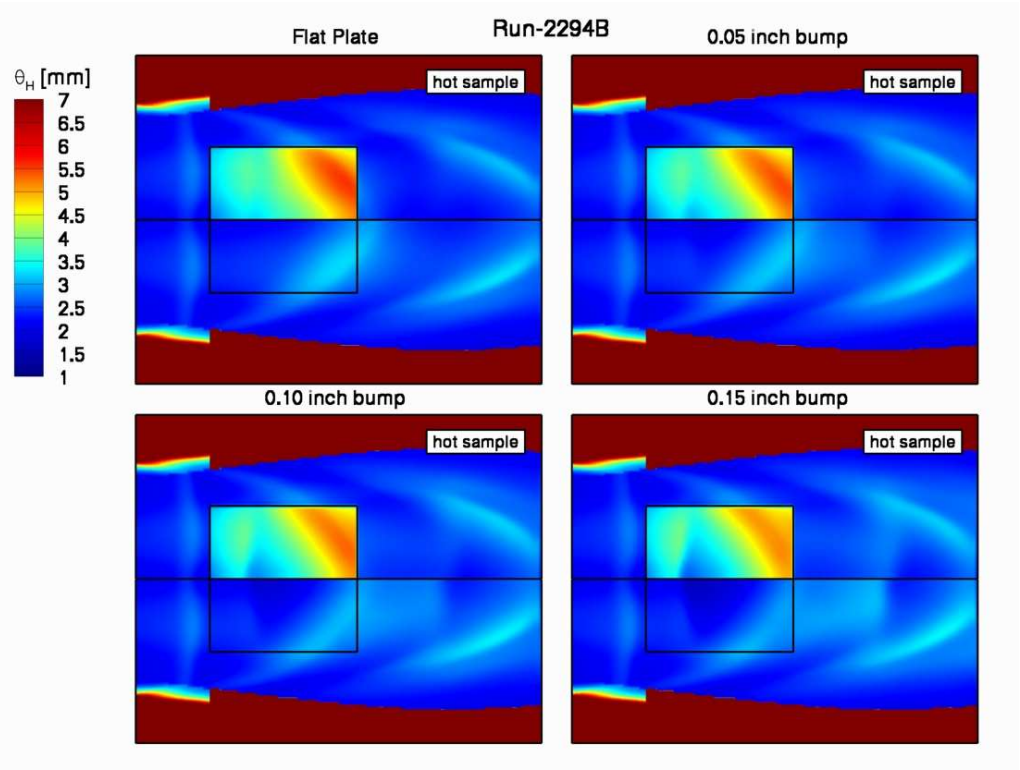

Figure 31: Run 2294B boundary layer enthalpy thickness variation.

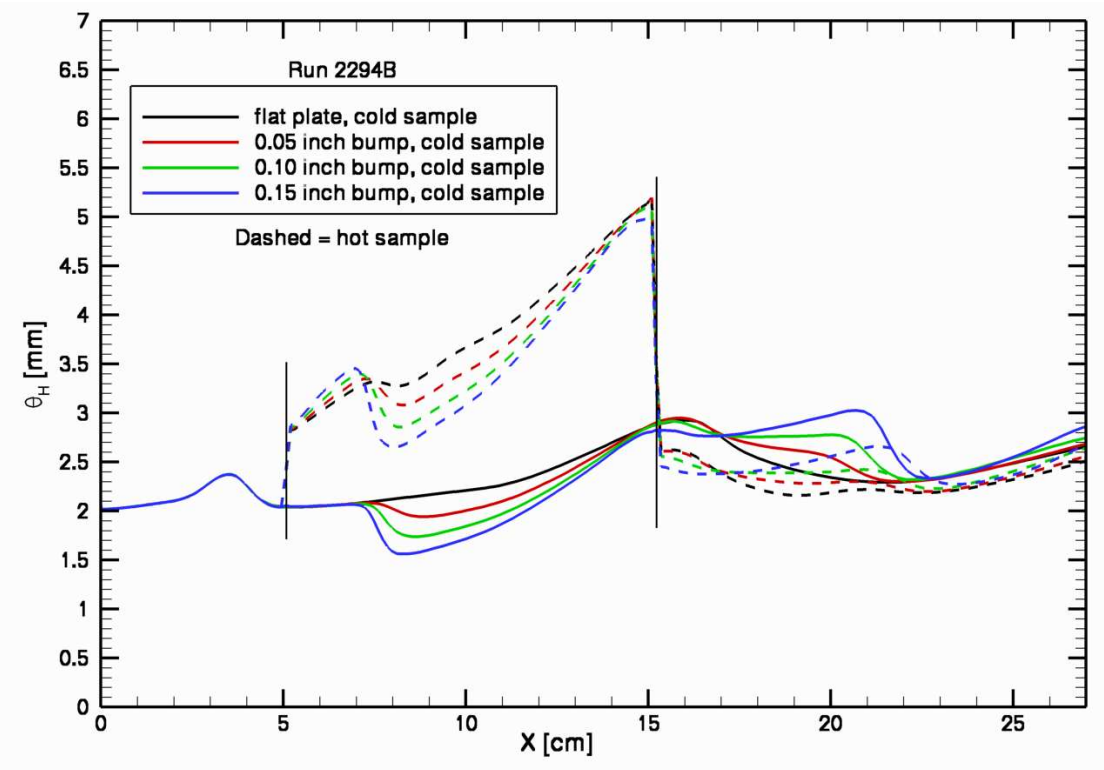

Figure 32: Run 2294B centerline boundary layer enthalpy thickness comparison.

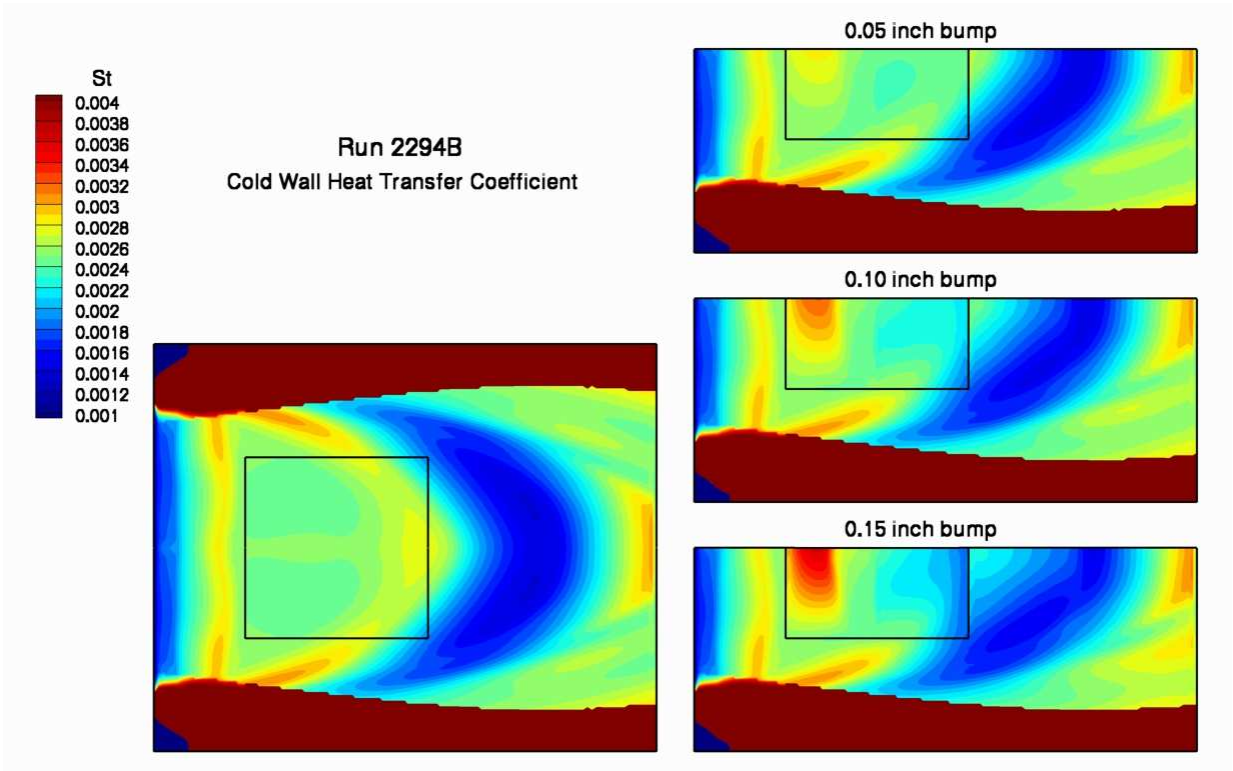

Figure 33: Run 2294B cold wall heat transfer coefficient variation.

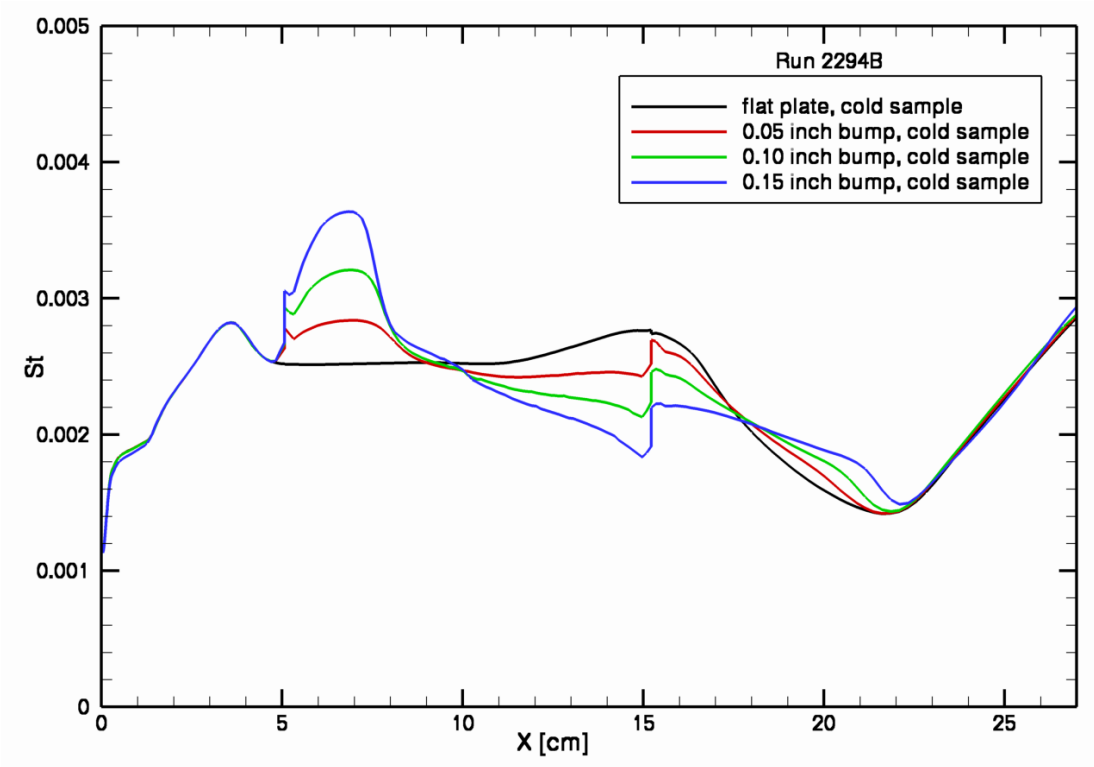

Figure 34: Run 2294B centerline cold wall heat transfer coefficient comparison.

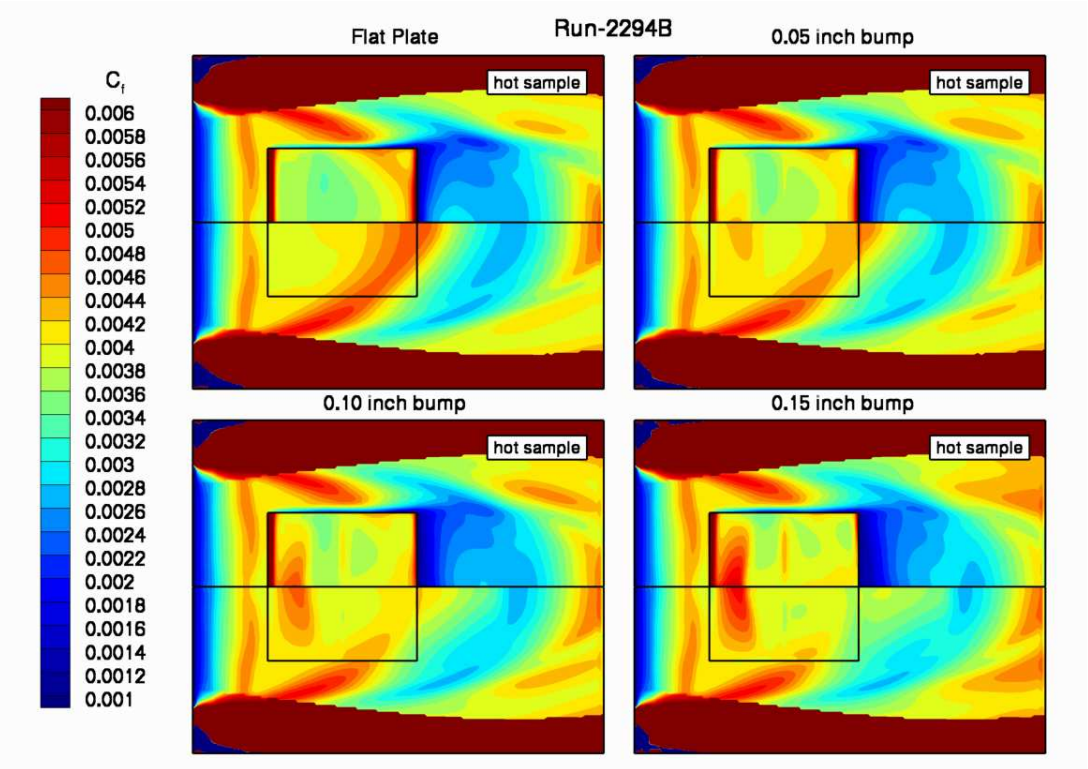

Figure 35: Run 2294B skin friction coefficient variation.

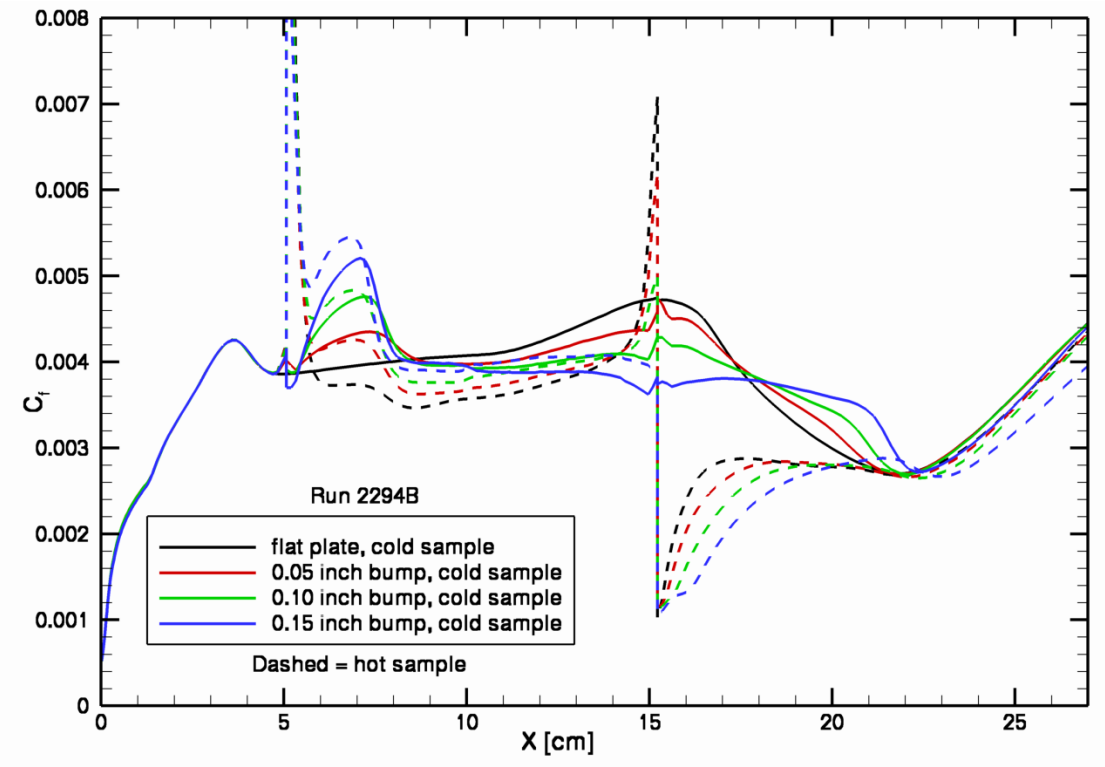

Figure 36: Run 2294B centerline skin friction coefficient comparison.

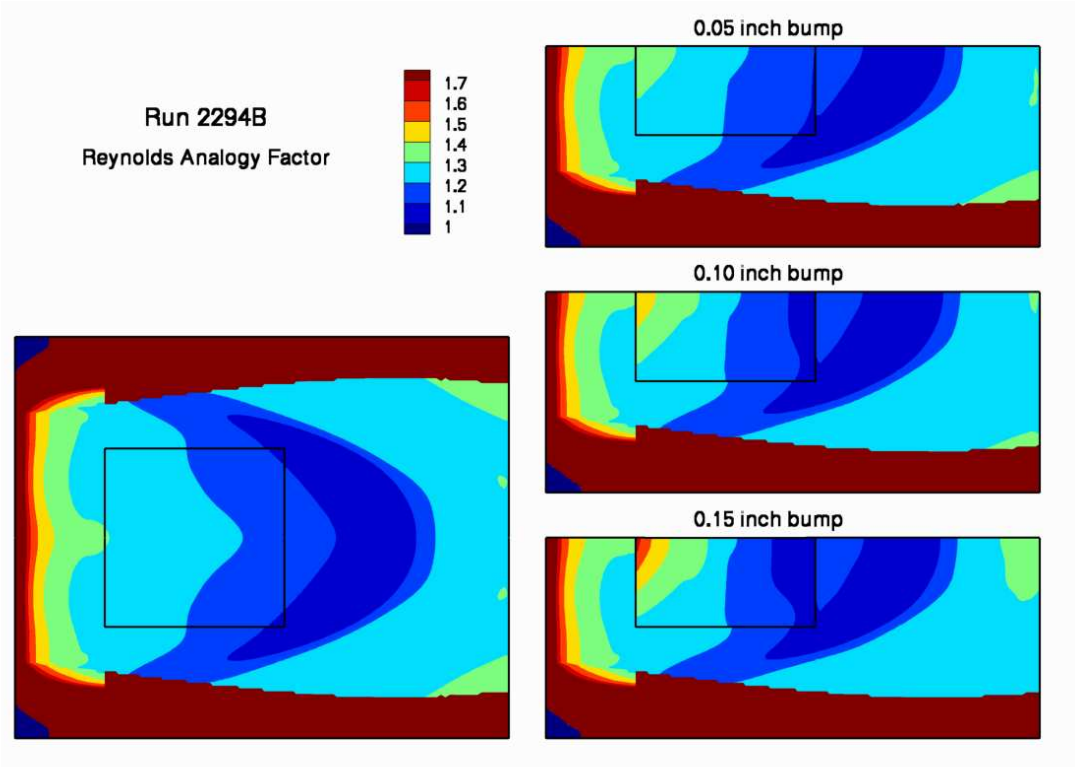

Figure 37: Run 2294B cold wall Reynolds analogy factor variation.

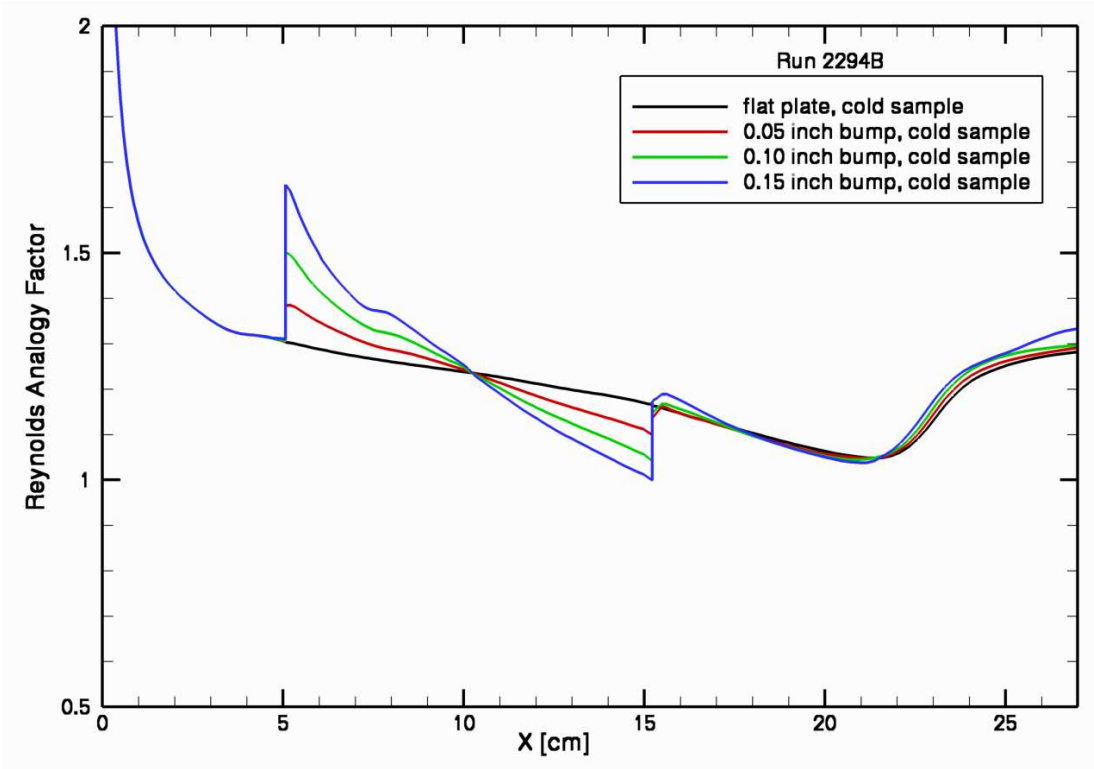

Figure 38: Run 2294B centerline cold wall Reynolds analogy factor comparison.

Results for Run 2294D

With a target of 4.8 kPa / 30 W/cm^2, the experimental and computational conditions are listed in Table 3. For this condition the computational model required 81% of the experimentally reported mass flow. A flat, cold wall shear of 171 Pa at the center of the sample was predicted for this test condition.

Table 3: Facility and calibration plate information for Run 2294D.

	Plenum Pressure (kPa)	Total Air Flow (kg/s)	Nozzle Exit Enthalpy (MJ/kg)	At Center of Calibration Plate		
				Pressure (kPa)	Heat Flux (W/cm^2)	Shear (Pa)
Experiment	912[a]	0.249	5.815	4.83	32.9	N/A
CFD Model	716[b]	0.201	5.864			171

a.) at most upstream wall of heater.

b.) at entrance to facility nozzle throat section.

Streamwise and lateral comparisons with the experimental pressure data are shown in Figures 39 and 40. At each streamwise station higher pressure is measured off centerline. The average experimental difference from Y=-4.191 to Y=4.191 was 0.23 kPa or 4.8% of the center value of 4.83 kPa. In contrast, the CFD simulation indicates higher pressure along the centerline. The simulation also predicts a continuously decreasing pressure over the sample area in the streamwise direction while the first measurement location along the centerline is lower than the second measurement.

Figures 41 and 42 show streamwise and lateral comparisons with the experimental heat flux data. The continuously decreasing predicted heat flux agrees well with the last measurement along the centerline (center point was used to determine uniform facility plenum conditions). The off centerline data straddles the simulation at X=6.985, agrees well at X=10.160, but is under predicted at X=13.335. The average experimental difference from Y=-3.175 to Y=3.175 was 2.27 W/cm^2 or 6.9 % of the center value of 32.92 W/cm^2.

The same facility nozzle exit flow was used to perform 7 more simulations. These included the same bump geometries described previously and each geometry solved with an adiabatic wall boundary condition. The variations in surface pressure are plotted in Figure 43. The total variation over the sample area was 2.86 – 5.89 kPa for the flat plate. The pressure is higher than the Run 2294B conditions, therefore the flow is not as affected by the 2.9 kPa cabin pressure. However, the trends remain the same: fairly uniform pressure laterally (except at the end corners), monotonically decreasing axially, and same affects created by the bump geometries. The cold wall heat flux variations are shown in Figure 44. Similar to Run 2294B, the heat flux varies much more axially than laterally. The total variation over the sample area was 22.0 – 37.3 W/cm^2 for the flat plate.

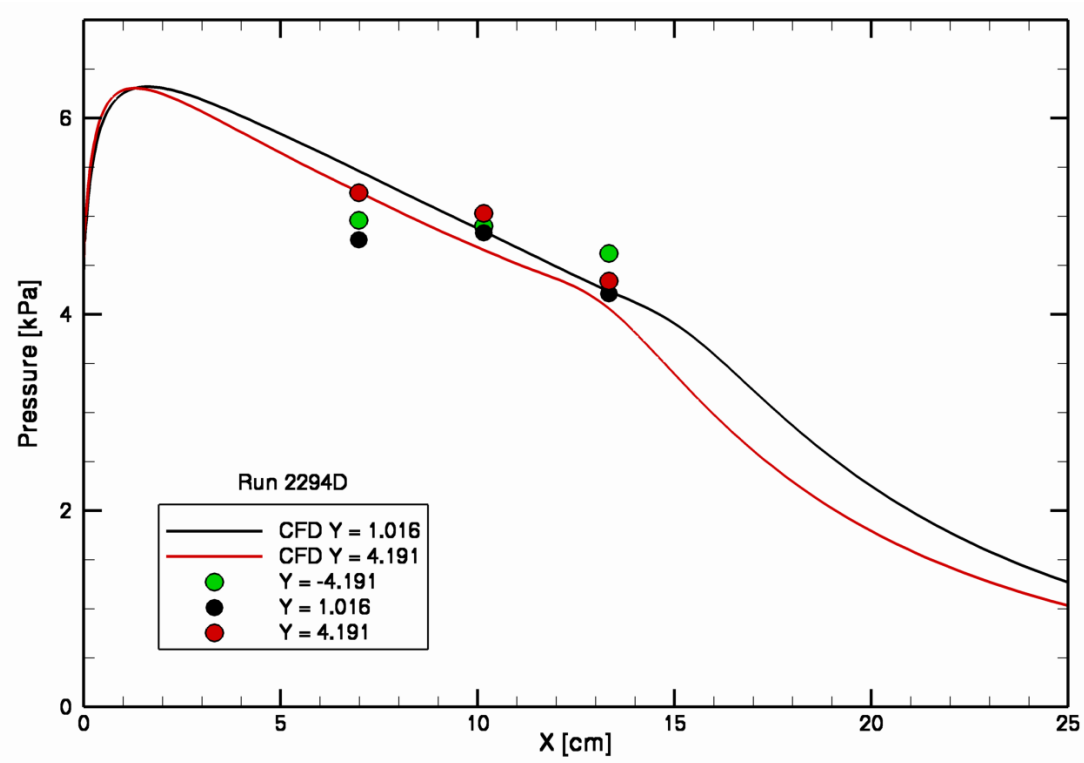

Figure 39: Streamwise comparison with Run 2294D calibration plate pressure data.

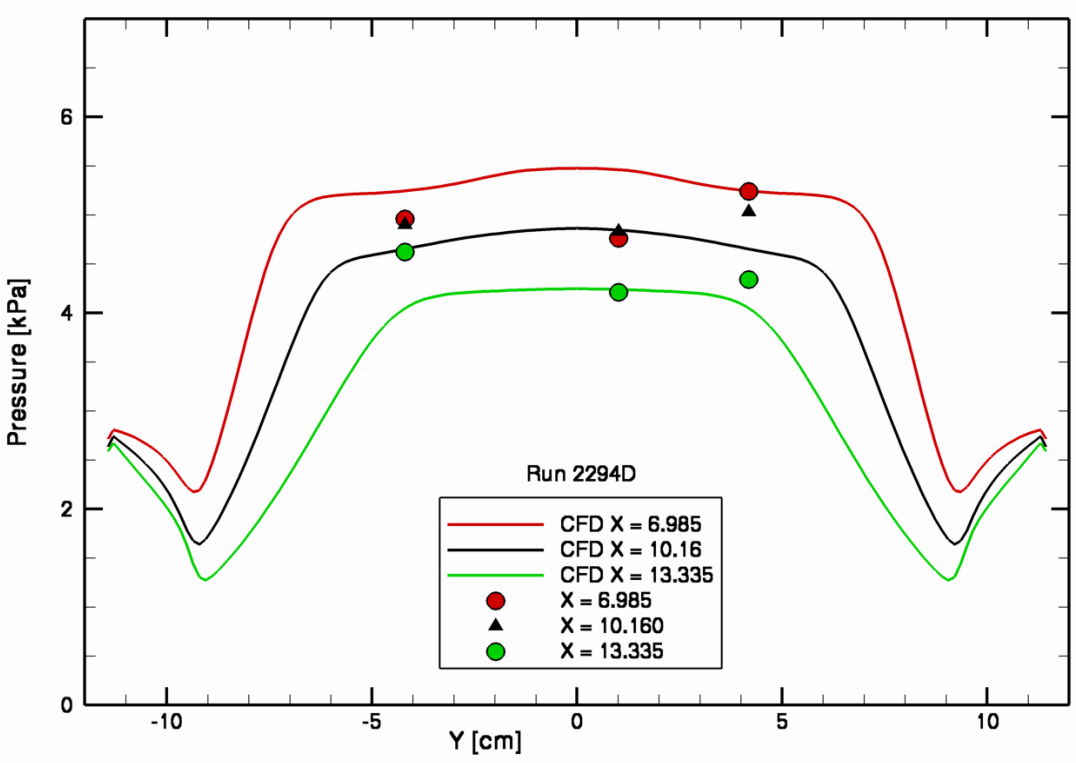

Figure 40: Lateral comparison with Run 2294D calibration plate pressure data.

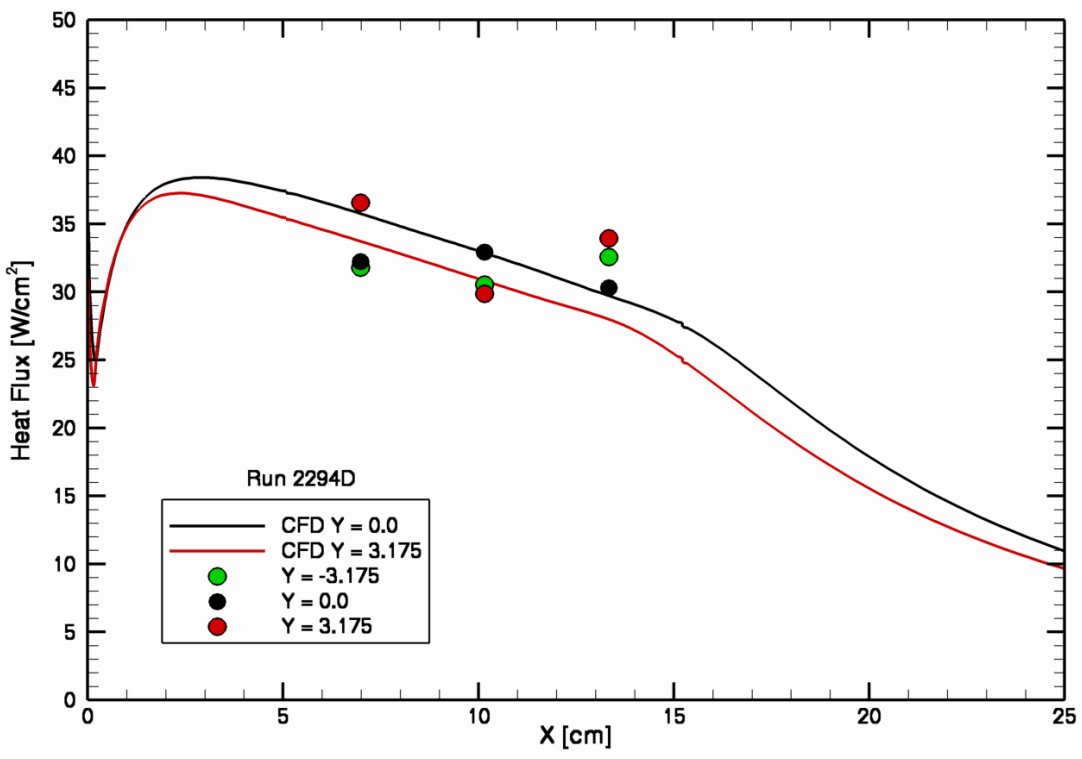

Figure 41: Streamwise comparison with Run 2294D cold wall heat flux data.

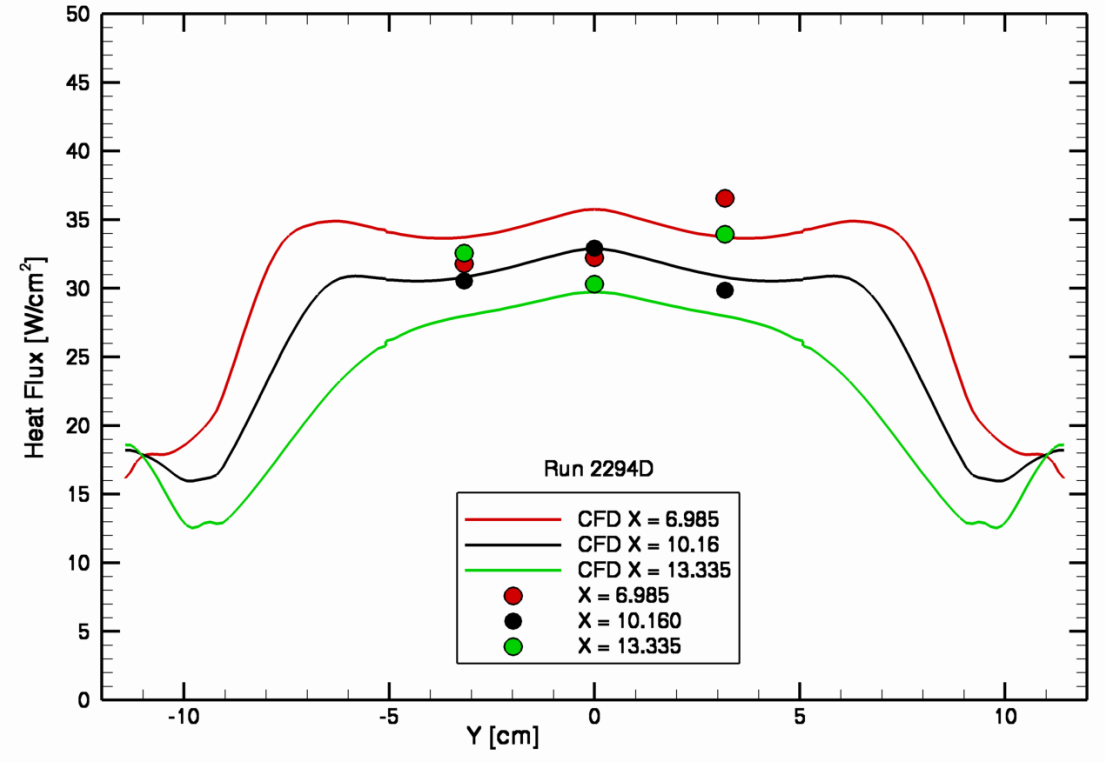

Figure 42: Lateral comparison with Run 2294D cold wall heat flux data.

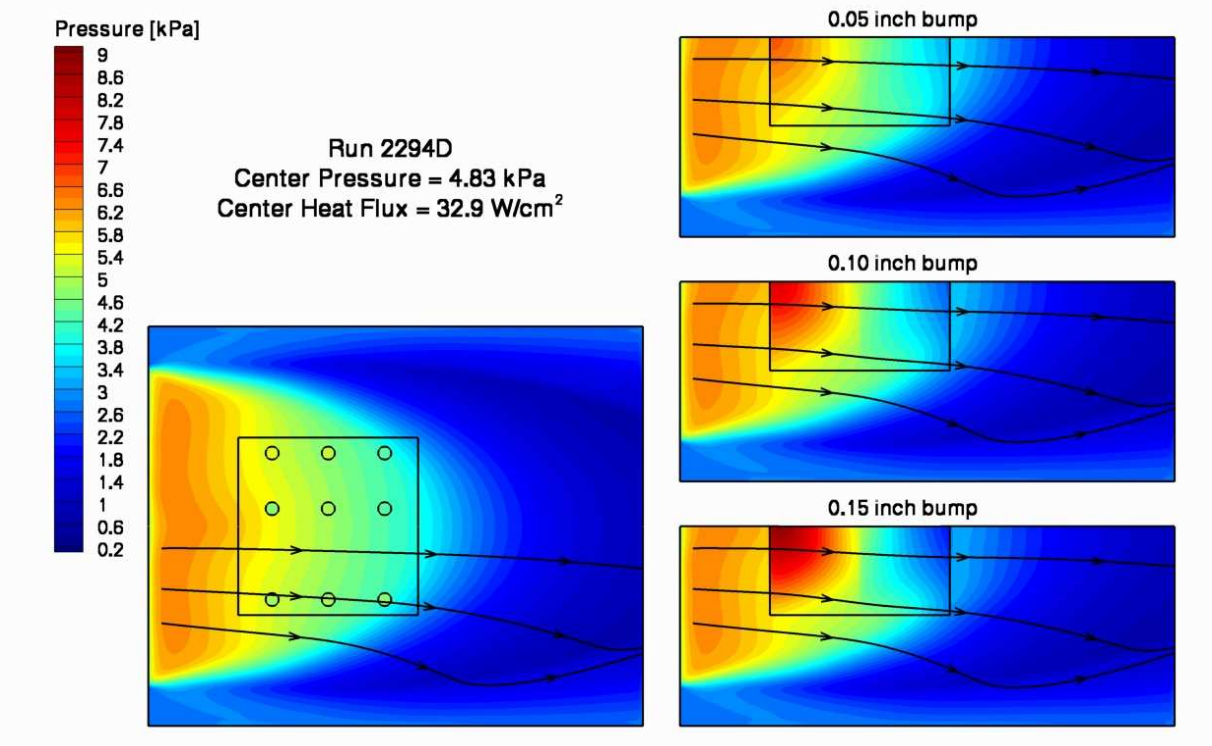

Figure 43: Run 2294D surface pressure variation (CFD inflow calibrated using center measurement).

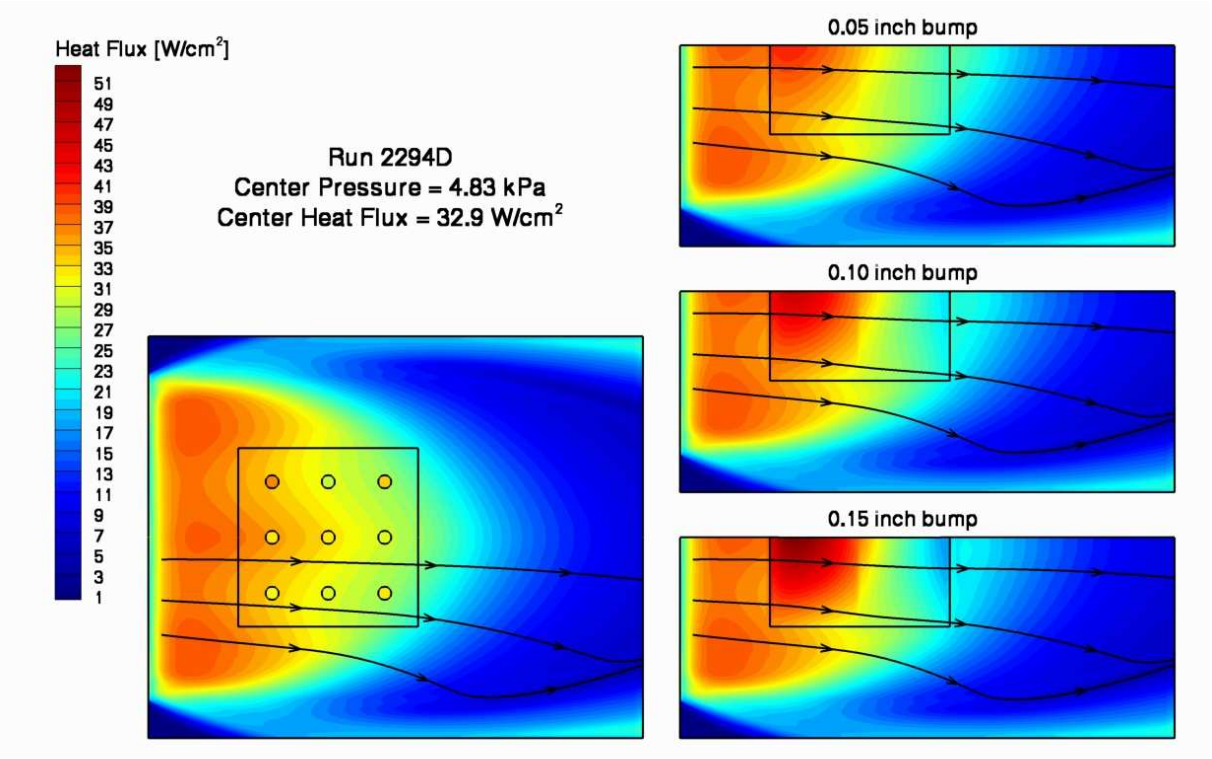

Figure 44: Run 2294D cold wall heat flux variation (CFD inflow calibrated using center measurement).

Four simulations were completed with an adiabatic wall boundary condition rather than a specified cold wall temperature. This quantifies the shear sensitivity to surface temperature. The predicted adiabatic wall temperature variation over the sample areas are shown in Figure 45.

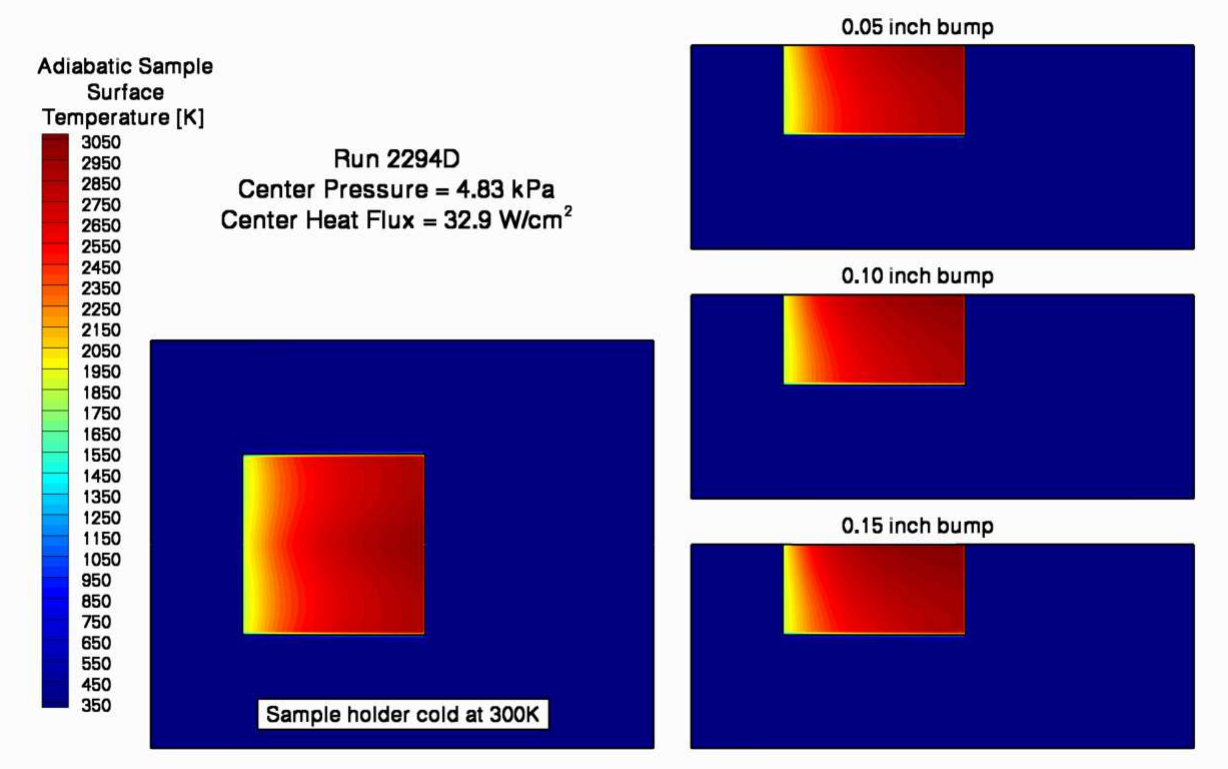

Figure 45: Run 2294D adiabatic surface temperature variation.

The predicted wall shear for all solutions is shown in Figure 46. The results are similar to Run 2294B, with higher shear generated on the upstream ~66% of the bump and lower shear to the remaining length compared to the flat plate results.

Centerline distributions have been extracted from each of the preceding four figures and show trends similar to the Run 2294B results. The pressure distribution shown in Figure 47 reveals that the pressure at the center of the sample area is nearly independent of bump size or surface temperature. The cold wall heat flux results are included in Figure 48. For the flat plate the heat flux at the upstream measurement location (6.985 cm) is 1.20 times greater than at the downstream measurement location (13.335 cm). This ratio increases to 2.32 for a 0.15 inch bump. Figure 49 shows the adiabatic surface temperature sensitivity to bump height. The wall shear from all 8 simulations, in Figure 50, shows the expected variation with bump height and the large spike at the leading edge of the sample due to the surface temperature discontinuity. The ratio of shear for the two locations described above is 1.15 for the flat plate and 1.82 for the 0.15 inch bump.

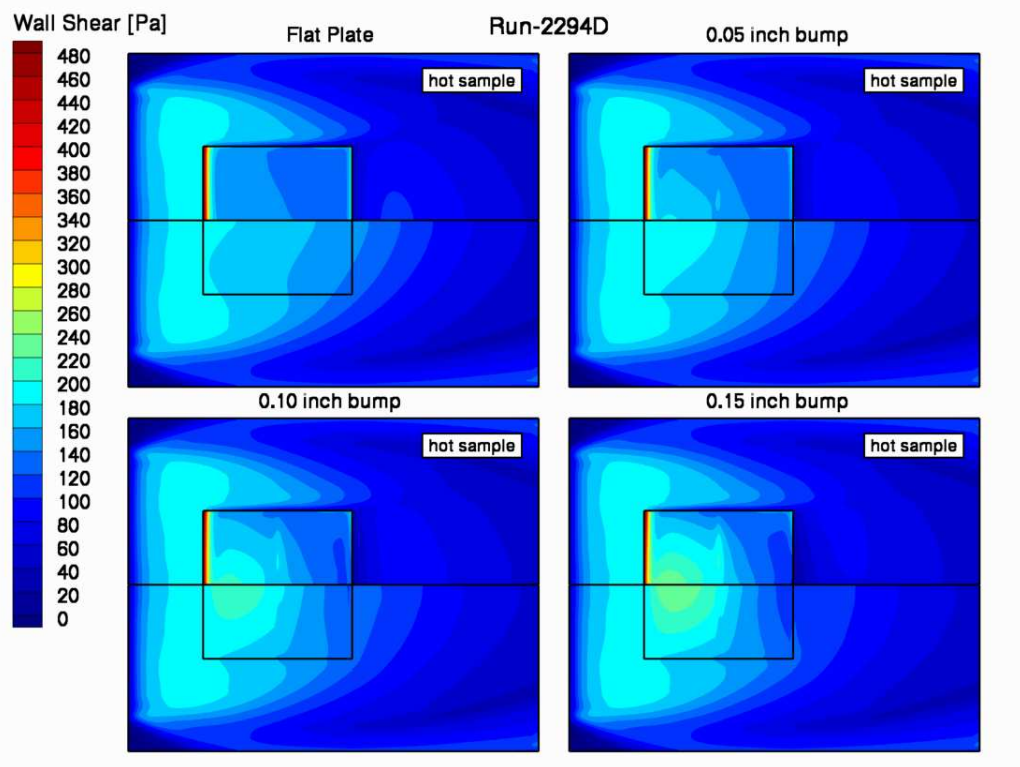

Figure 46:Run 2294D wall shear variation.

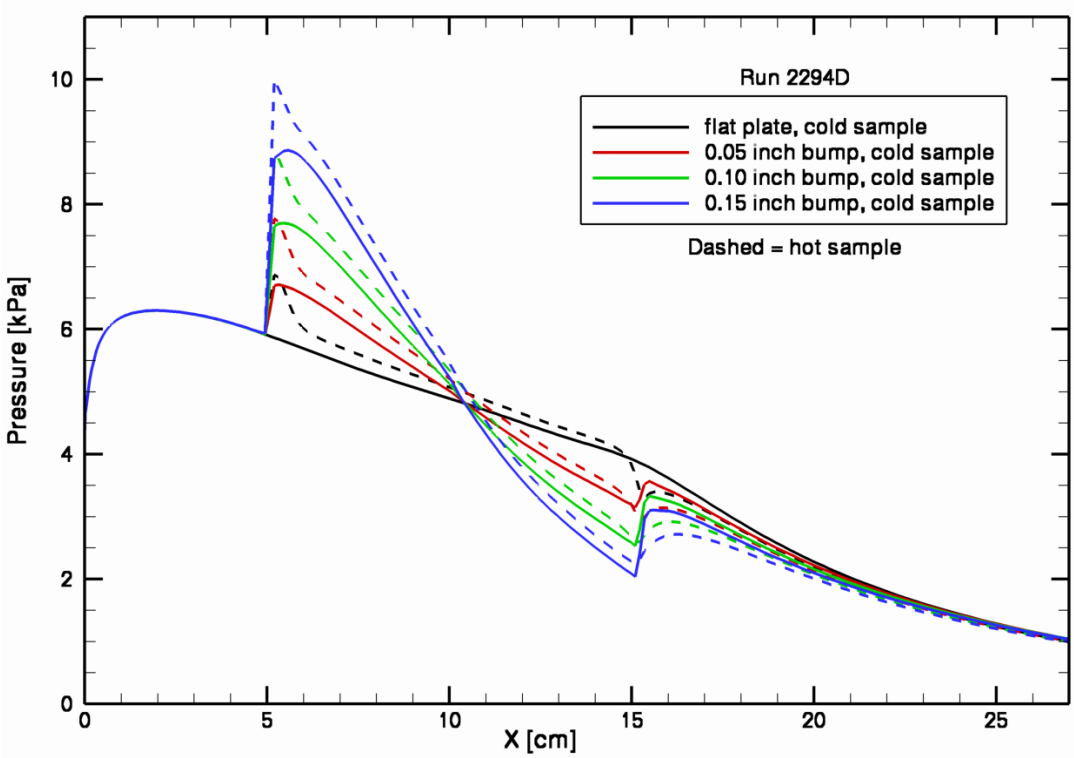

Figure 47: Run 2294D centerline pressure sensitivity to surface temperature and bump height.

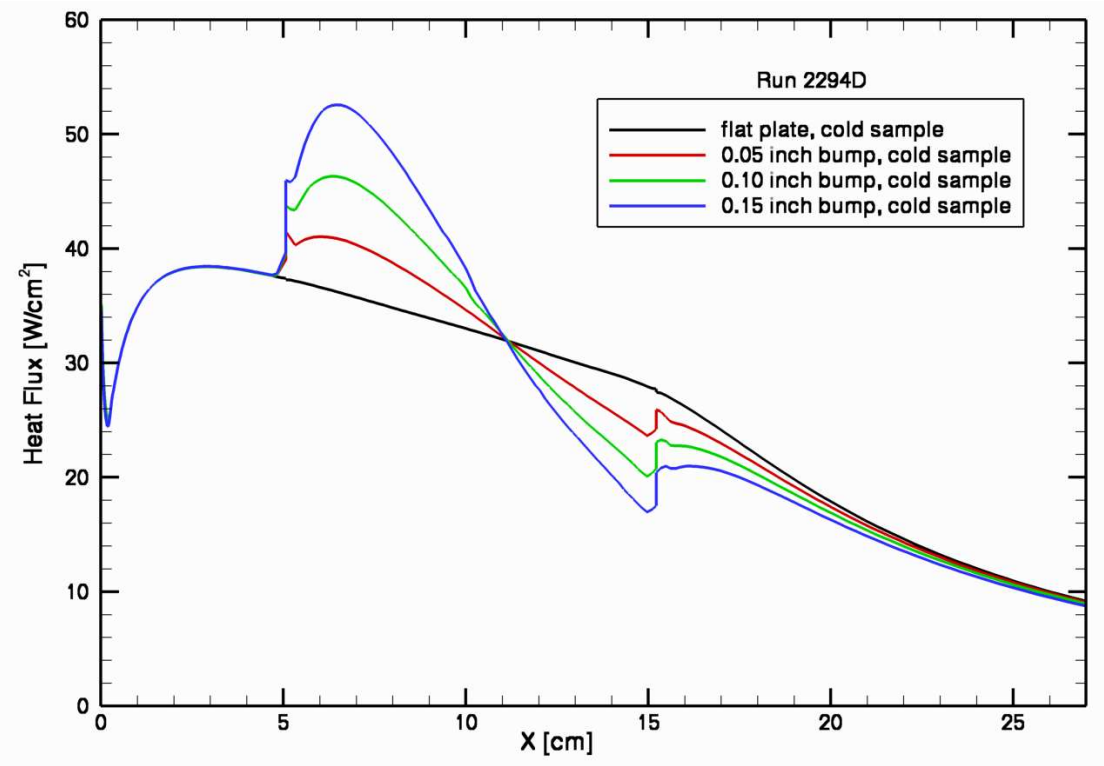

Figure 48: Run 2294D centerline cold wall heat flux sensitivity to bump height.

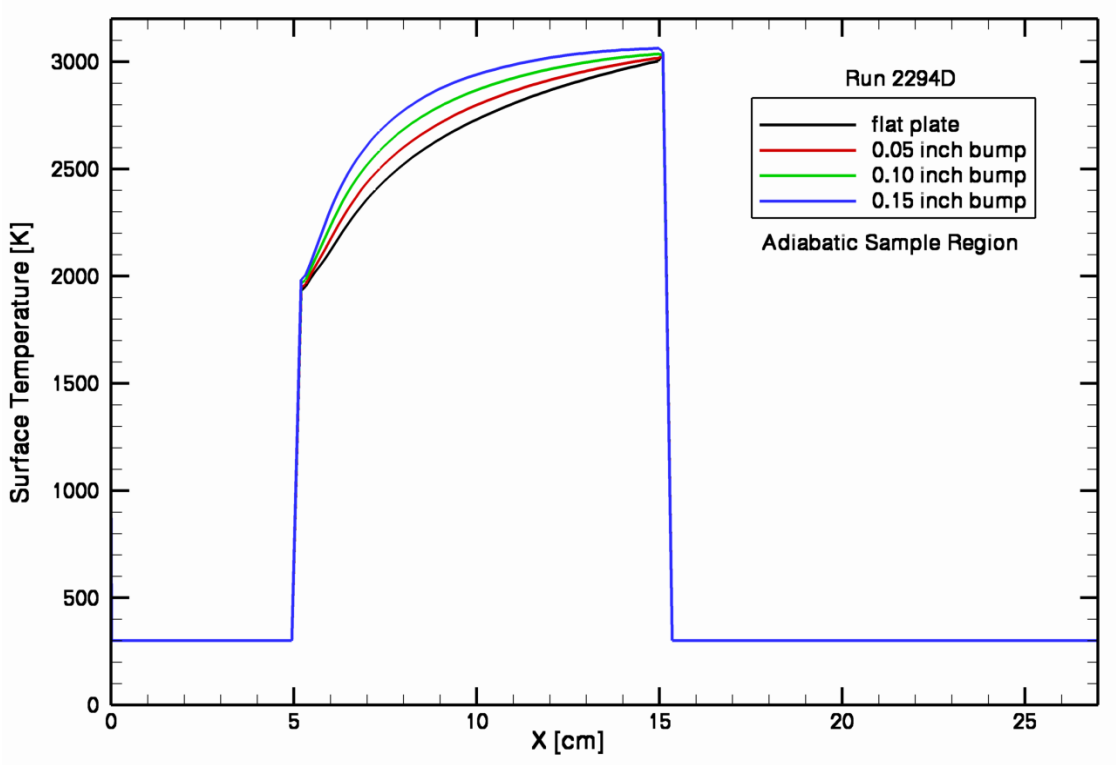

Figure 49: Run 2294D centerline adiabatic surface temperature sensitivity to bump height.

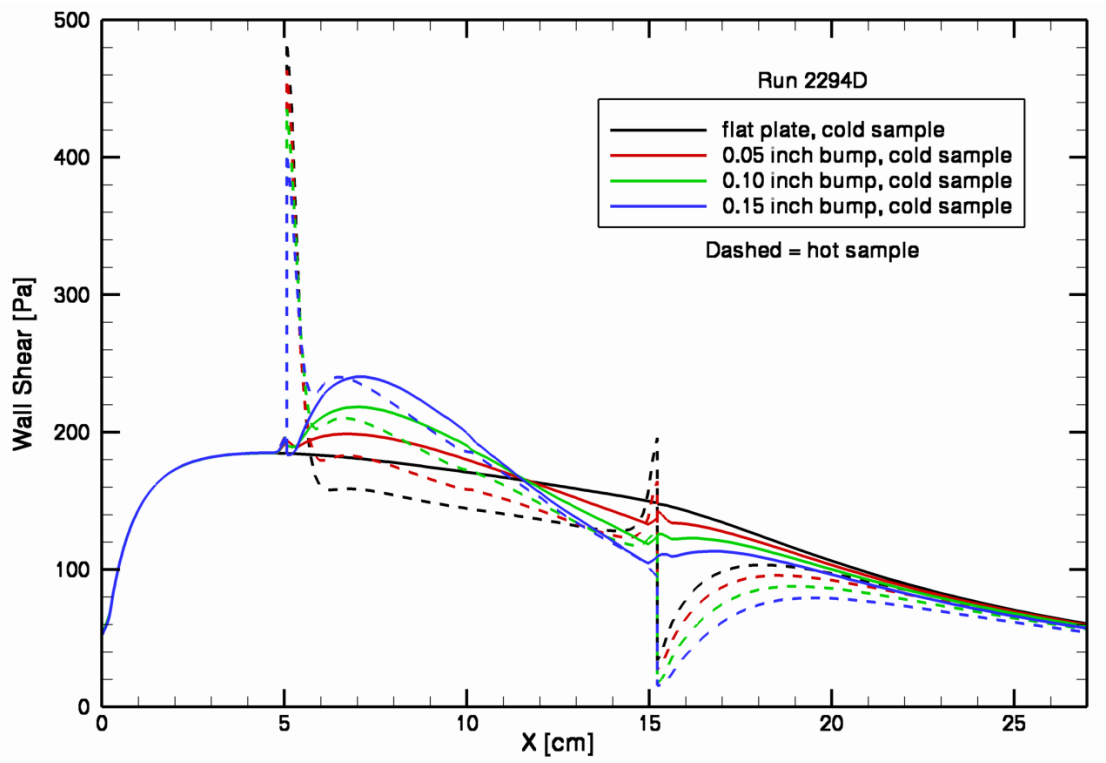

Figure 50: Run 2294D centerline wall shear sensitivity to wall temperature and bump height.

The pressure, heat flux, adiabatic wall temperature, and shear results from the previous four figures were extracted at the 3 instrumentation locations. Linear trends in pressure sensitivity to bump height and surface temperature are shown in Figure 51. The pressure at the center of the sample area is nearly insensitive to bump height. Linear trends are also predicted for cold wall heat flux and adiabatic surface temperature in Figures 52 and 53. The predicted wall shear trends are plotted in Figure 54. The difference between the cold wall and hot wall results decreases as the bump height increases. For the 0.15 inch bump, the wall shear becomes almost insensitive to surface temperature. Finally, the same wall shear results are plotted vs. surface temperature in Figure 55. This allows for the linear interpolation of wall shear predictions to other surface temperatures for each bump size at each measurement location.

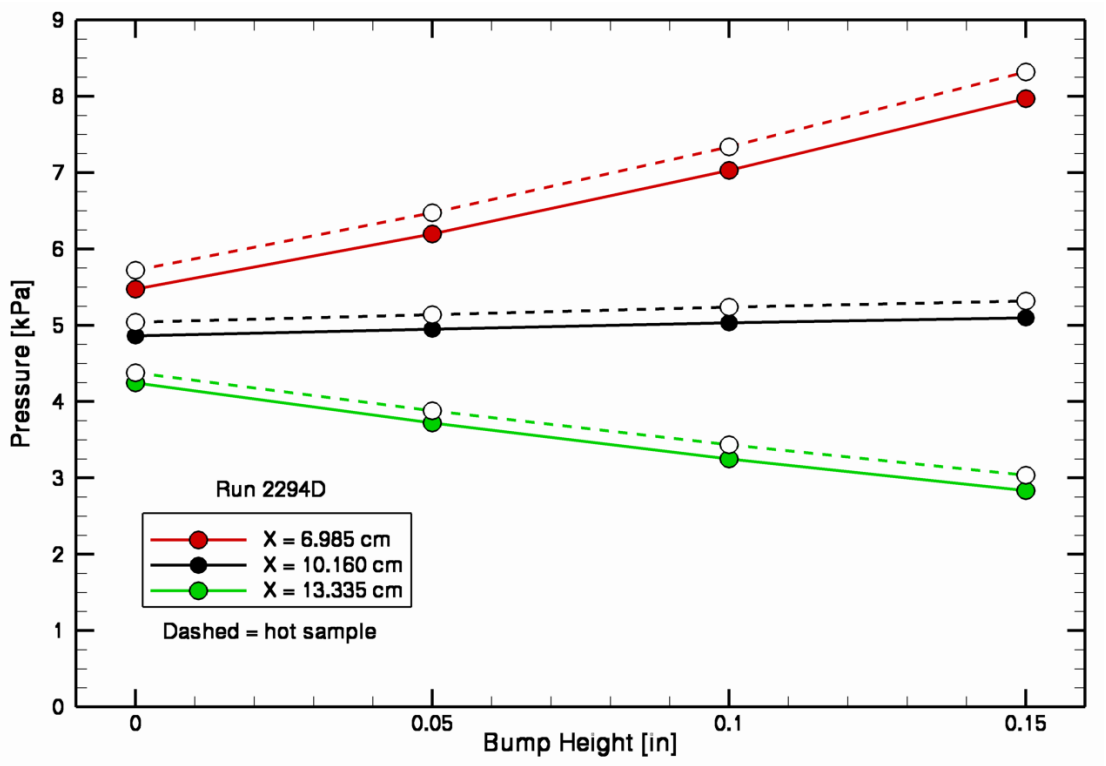

Figure 51: Run 2294D pressure sensitivity to wall temperature and bump height.

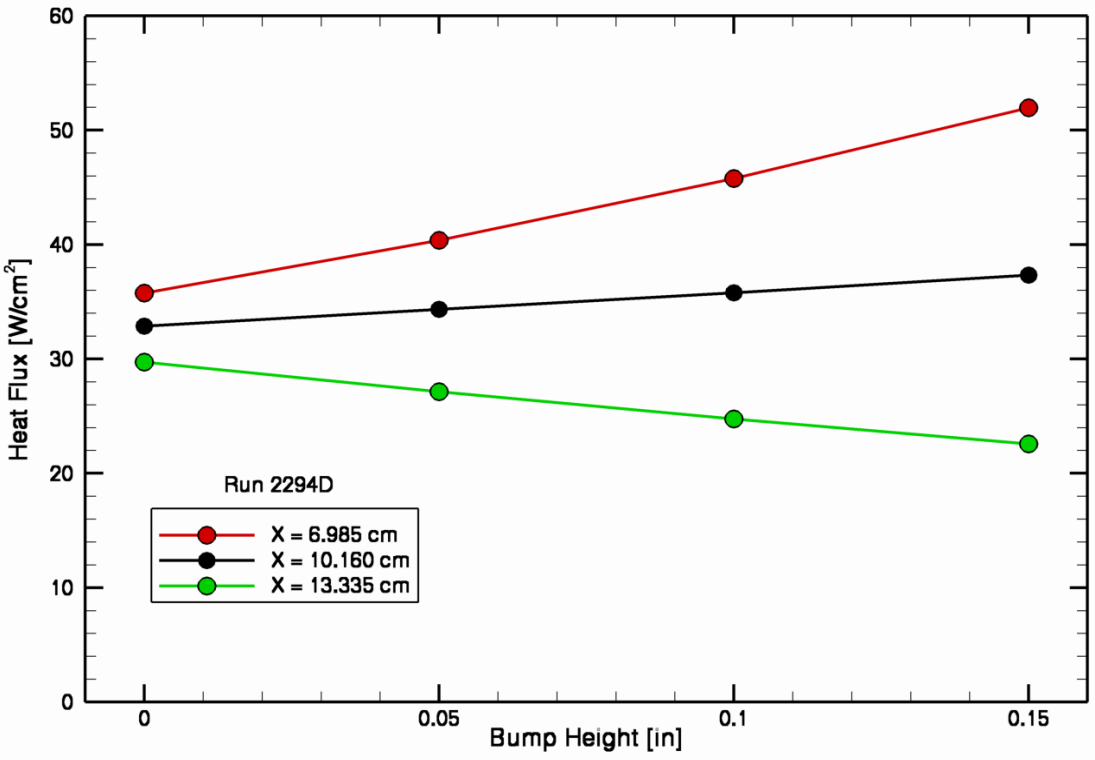

Figure 52: Run 2294D cold wall heat flux sensitivity to bump height.

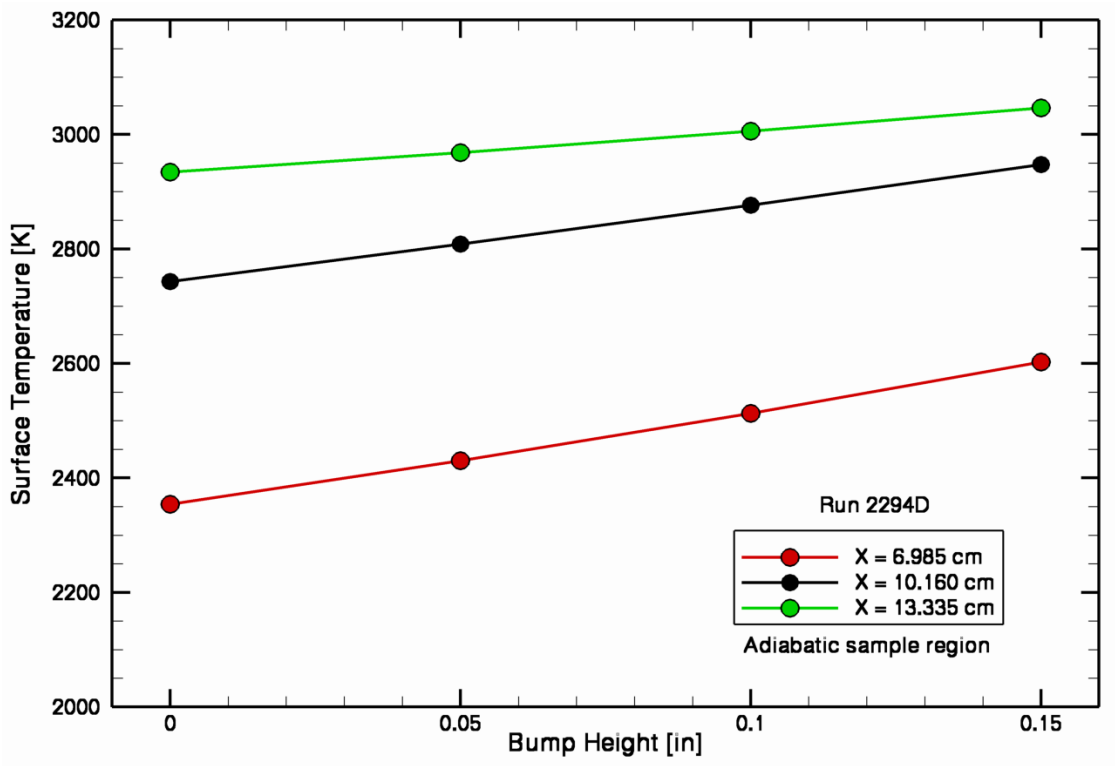

Figure 53: Run 2294D adiabatic surface temperature sensitivity to bump height.

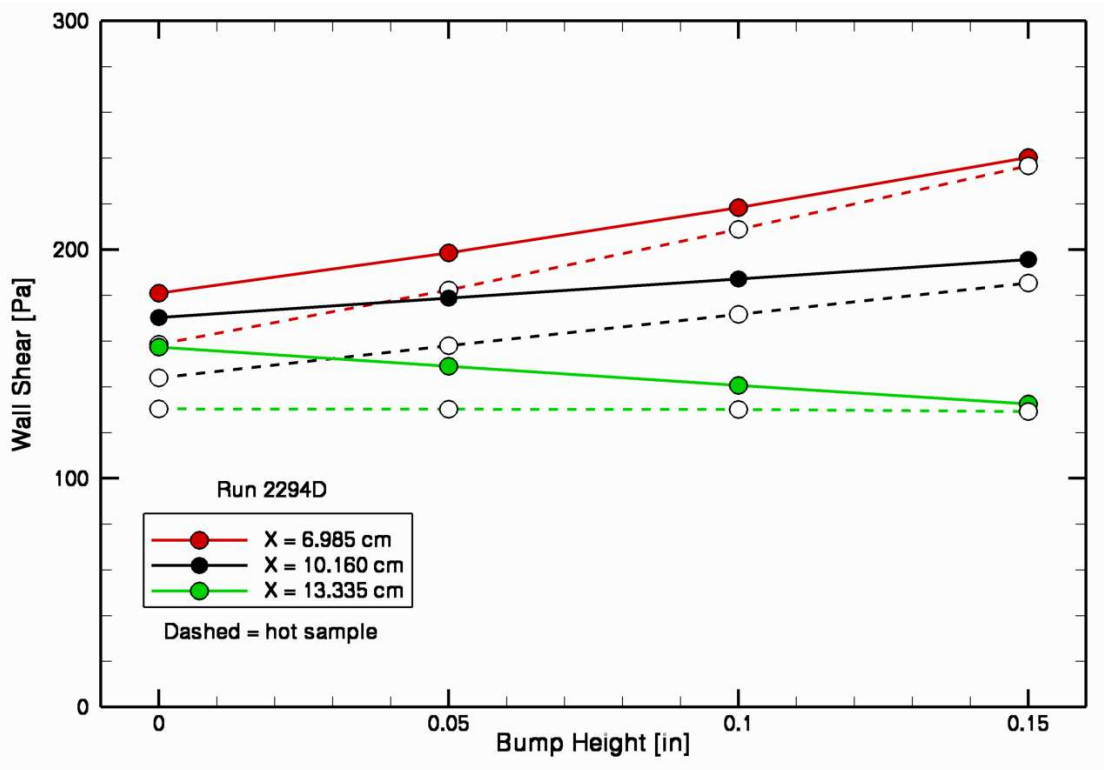

Figure 54: Run 2294D wall shear sensitivity to bump height.

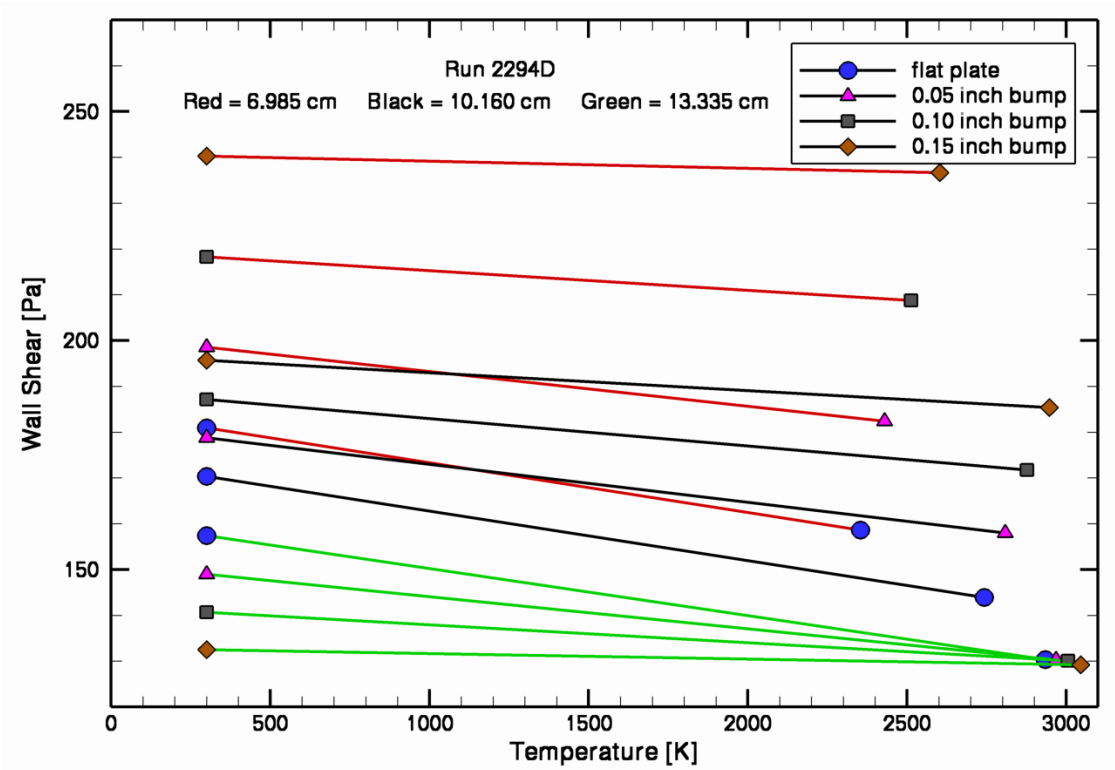

Figure 55: Run 2294D wall shear sensitivity to surface temperature.

Boundary layer parameters are included in the next 14 figures. The boundary layer thickness variation and centerline comparisons are included in Figures 56 and 57. Along the centerline the boundary layer thickness is predicted to continuously increase for the flat plat. The introduction of a bump reduces the boundary layer thickness on the upstream side and thickens it on the downstream side. Figures 58 and 59 show the boundary layer displacement thickness variation and centerline results. Compared to the bump results for Run 2294B, at this test condition the displacement thickness drops significantly downstream of the TPS sample area. The predicted boundary layer momentum thickness is plotted in Figures 60 and 61. Boundary layer enthalpy thickness results are included in Figures 62 and 63. The Stanton number variations and centerline comparisons are shown in Figures 64 and 65. Skin friction coefficient results are included in Figures 66 and 67. The non-dimensional heat flux and skin friction coefficients were used to create the Reynold's analogy factor information in Figures 68 and 69. For the sample area, these results are very similar to the analogy factor for the Run 2294B test condition.

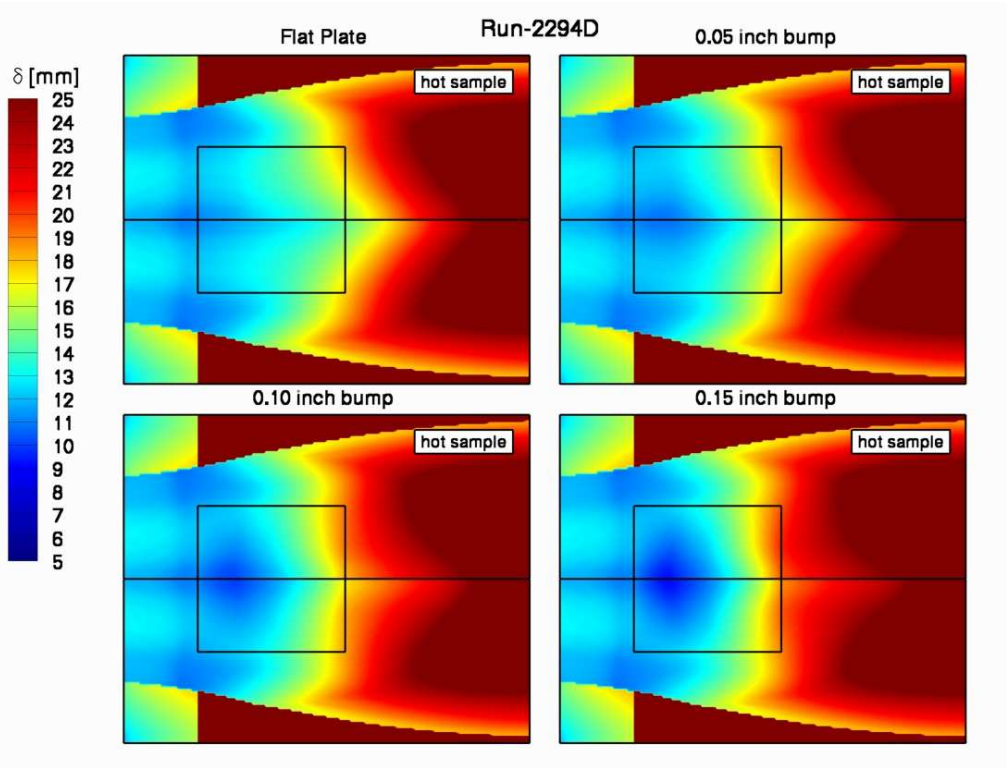

Figure 56: Run 2294D boundary layer thickness variation.

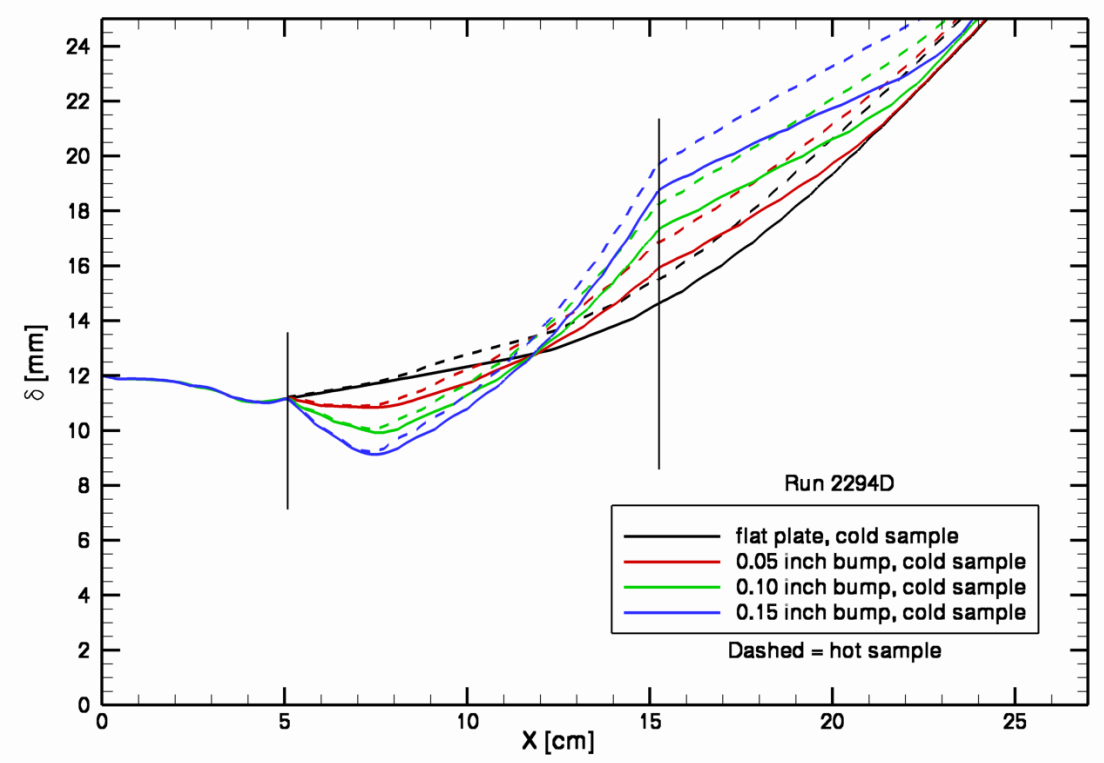

Figure 57: Run 2294D centerline boundary layer thickness comparison.

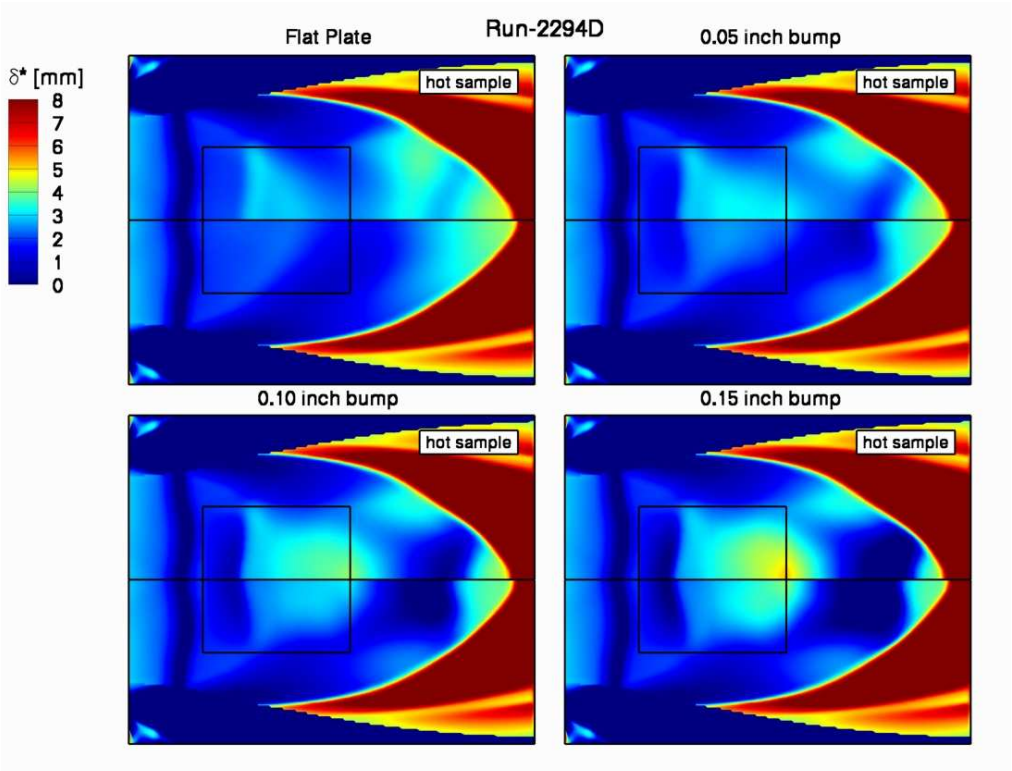

Figure 58: Run 2294D boundary layer displacement thickness variation.

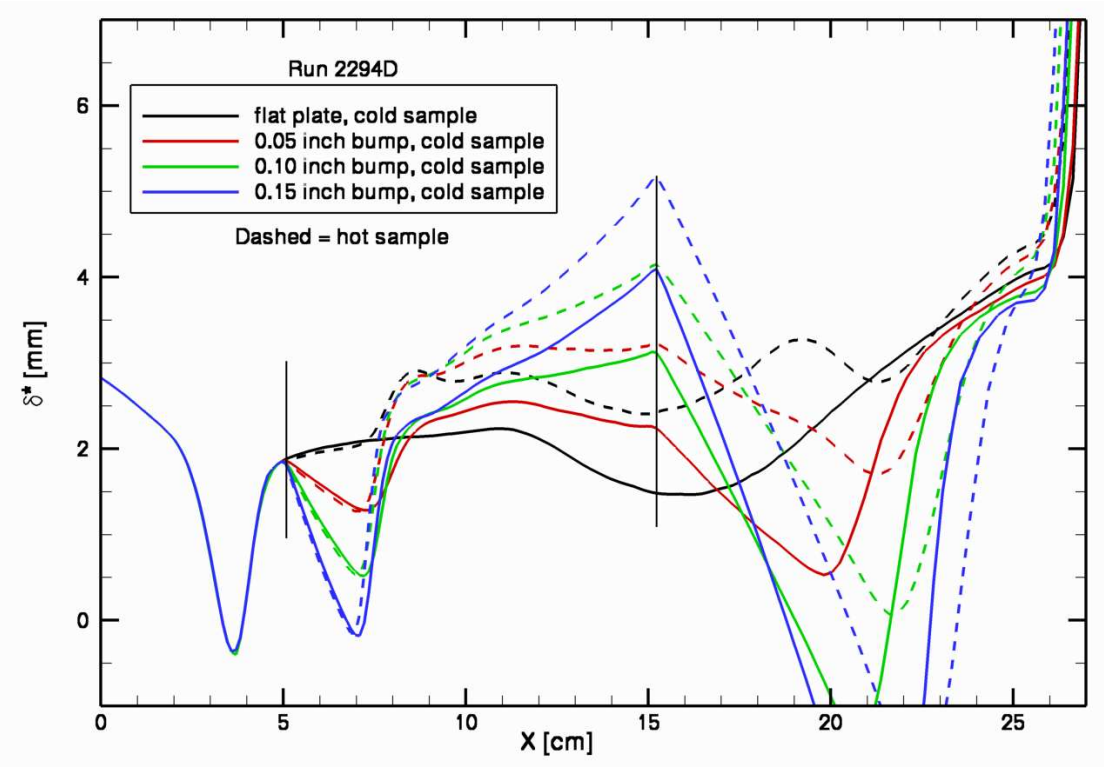

Figure 59:Run 2294D centerline boundary layer displacement thickness comparison.

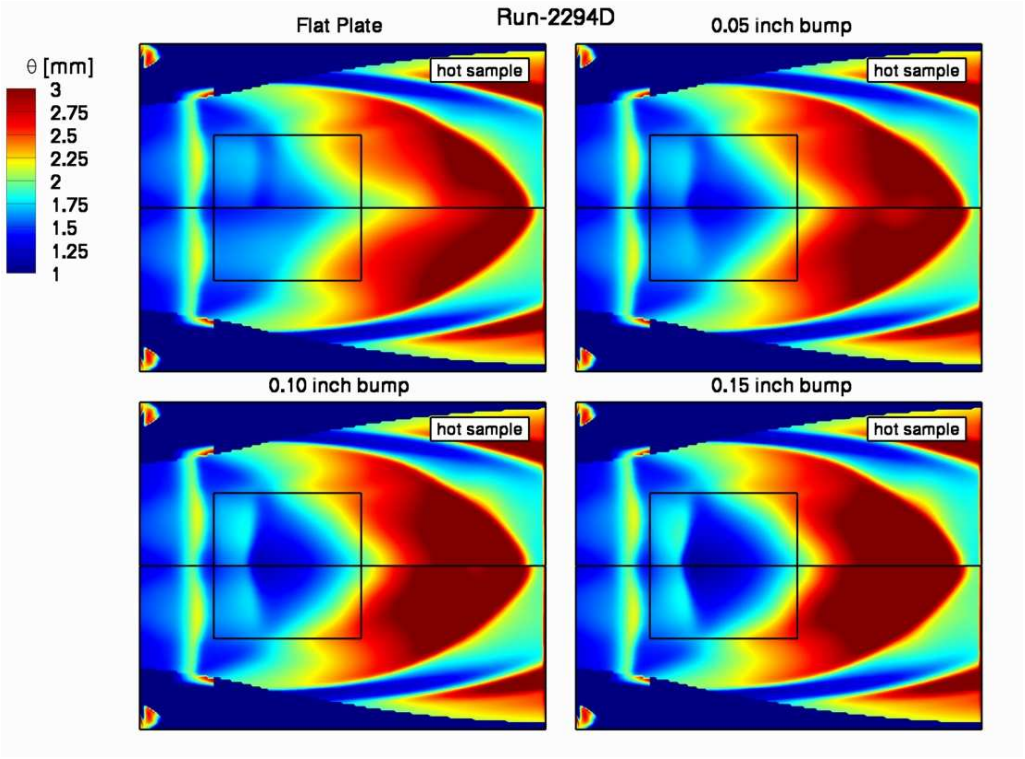

Figure 60: Run 2294D boundary layer momentum thickness variation.

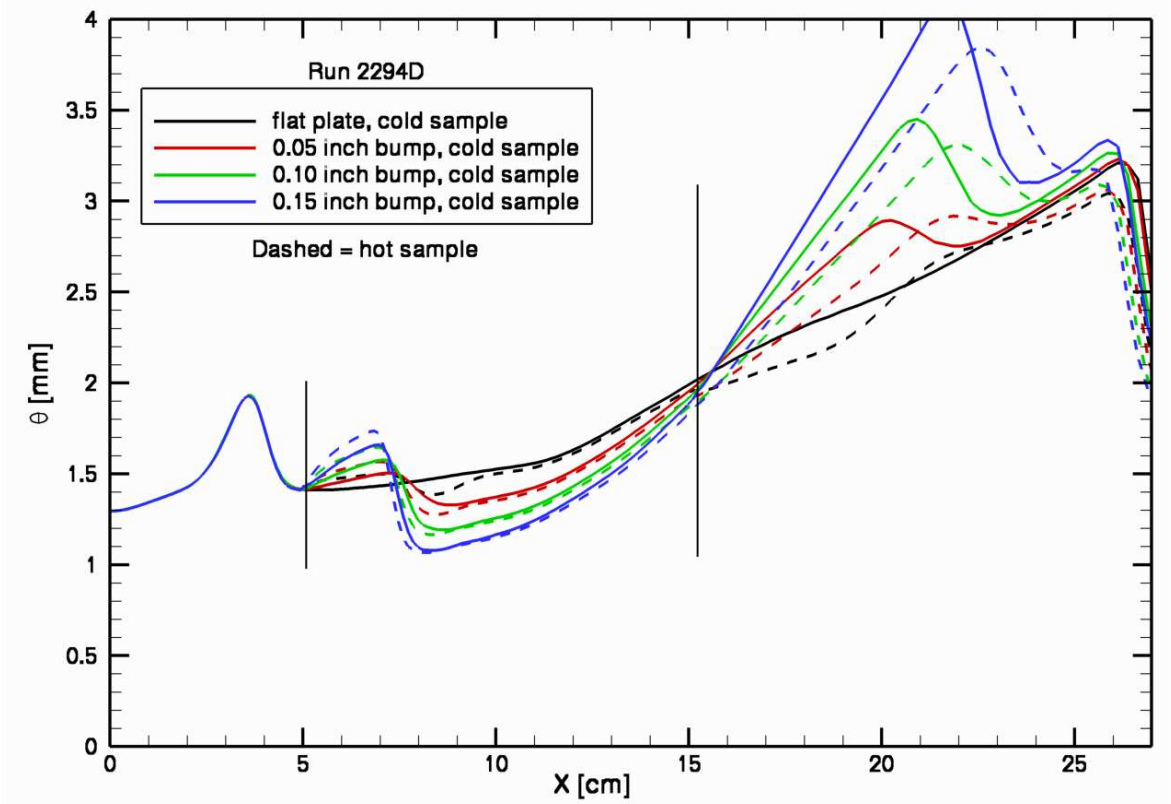

Figure 61: Run 2294D centerline boundary layer momentum thickness comparison.

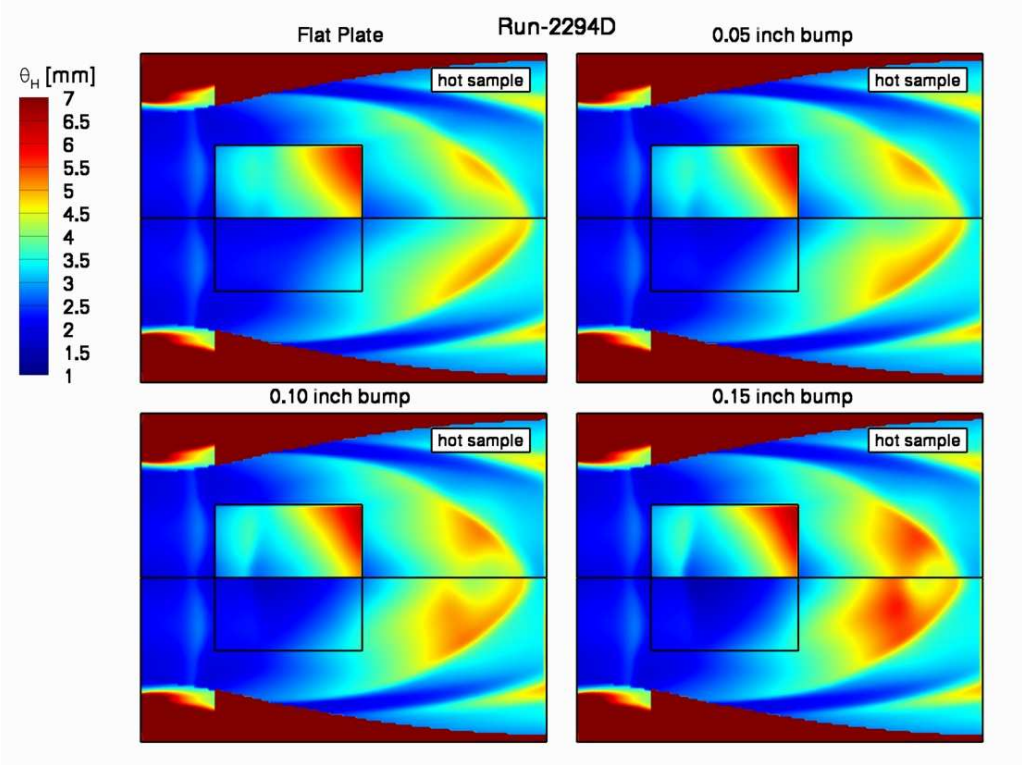

Figure 62: Run 2294D boundary layer enthalpy thickness variation.

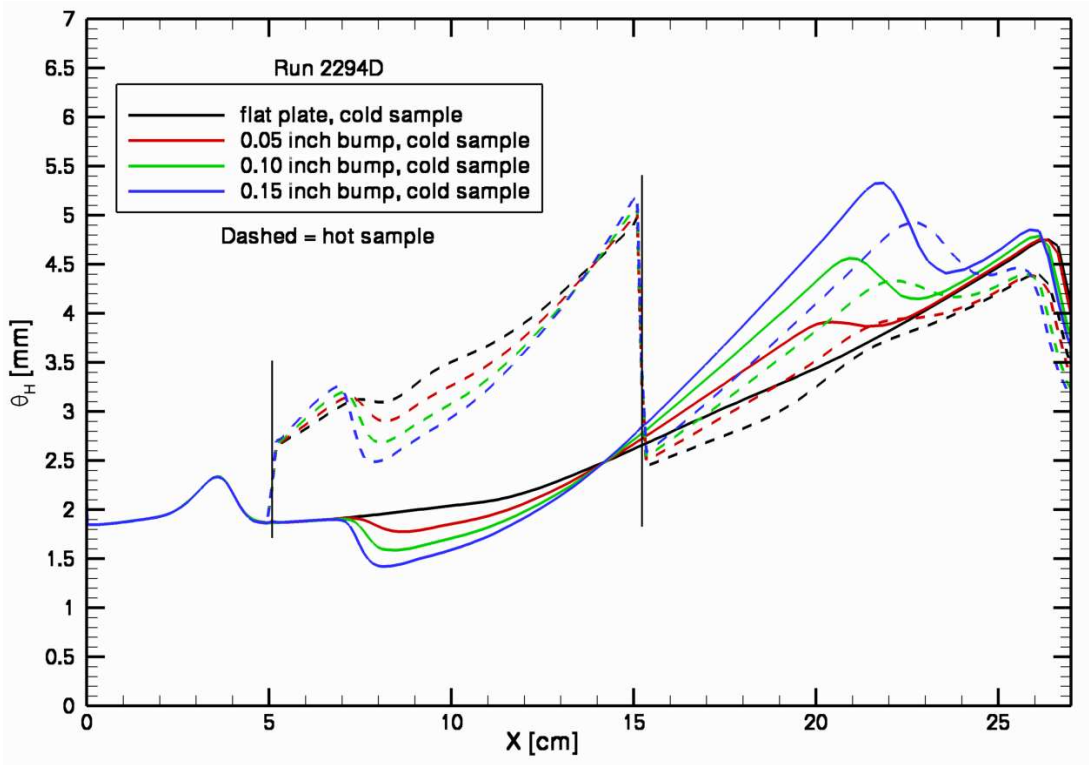

Figure 63: Run 2294D centerline boundary layer enthalpy thickness comparison.

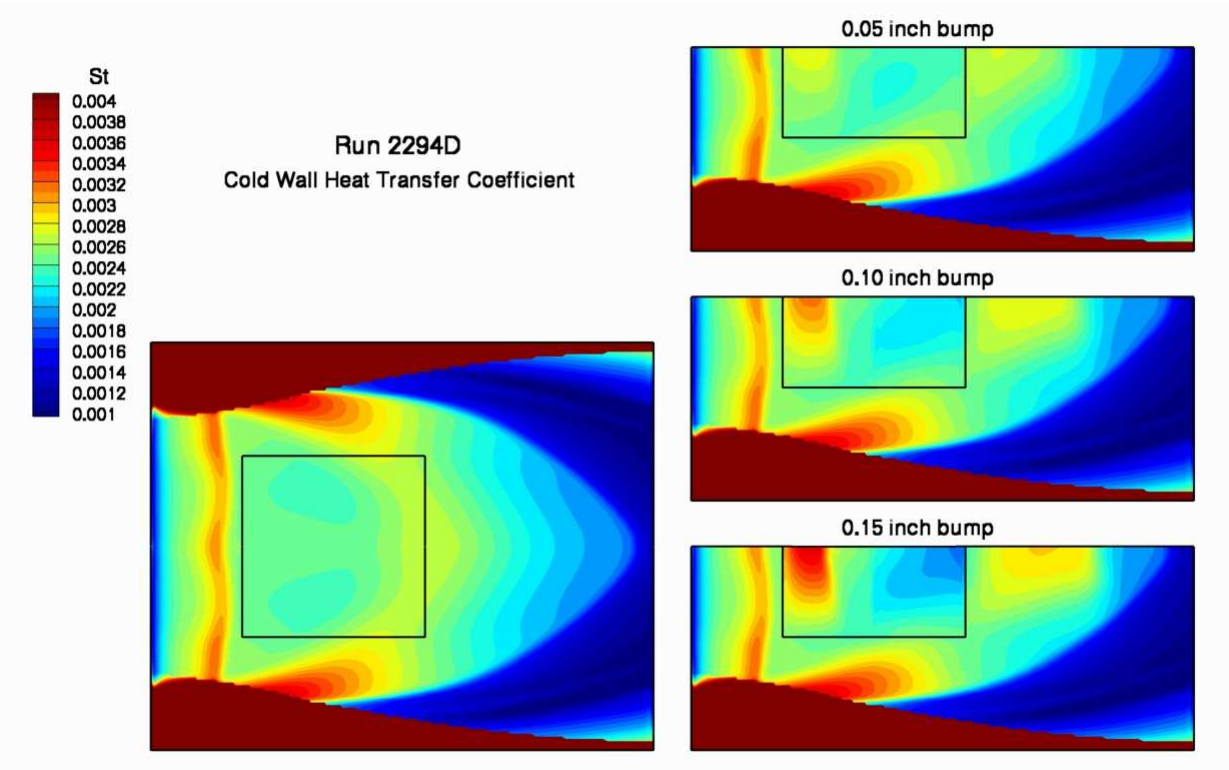

Figure 64: Run 2294D heat transfer coefficient variation.

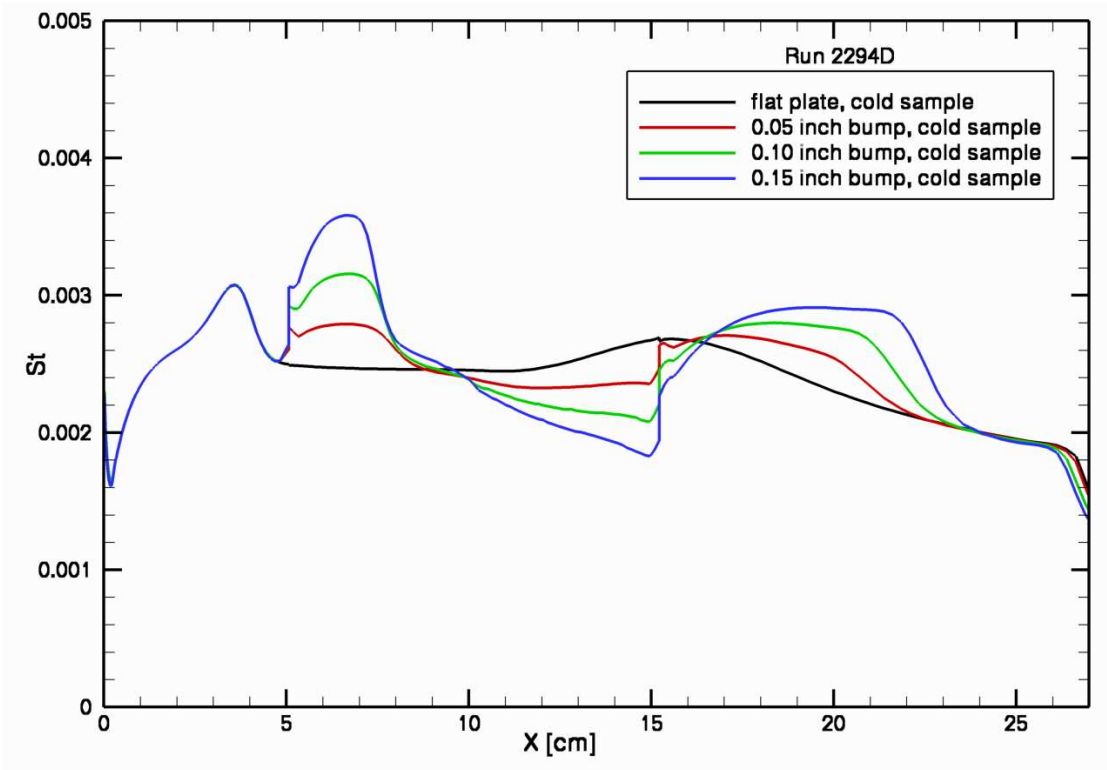

Figure 65: Run 2294D centerline heat transfer coefficient variation.

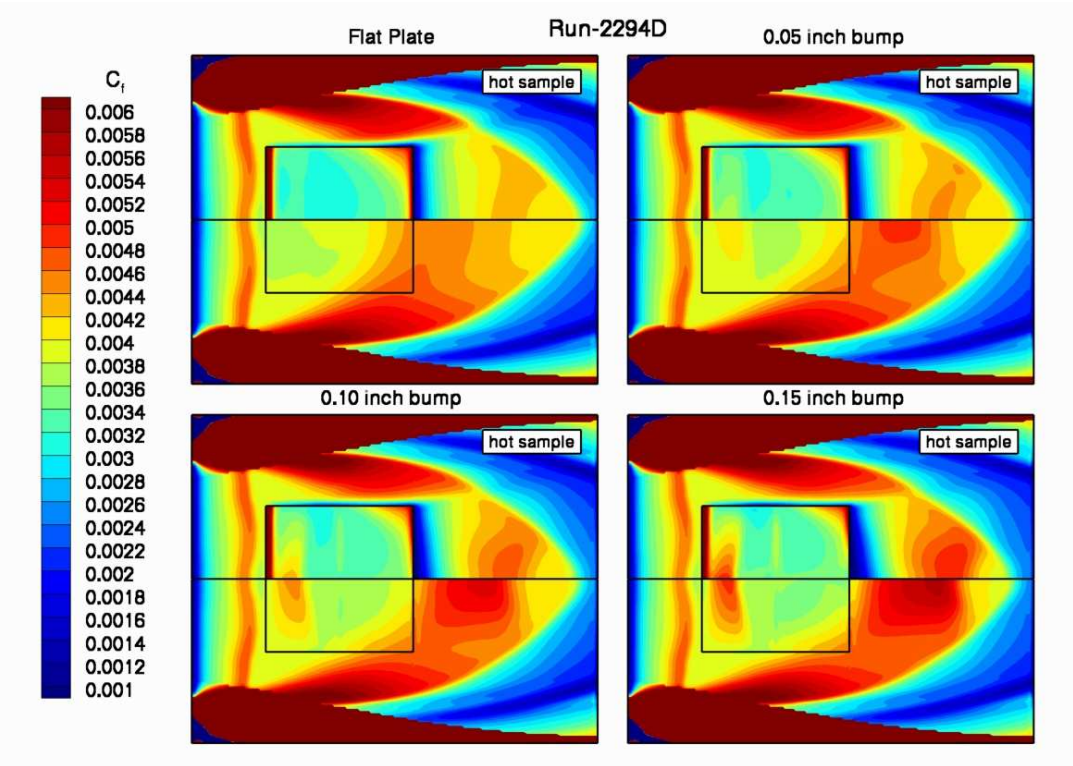

Figure 66: Run 2294D skin friction coefficient variation.

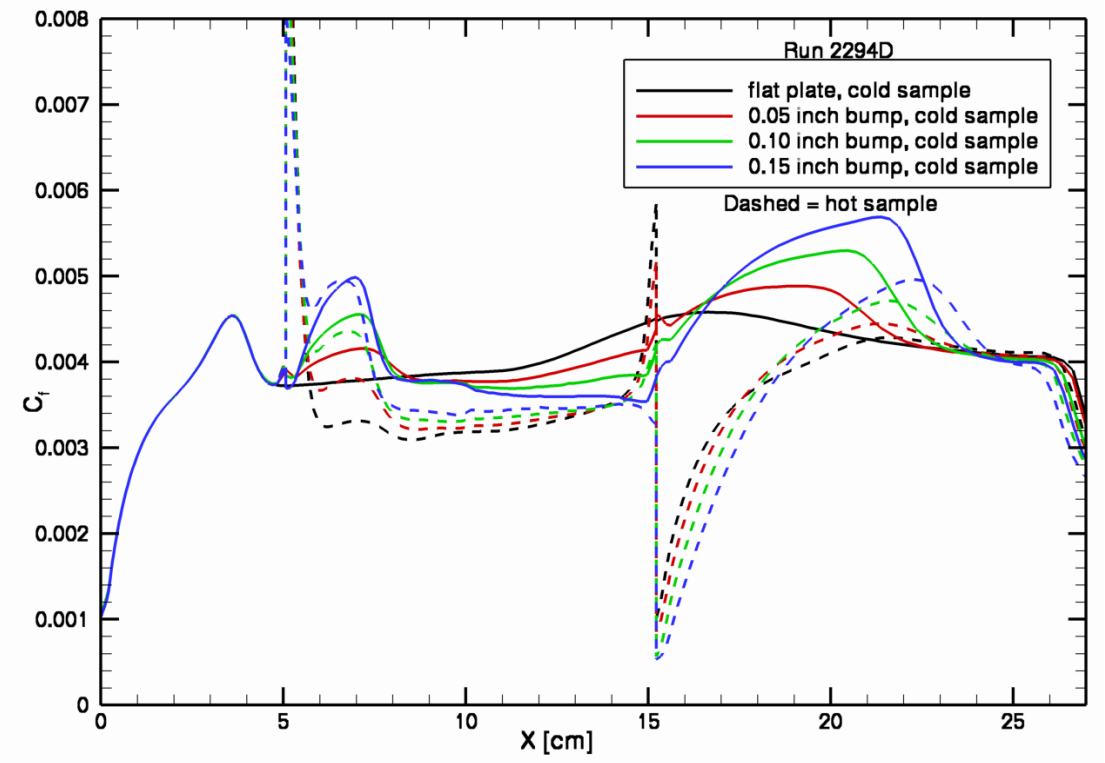

Figure 67: Run 2294D centerline skin friction coefficient comparison.

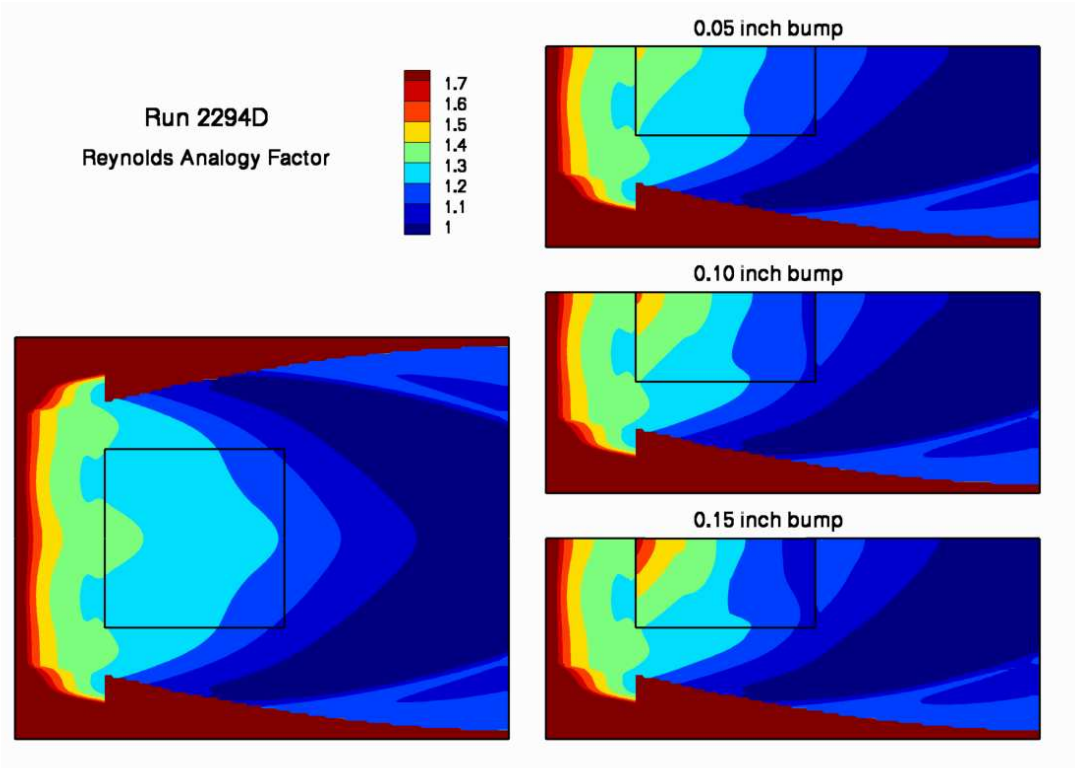

Figure 68: Run 2294D Reynolds analogy variation.

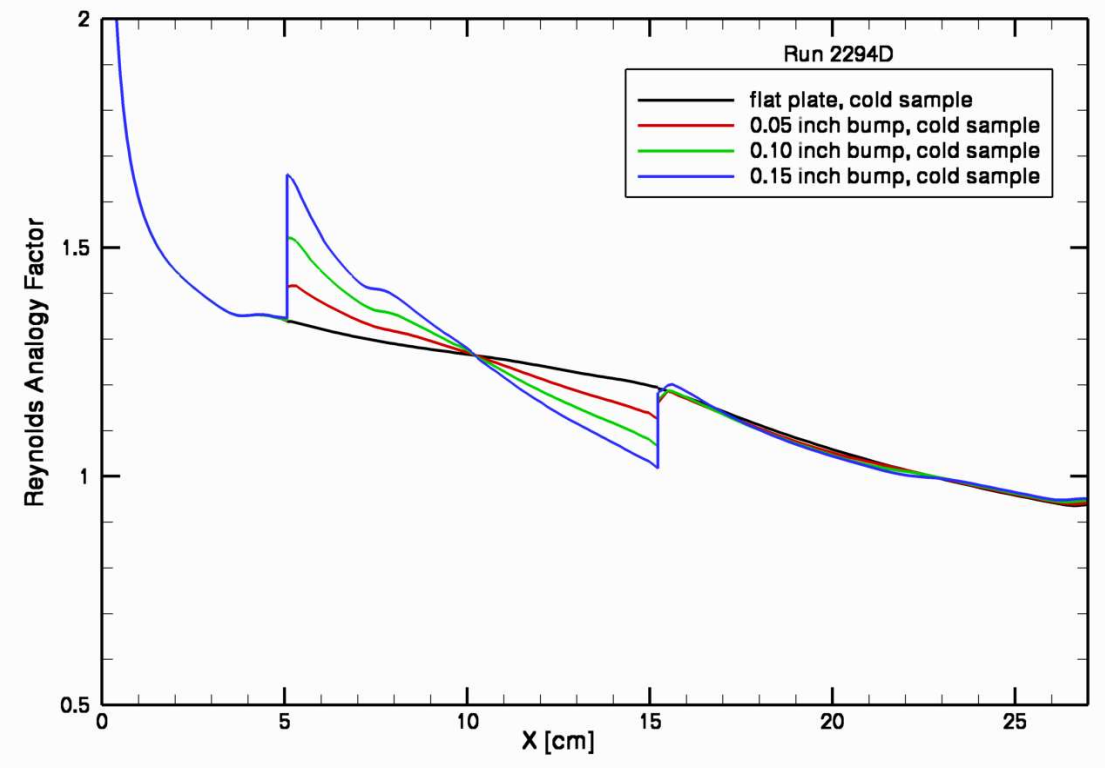

Figure 69: Run 2294D centerline Reynolds analogy factor comparison.

Results for Run 2294E

For target conditions of 6.6 kPa / 40 W/cm^2, the experimental and computational conditions are listed in Table 4. For this condition the computational model required 81% of the experimentally reported mass flow and the greatest difference (+7.6%) in nozzle exit flow total enthalpy. A flat, cold wall shear of 216 Pa at the center of the sample was predicted for this test condition.

Table 4: Facility and calibration plate information for Run 2294E.

	Plenum Pressure (kPa)	Total Air Flow (kg/s)	Nozzle Exit Enthalpy (MJ/kg)	At Center of Calibration Plate		
				Pressure (kPa)	Heat Flux (W/cm^2)	Shear (Pa)
Experiment	1216[a]	0.348	5.254	6.55	41.0	N/A
CFD Model	980[b]	0.281	5.653			216

a.) at most upstream wall of heater.

b.) at entrance to facility nozzle throat section.

Streamwise and lateral comparisons with the experimental pressure data are shown in Figures 70 and 71. Similar to results at the Run 2294D condition, higher pressure is consistently measured off-centerline while the opposite is predicted by the CFD simulation. The first centerline pressure measurement is also lower than the second, while the simulation predicts a continuously decreasing pressure. All the pressure data is remarkably consistent with Run 2294D pressure data, just shifted upwards (compare to Figures 39 and 40).

The streamwise and lateral heat flux data, shown in Figures 72 and 73, also shows similar trends compared to the Run 2294D heat flux data (Figures 41 and 42). These include: lower heat flux along the centerline at the first measurement location compared to the center measurement, lower heat flux measured off-centerline at the second measurement location, and higher heat flux measured off-centerline at the third measurement location. The CFD simulation predicts continuously decreasing heat flux axially and lower heat flux off-centerline.

The same facility nozzle exit flow was used to perform seven more simulations. These included cold wall predictions for three bump geometries and each geometry solved with an adiabatic wall boundary condition for the TPS sample region. The variations in surface pressure are plotted in Figure 74. The total variation over the sample area was 3.9 – 8.0 kPa for the flat plate. The pressure is higher than Run 2294D, otherwise the flow characteristics are the same. The cold wall heat flux variation, shown in Figure 75, reveals a total variation of 28 – 46 W/cm^2 over the flat plate sample area.

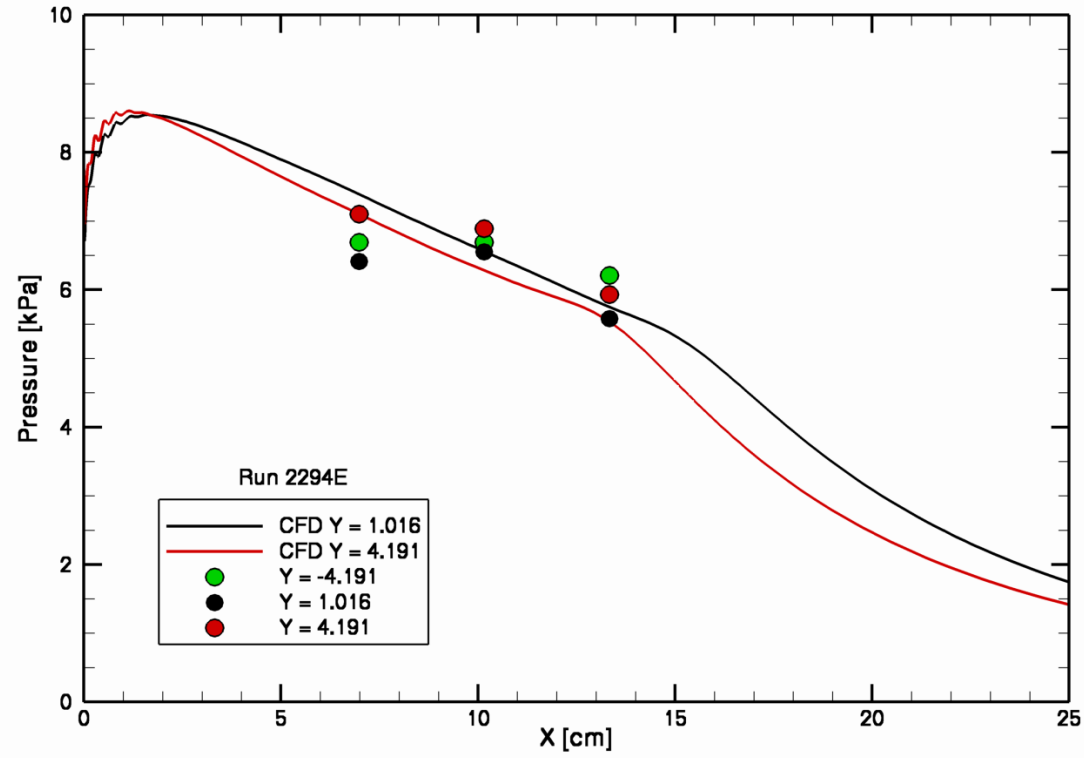

Figure 70: Streamwise comparison with Run 2294E calibration plate pressure data.

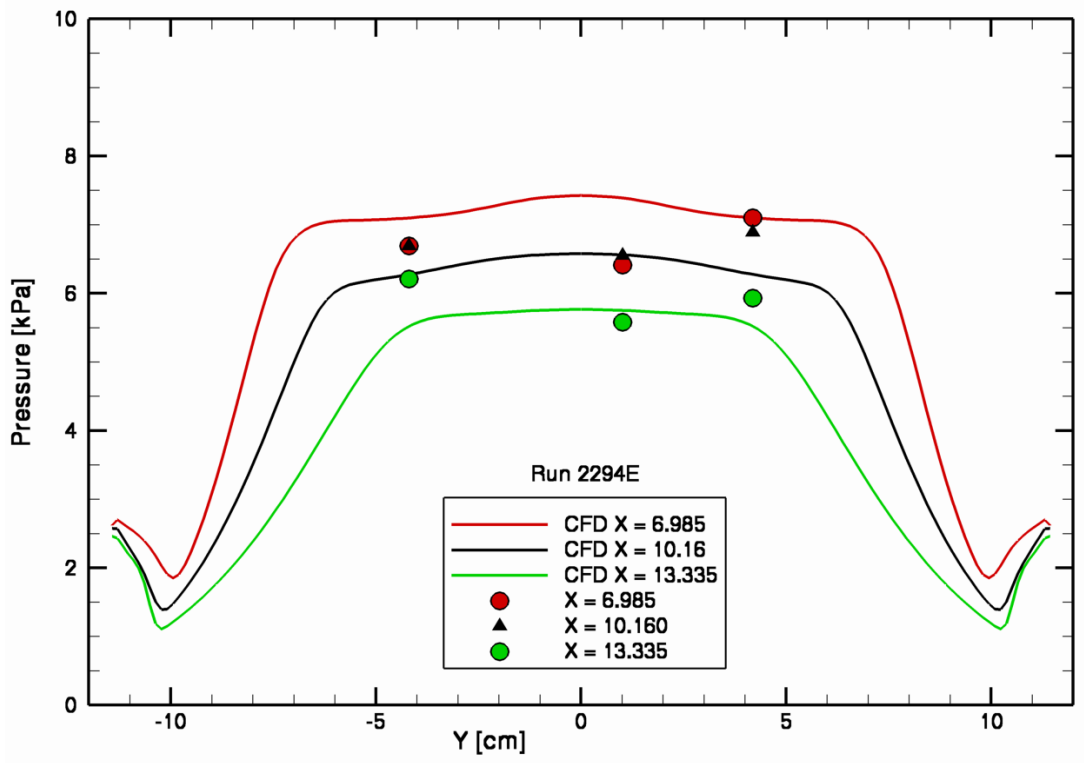

Figure 71: Lateral comparison with Run 2294E calibration plate pressure data.

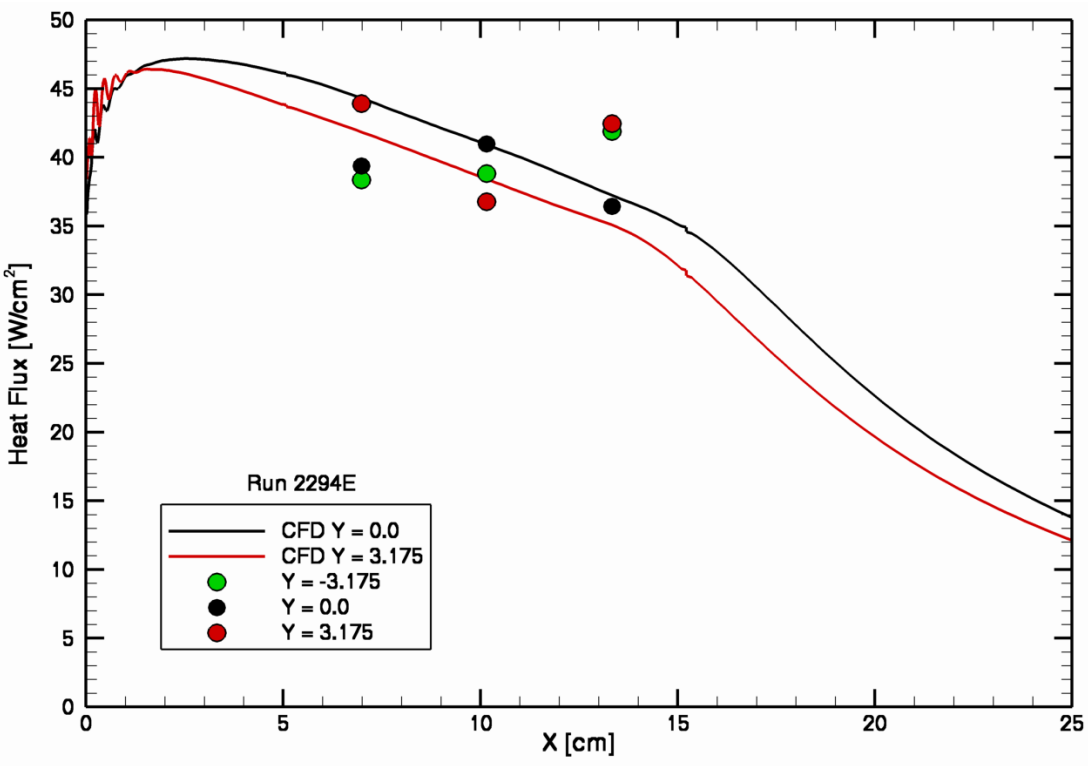

Figure 72: Streamwise comparison with Run 2294E cold wall heat flux data.

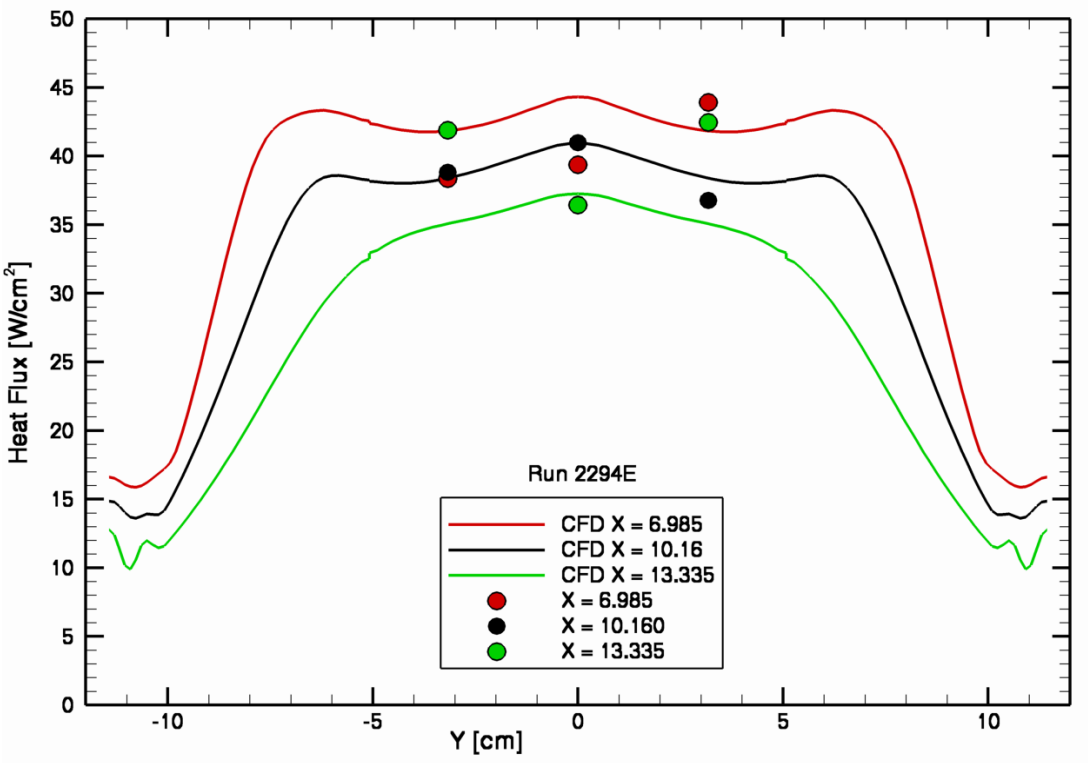

Figure 73: Lateral comparison with Run 2294E cold wall heat flux data.

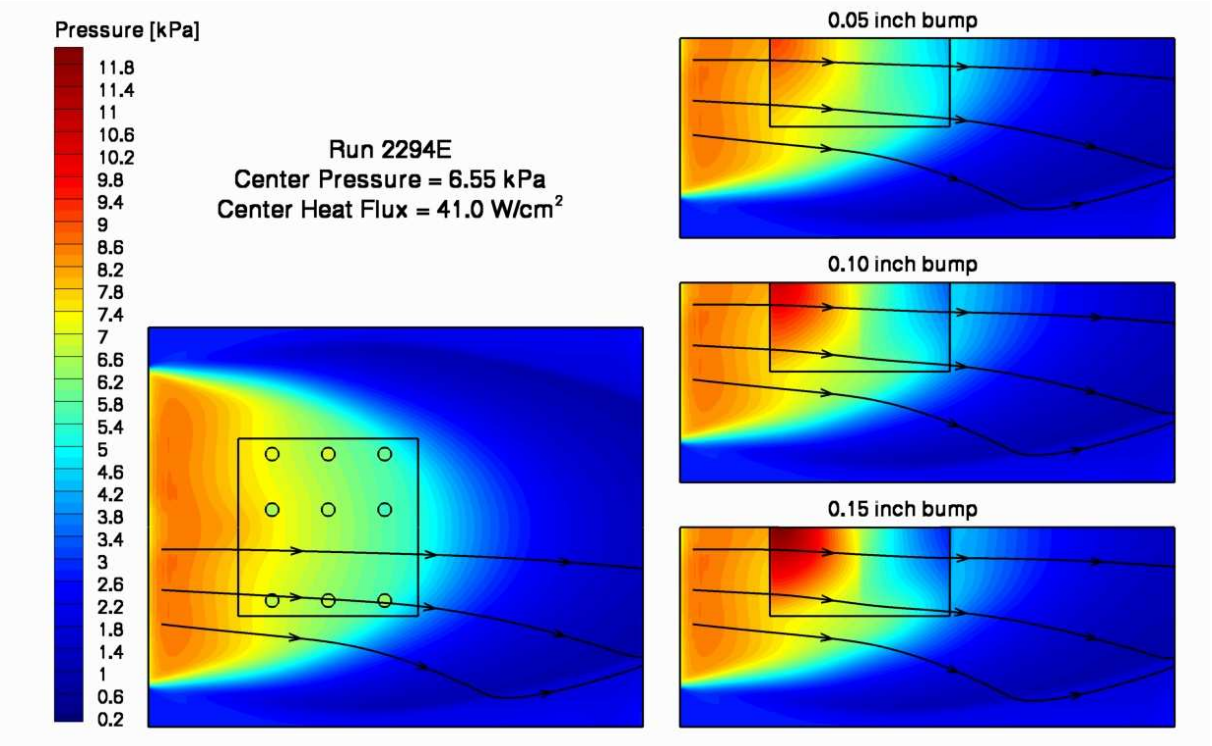

Figure 74: Run 2294E surface pressure variation (CFD inflow calibrated using center measurement).

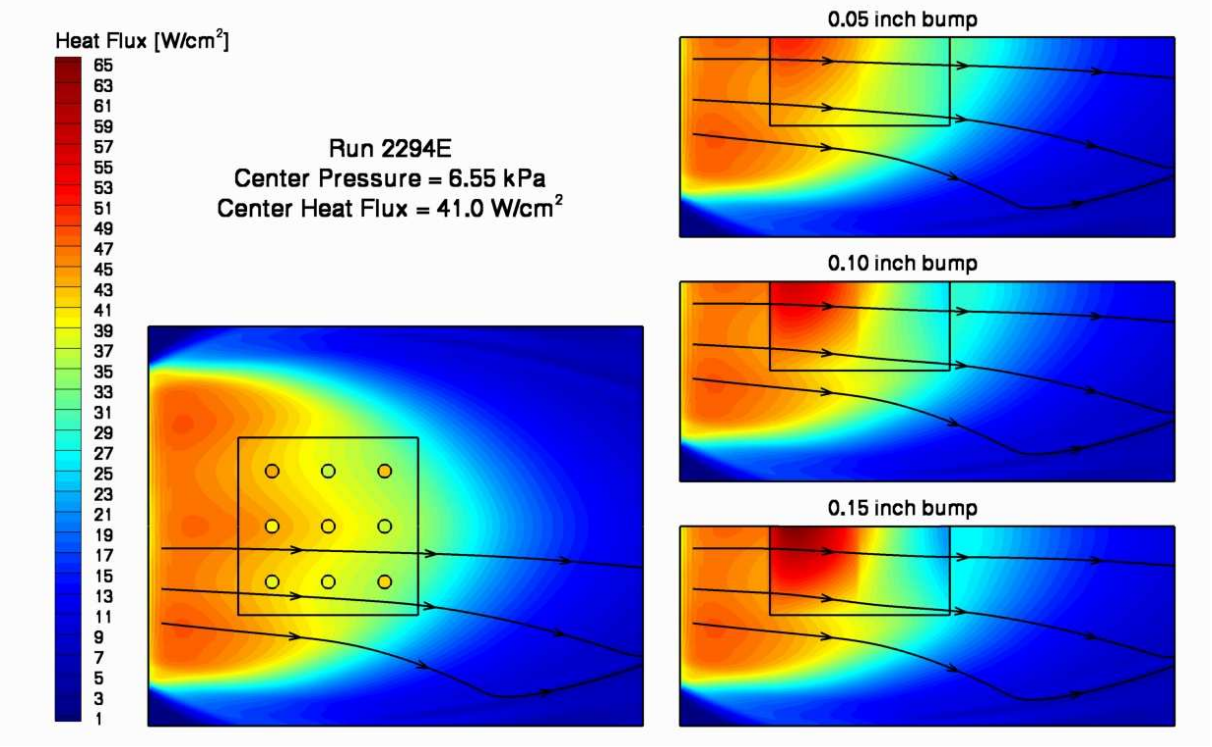

Figure 75: Run 2294E cold wall heat flux variation (CFD inflow calibrated using center measurment).

A simulation was completed for each geometry with an adiabatic wall boundary condition for the TPS sample area rather than a specified cold wall temperature. The predicted adiabatic surface temperature variations are shown in Figure 76. The peak temperature occurs at the centerline at the end of the sample.

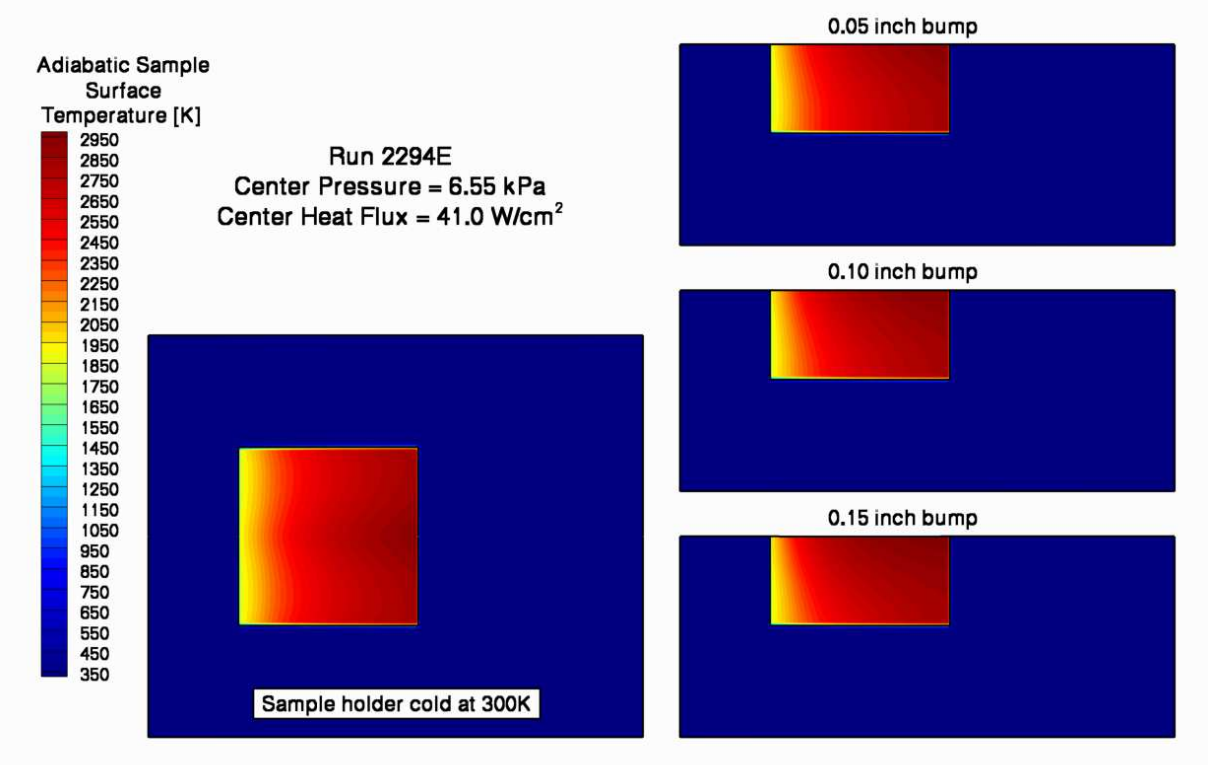

Figure 76: Run 2294E adiabatic surface temperature variation.

The wall shear predictions for all eight simulations at this test condition are shown in Figure 77. Following a spike at the leading edge of the sample, a hot surface temperature reduces the predicted wall shear to the majority of the sample area. An increasing bump height increases the shear on the forward facing region of the bump and decreases it on the downstream side.

Centerline distributions have been extracted from each of the preceding four figures. The pressure, cold wall heat flux, adiabatic wall temperature, and wall shear are included in Figures 78 - 81.

The results from the previous four figures were extracted at the three measurement locations. As with the previous test conditions, Figures 82 - 85 show linear trends with bump height for pressure, heat flux, adiabatic wall temperature, and shear. Figure 86 facilitates the interpolation of wall shear to intermediate surface temperatures at each measurement location for each bump height.

Boundary layer parameters are included in the next 14 figures (87 - 100). The results are quite similar to the Run 2294D results and will not be discussed in detail, but are included for completeness.

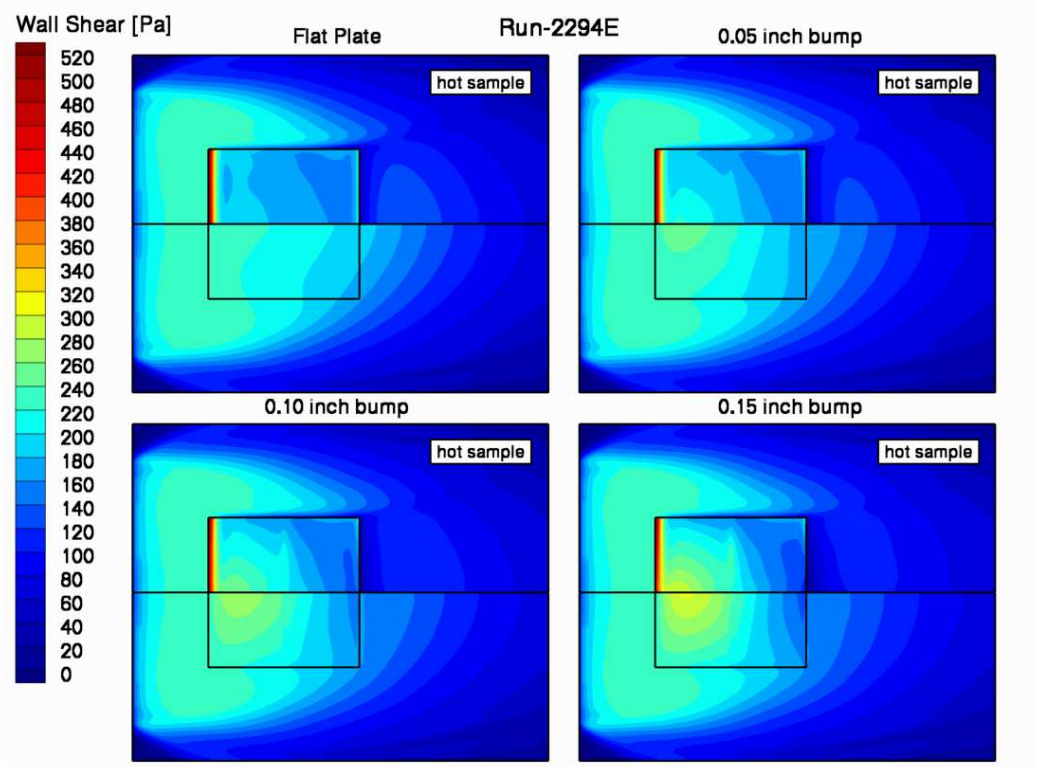

Figure 77: Run 2294E wall shear variation.

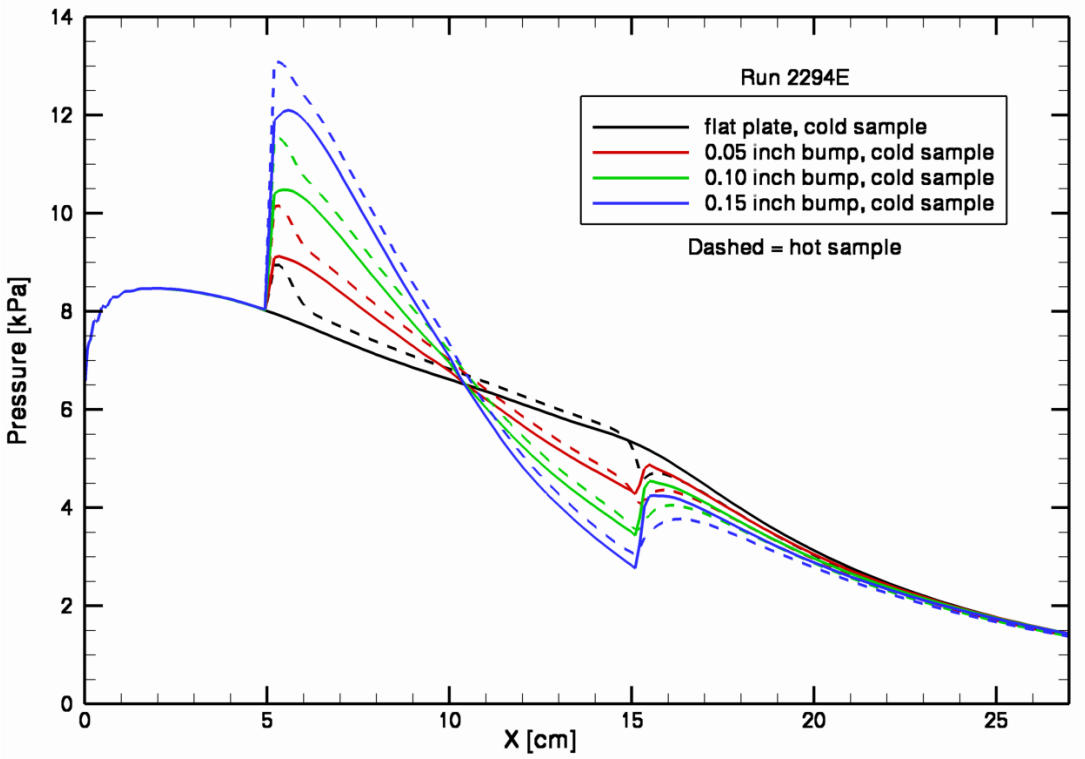

Figure 78: Run 2294E centerline pressure sensitivity to surface temperature and bump height.

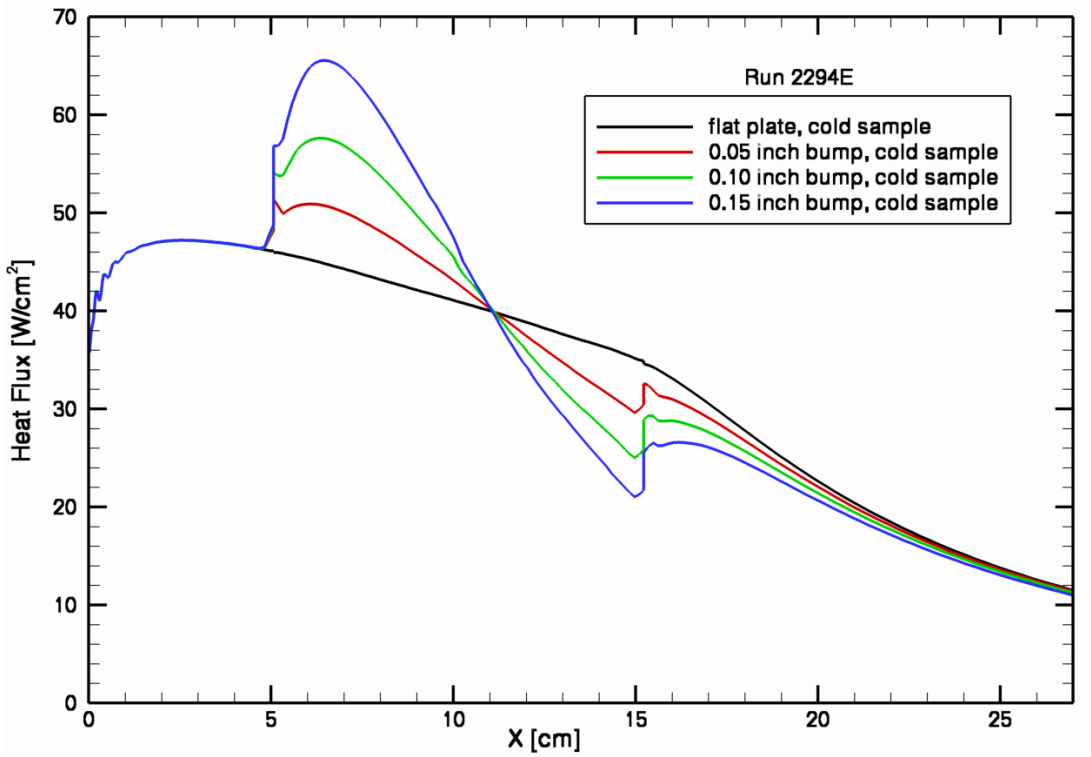

Figure 79: Run 2294E centerline cold wall heat flux sensitivity to bump height.

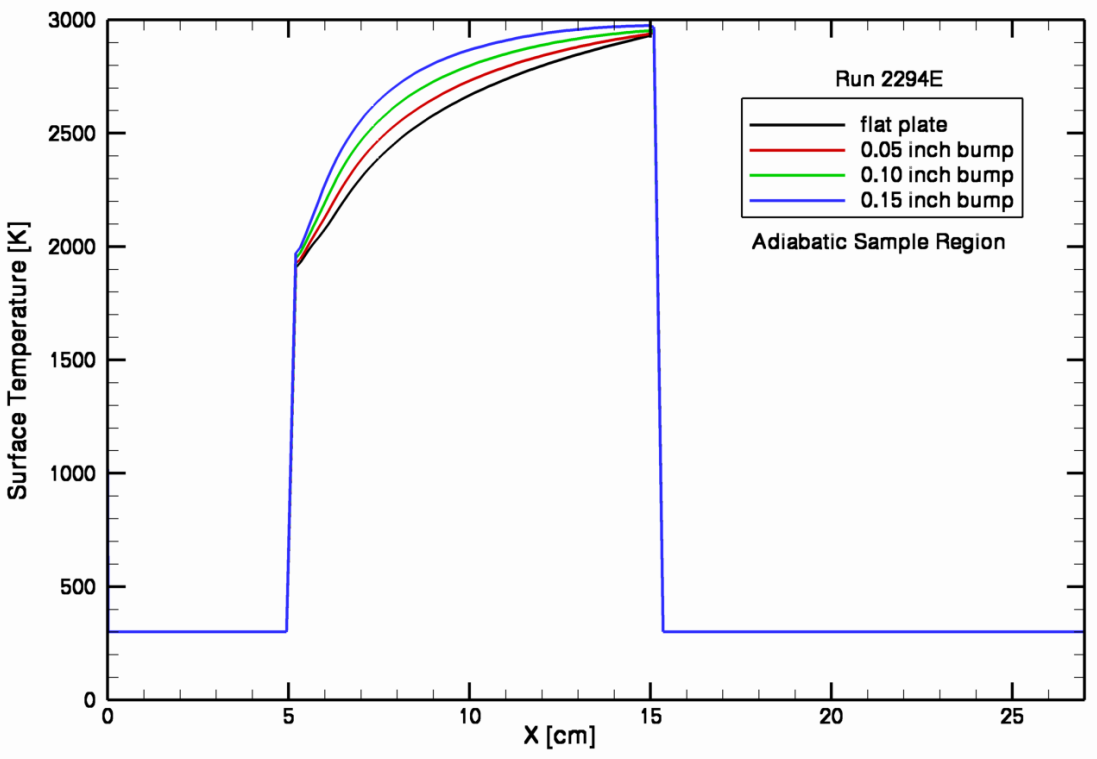

Figure 80: Run 2294E centerline adiabatic surface temperature sensitivity to bump height.

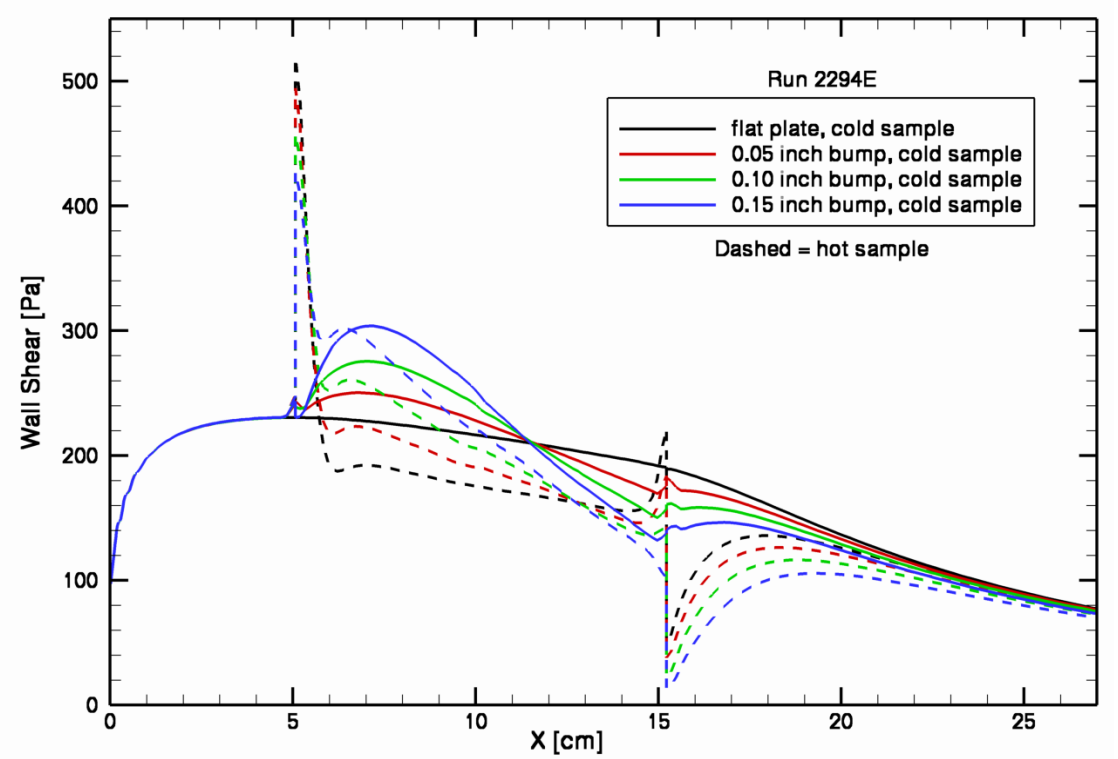

Figure 81: Run 2294E centerline wall shear sensitivity to wall temperature and bump height.

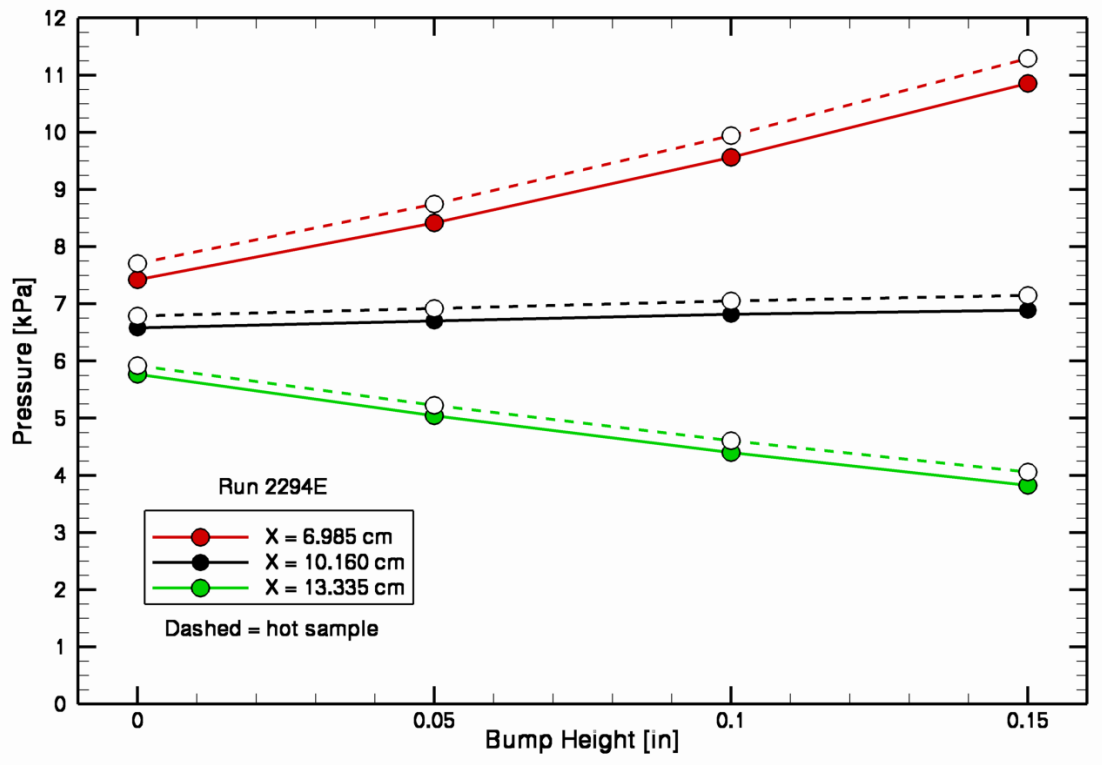

Figure 82: Run 2294E pressure sensitivity to wall temperature and bump height.

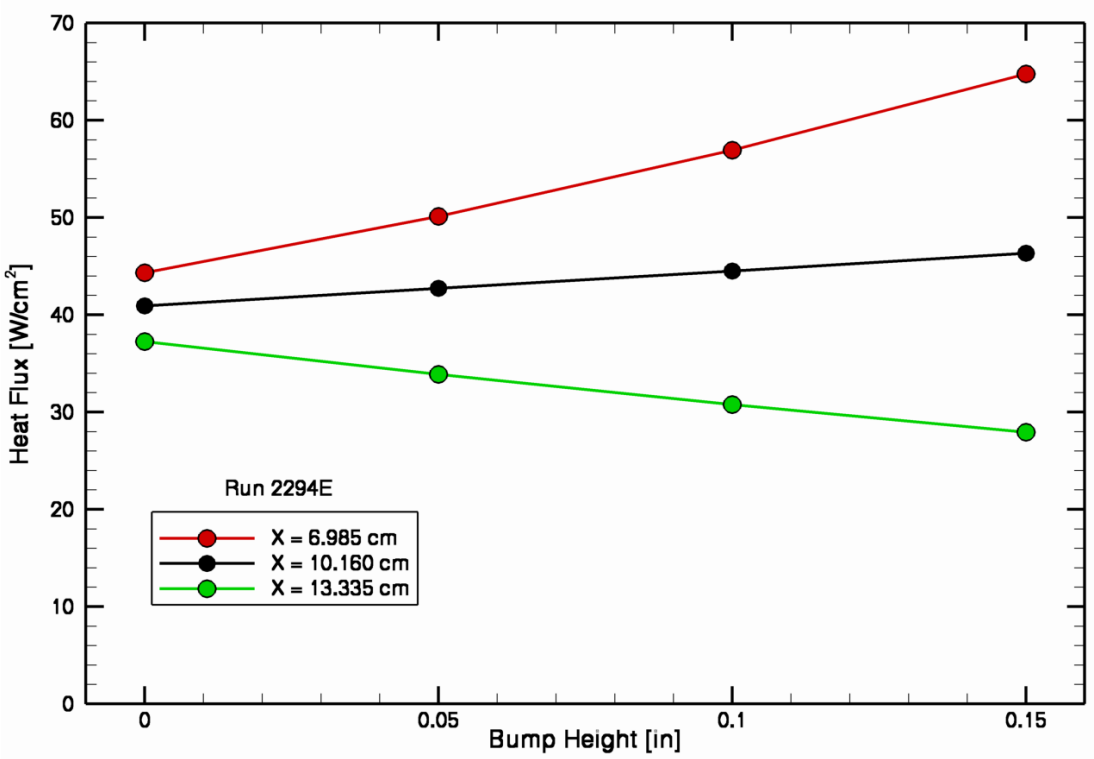

Figure 83: Run 2294E cold wall heat flux sensitivity to bump height.

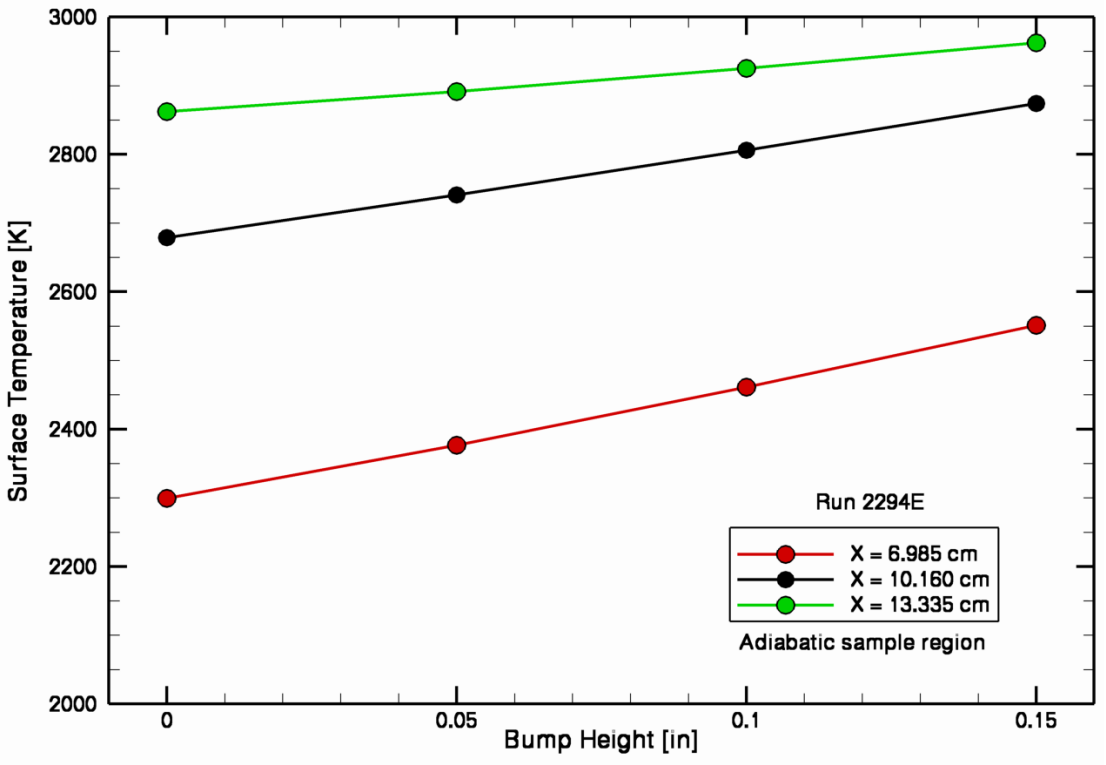

Figure 84: Run 2294E adiabatic surface temperature sensitivity to bump height.

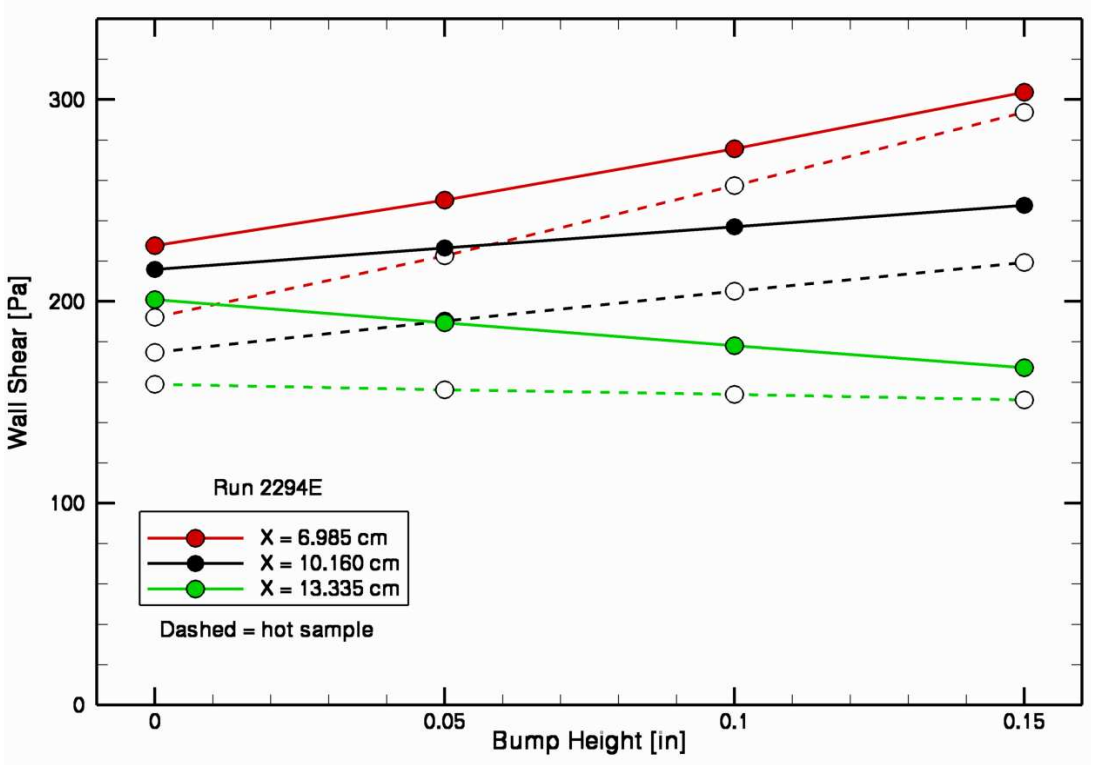

Figure 85: Run 2294E wall shear sensitivity to bump height.

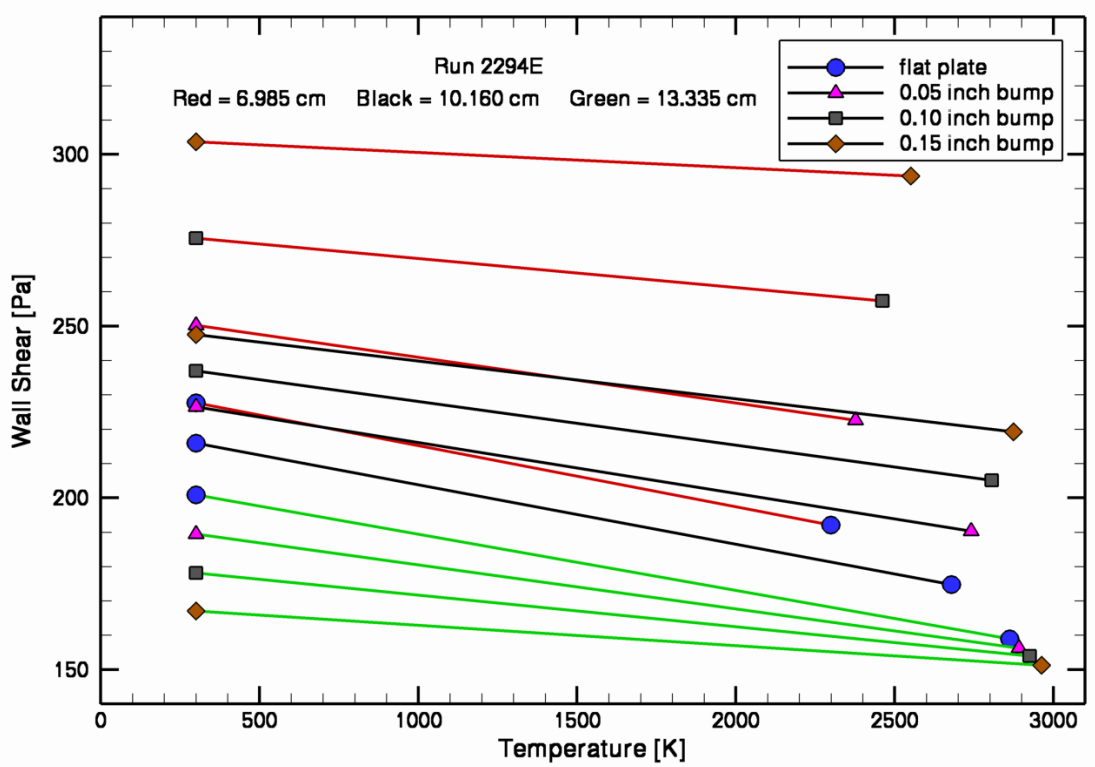

Figure 86: Run 2294E wall shear sensitivity to surface temperature.

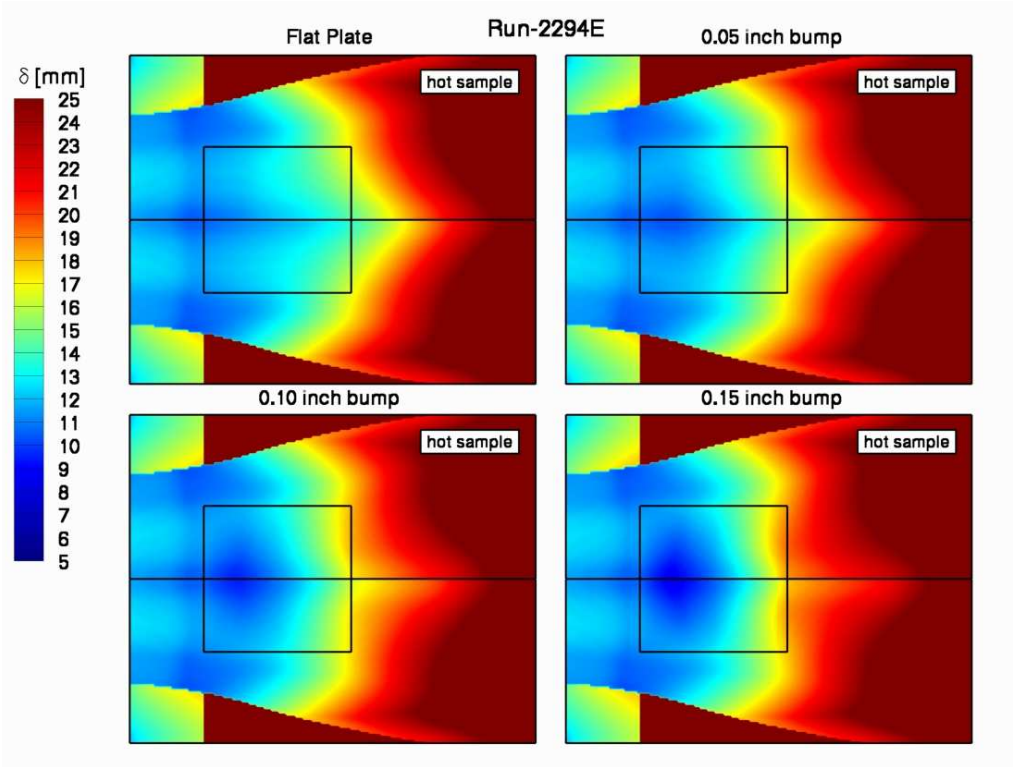

Figure 87: Run 2294E boundary layer thickness variation.

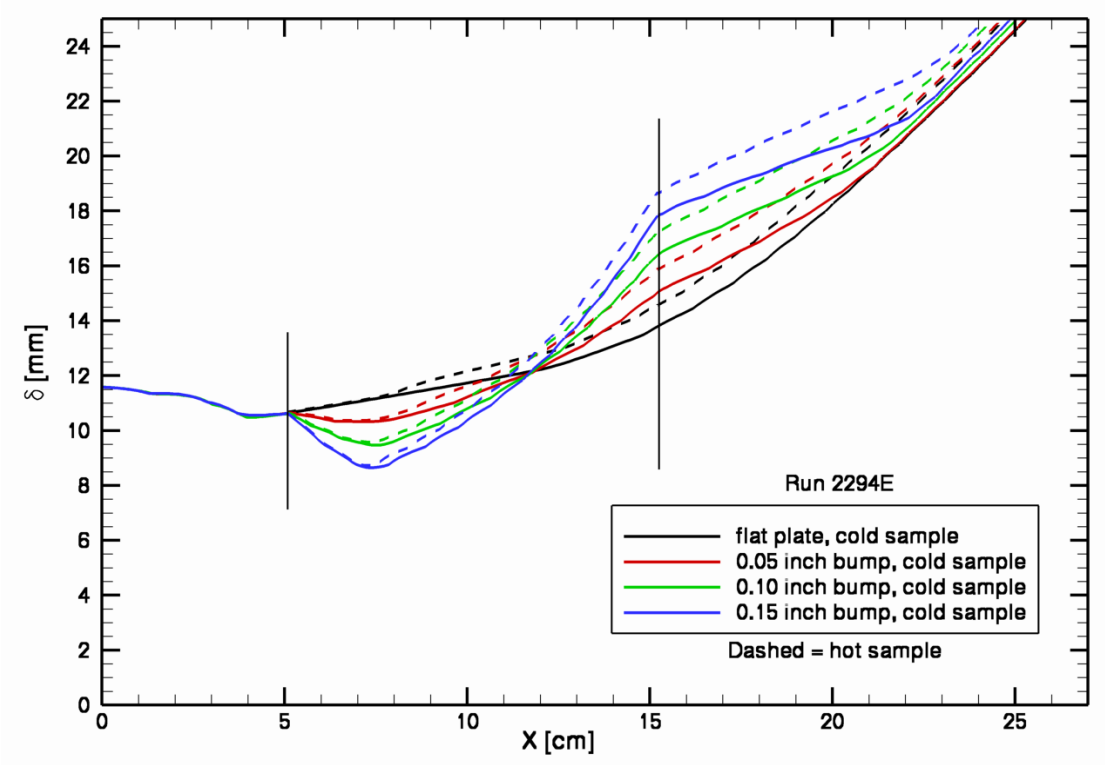

Figure 88: Run 2294E centerline boundary layer thickness comparison.

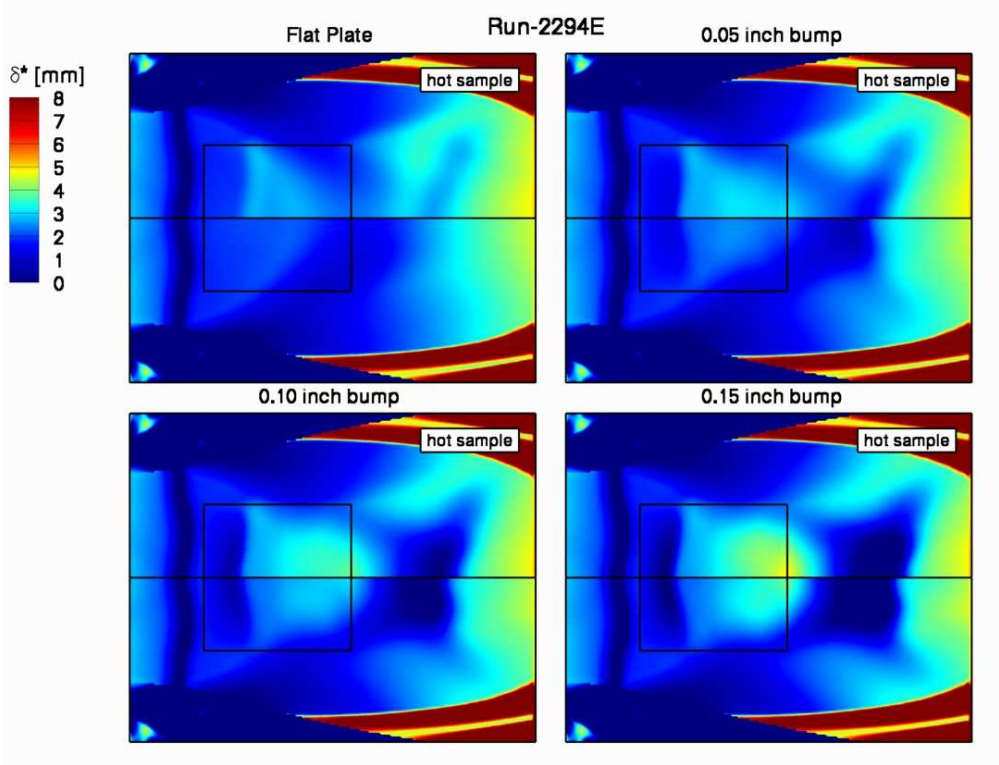

Figure 89: Run 2294E boundary layer displacement thickness variation.

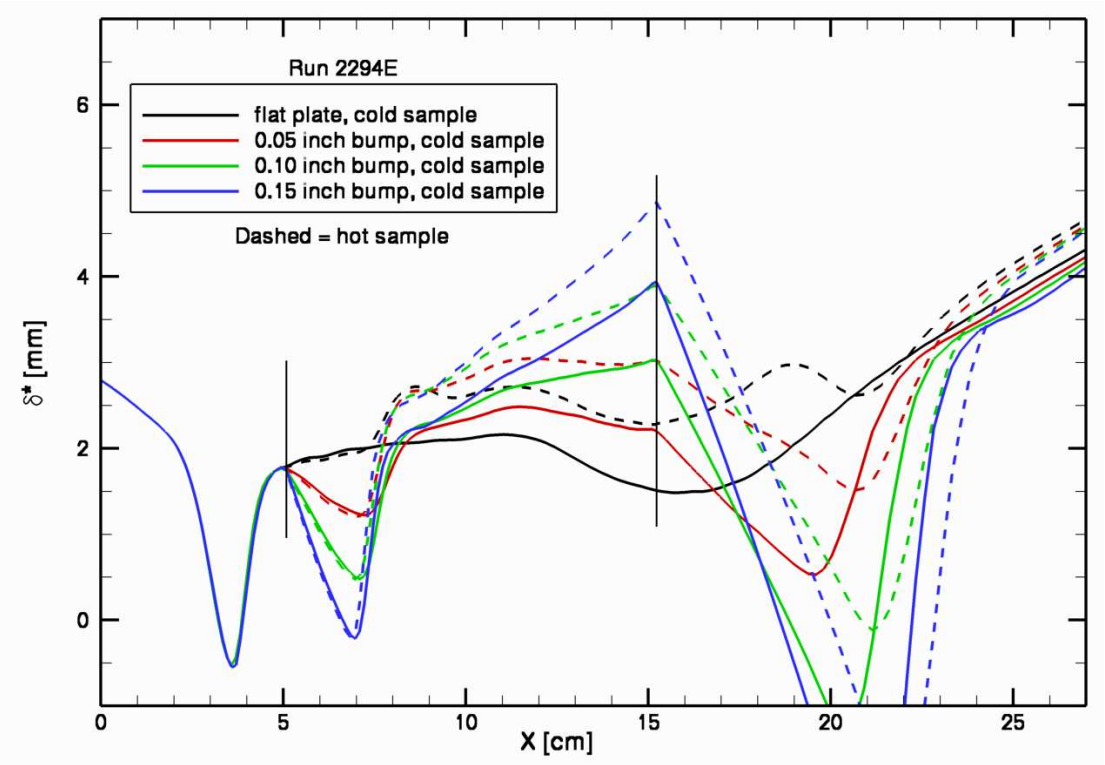

Figure 90: Run 2294E centerline boundary layer displacement thickness comparison.

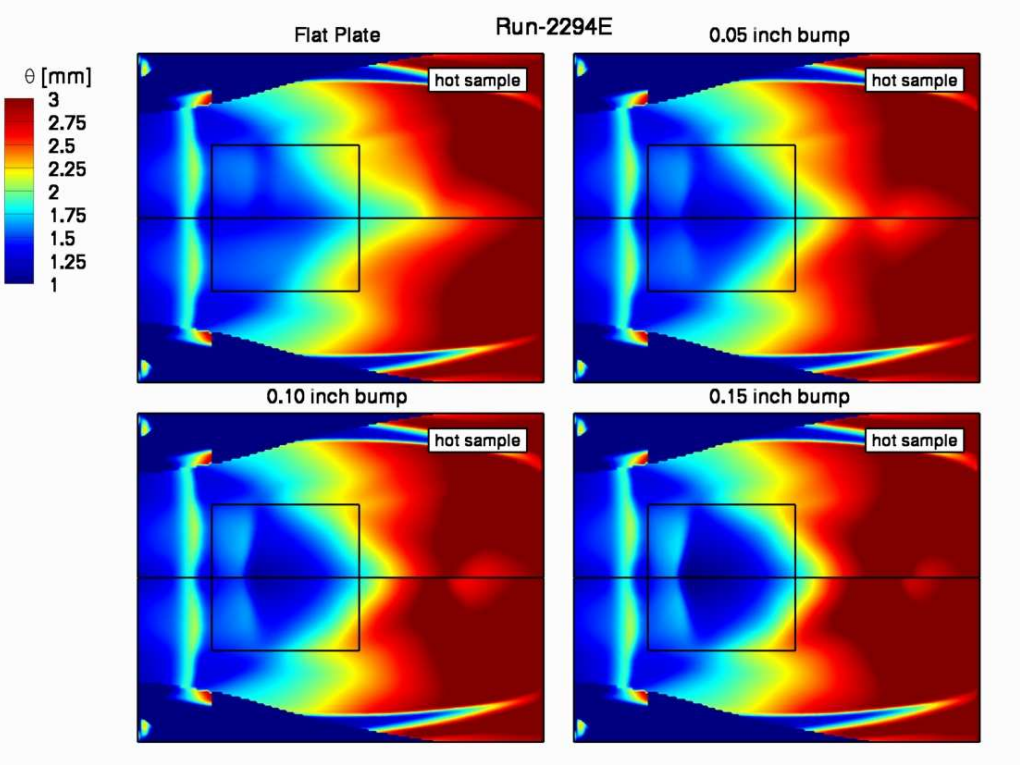

Figure 91: Run 2294E boundary layer momentum thickness variation.

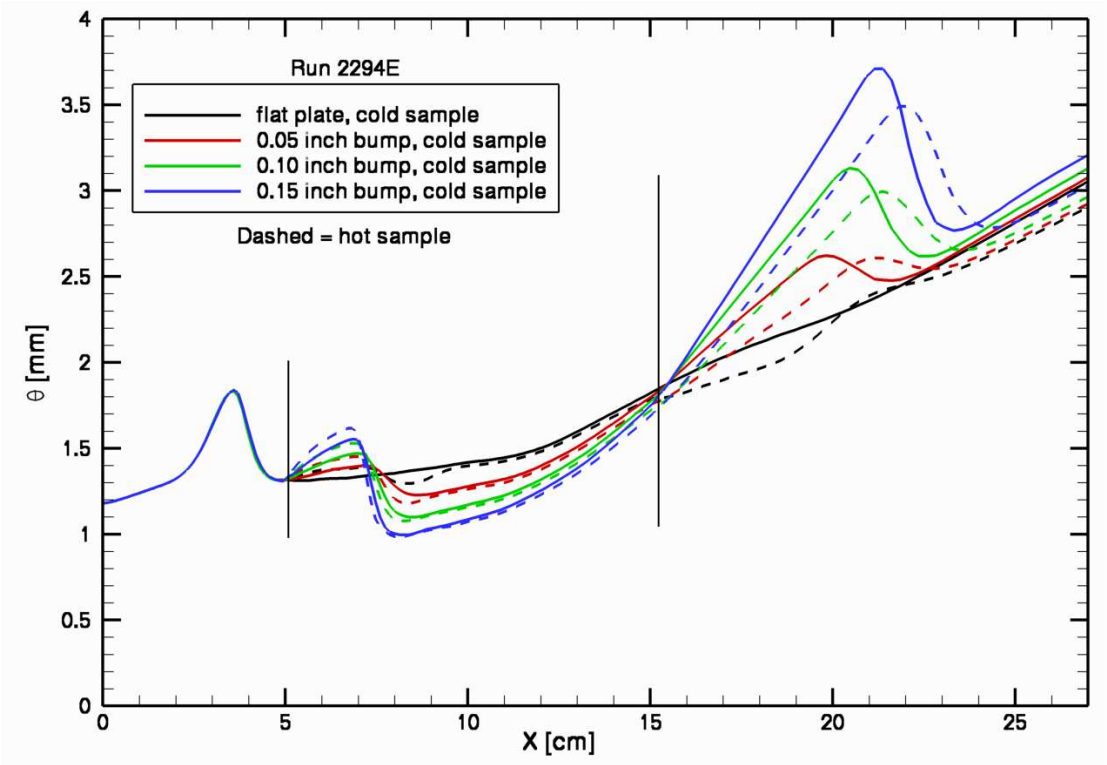

Figure 92: Run 2294E centerline boundary layer momentum thickness comparison.

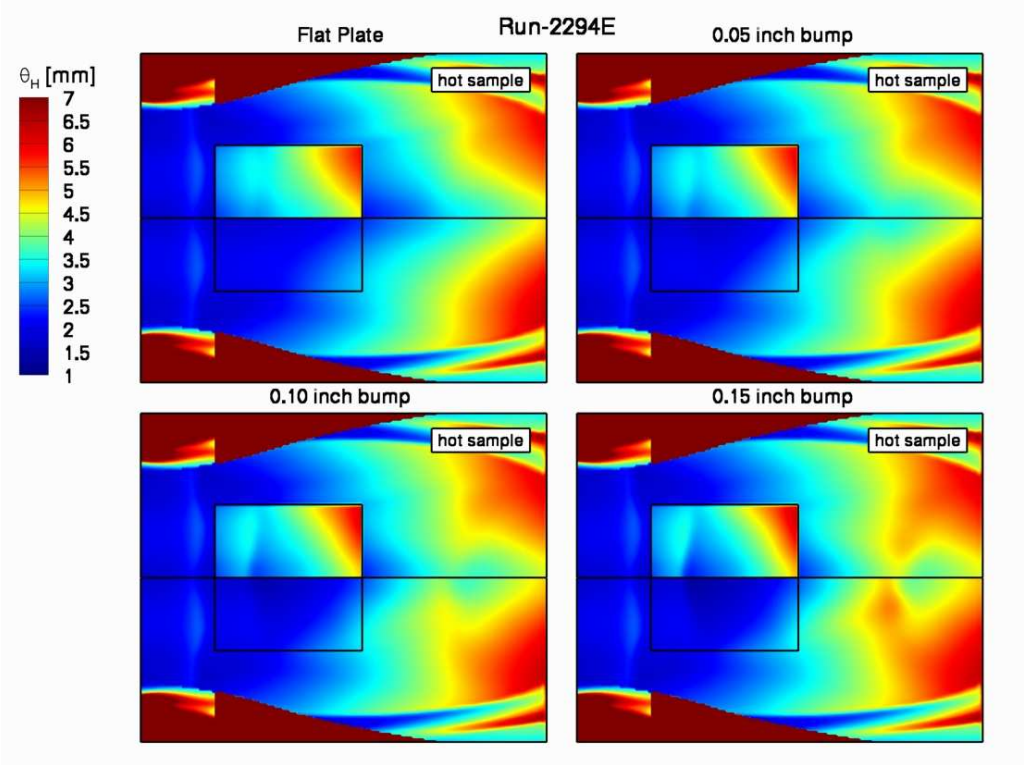

Figure 93: Run 2294E boundary layer enthalpy thickness variation.

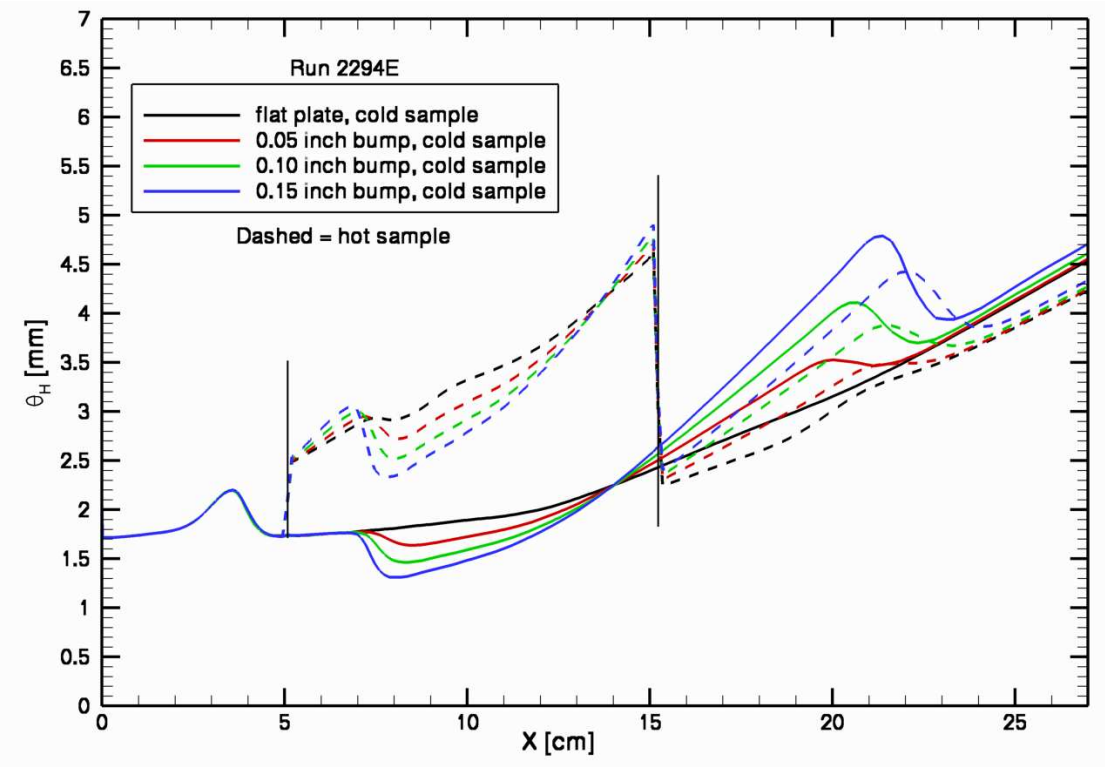

Figure 94: Run 2294E centerline boundary layer enthalpy thickness comparison.

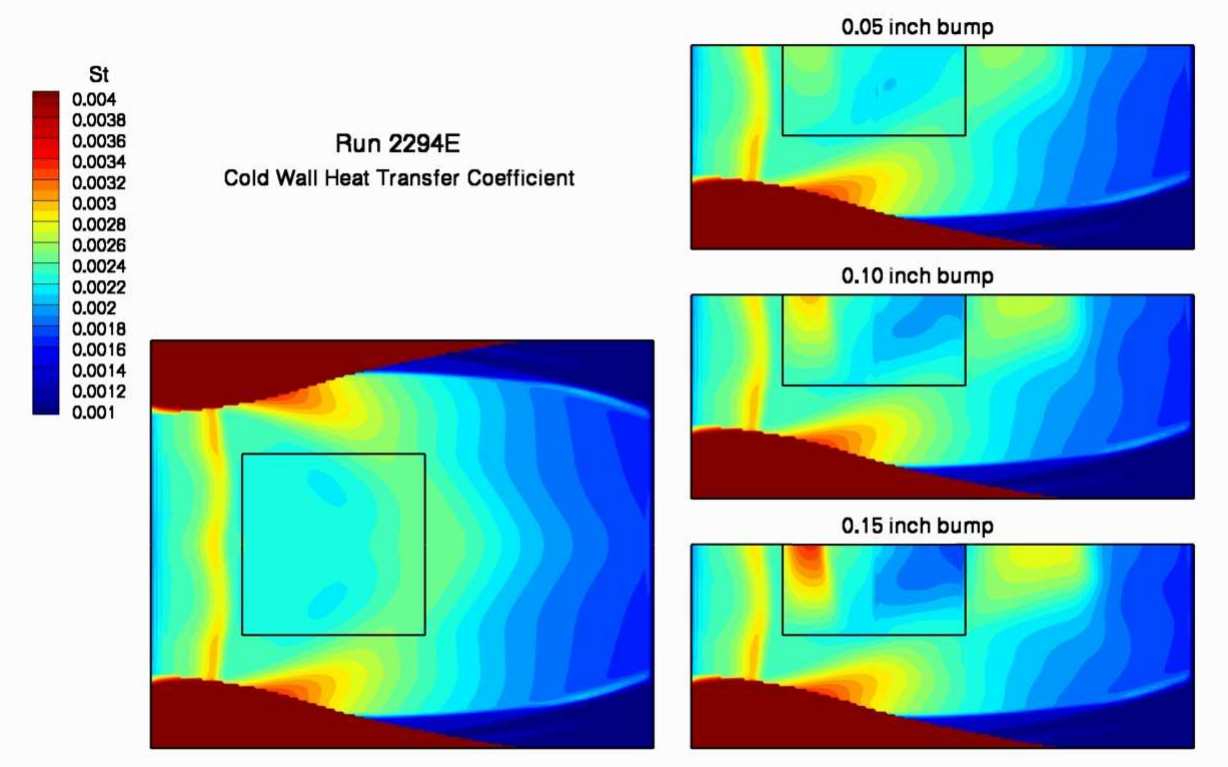

Figure 95: Run 2294E heat transfer coefficient variation.

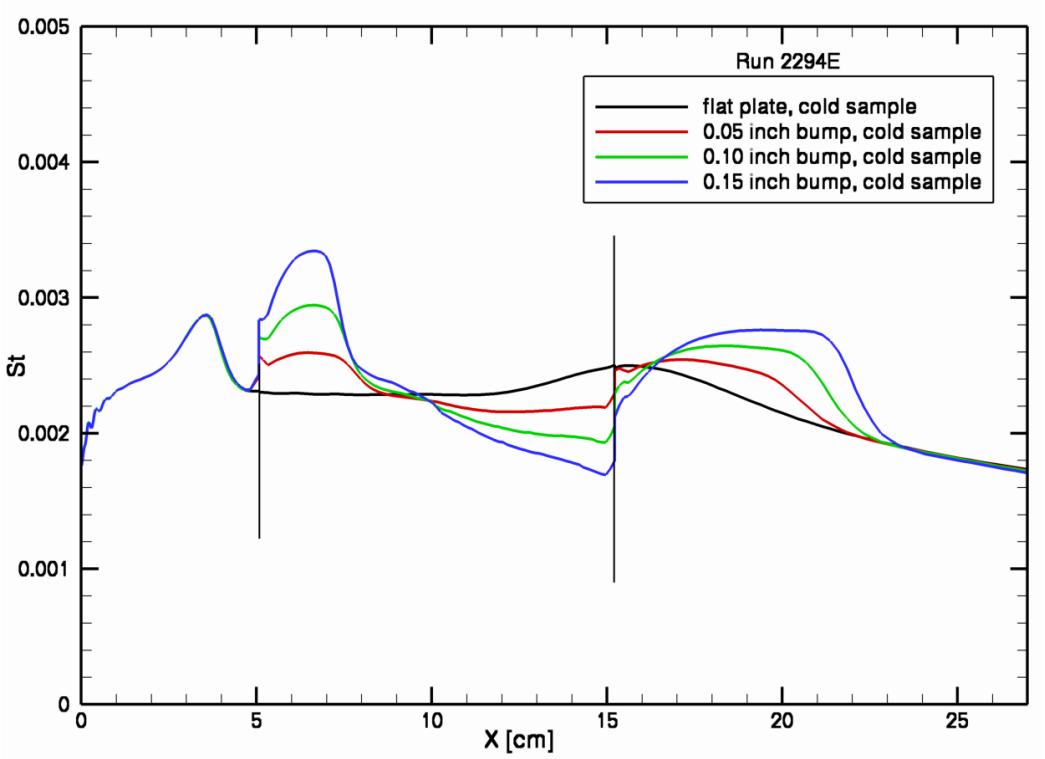

Figure 96: Run 2294E centerline heat transfer coefficient comparison.

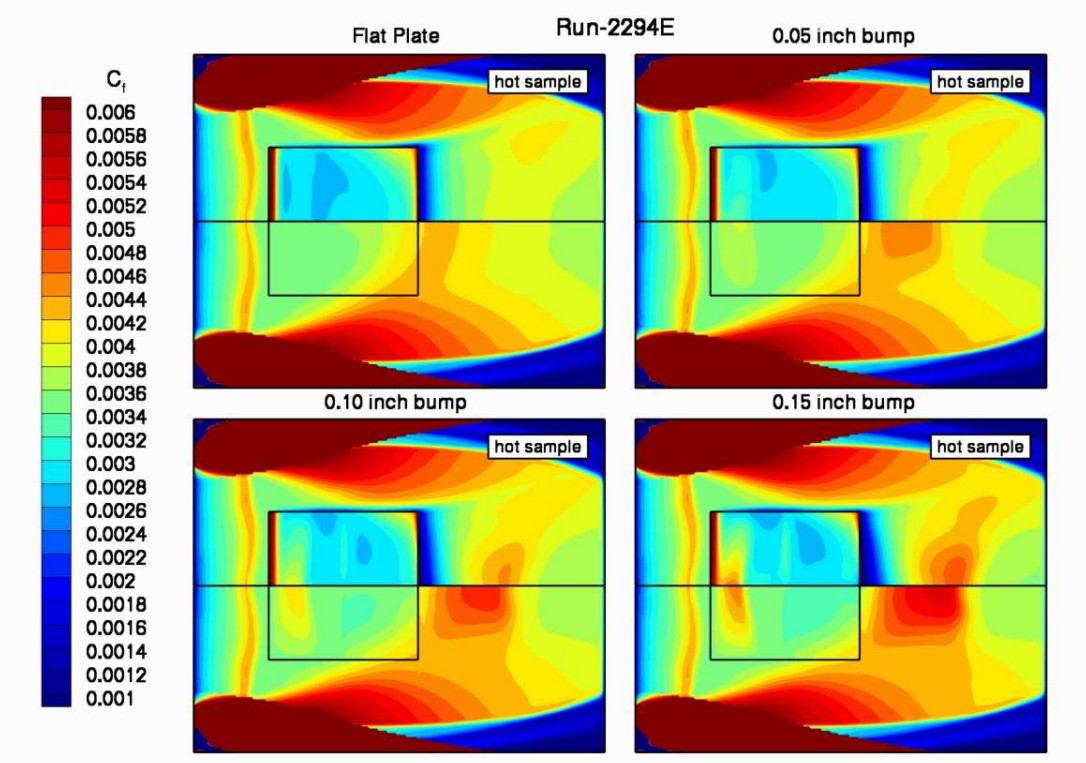

Figure 97: Run 2294E skin friction coefficient variation.

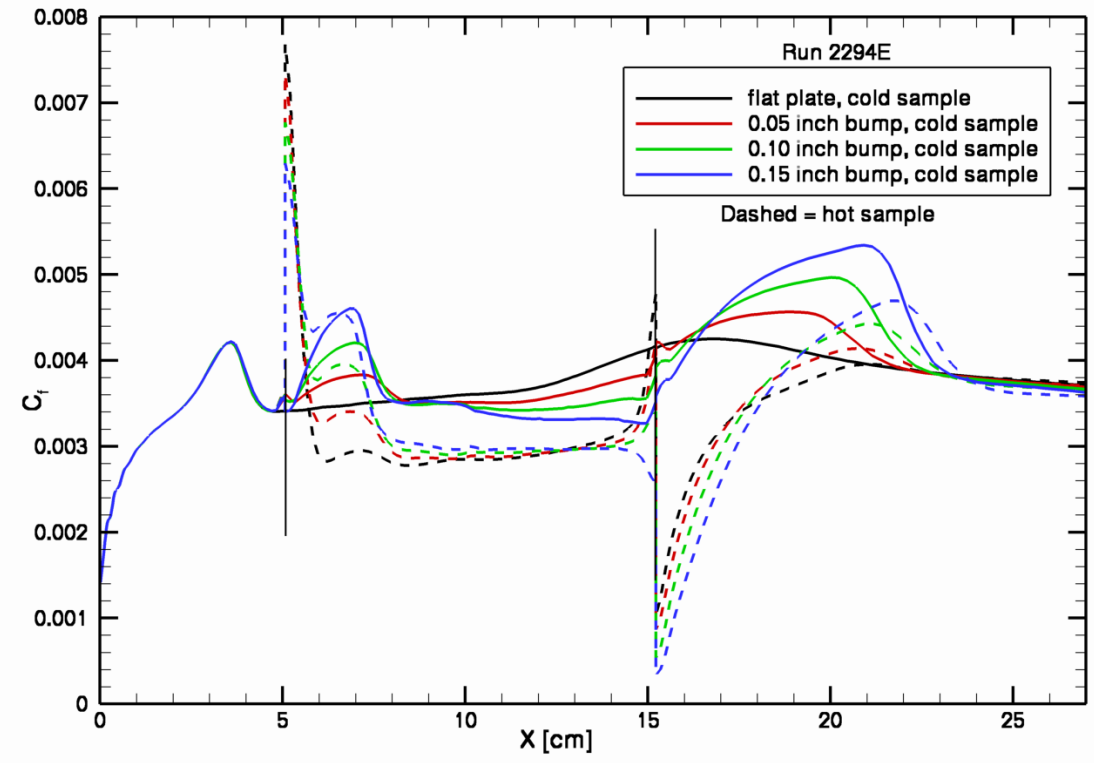

Figure 98: Run 2294E centerline skin friction coefficient comparison.

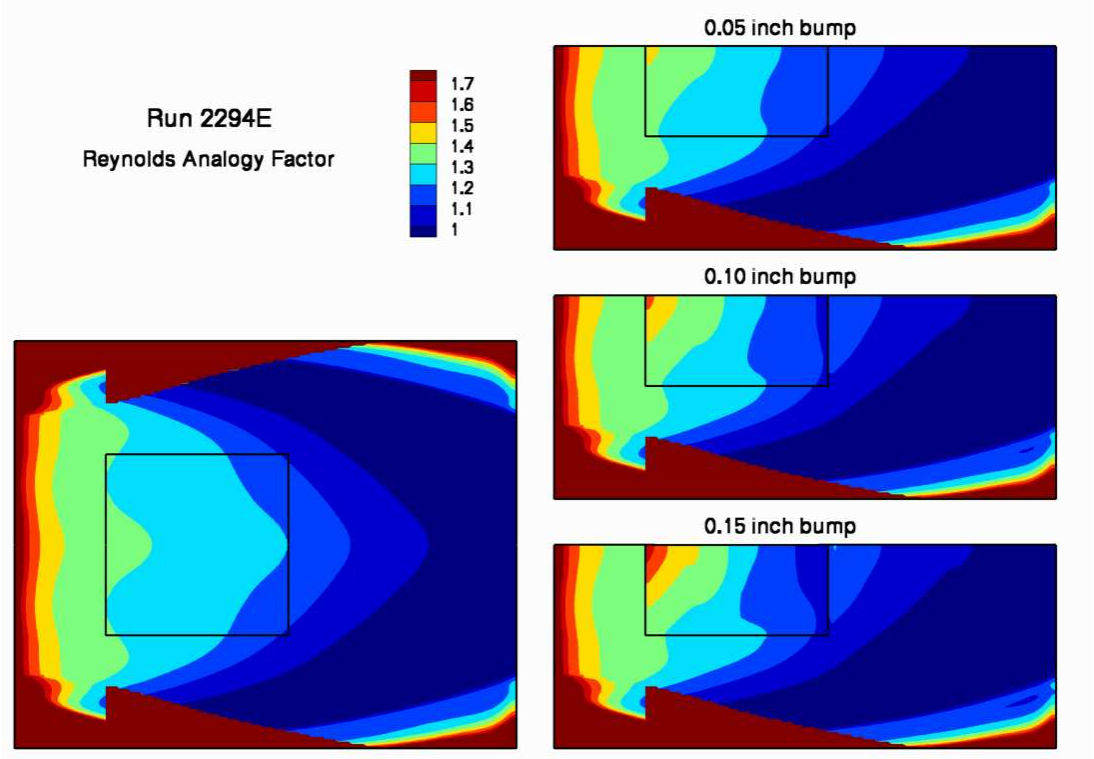

Figure 99: Run 2294E Reynolds analogy factor variation.

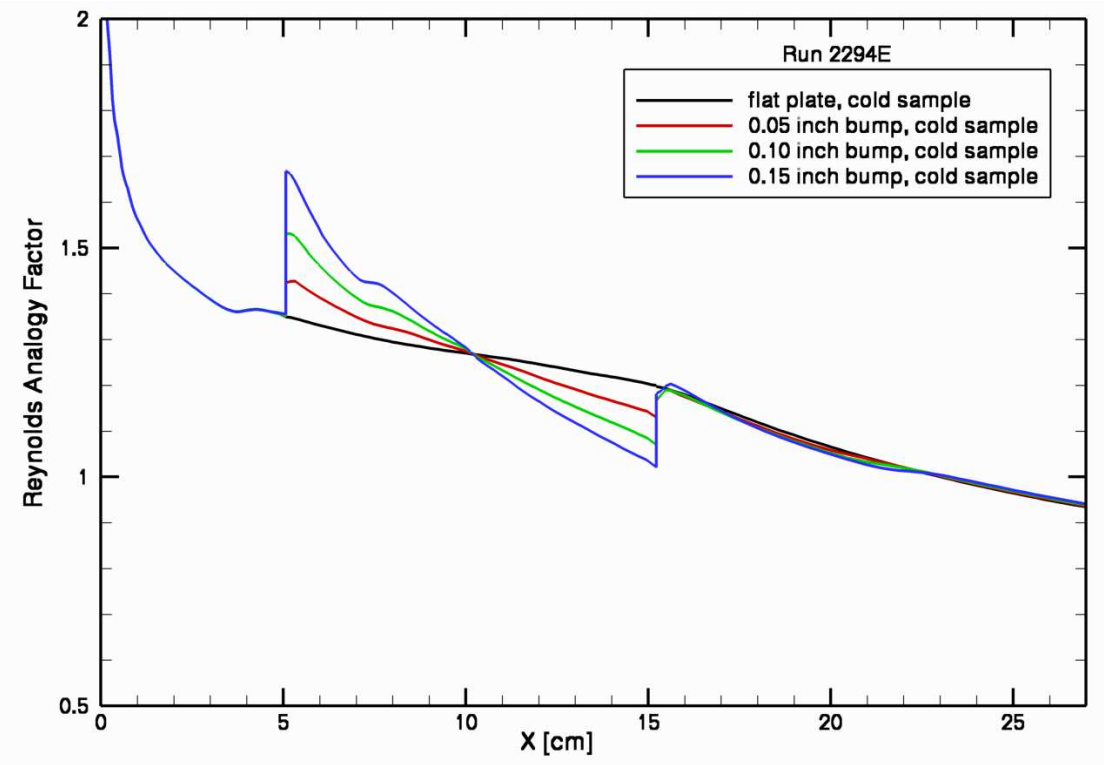

Figure 100: Run 2294E centerline Reynolds analogy factor comparison.

Run-to-Run Comparisons

Three test conditions were selected for computational analysis. One primary objective was to predict the surface shear at the center of the TPS sample area. In order to maximize confidence in the predicted shear, the experimental pressure and heat flux data from the center of the sample area were used to determine uniform facility nozzle plenum conditions. The matched pressure and heat flux along with the predicted shear are listed in Table 5.

Table 5: Computed cold wall results at the flat wall sample center.

Run	Pressure (kPa)	Heat Flux (W/cm^2)	Shear (Pa)
2294B	3.03	20.1	113
2294D	4.83	32.9	171
2294E	6.55	41.0	216

The pressure distributions down the centerline of the flat surface are compared in Figure 101. The CFD predicts a linearly decreasing pressure over the sample length for each test condition. The simulations were forced to match the center measurement. The low pressure experimental data suggests a lower slope, but still linear, pressure variation. The last pressure measurement for the two higher pressure conditions matches the CFD trend, but the first measurement indicates a pressure decrease compared to the center measurement. The current CFD analysis and results do not provide any insight as to what could cause a pressure increase down the centerline of the flat calibration plate.

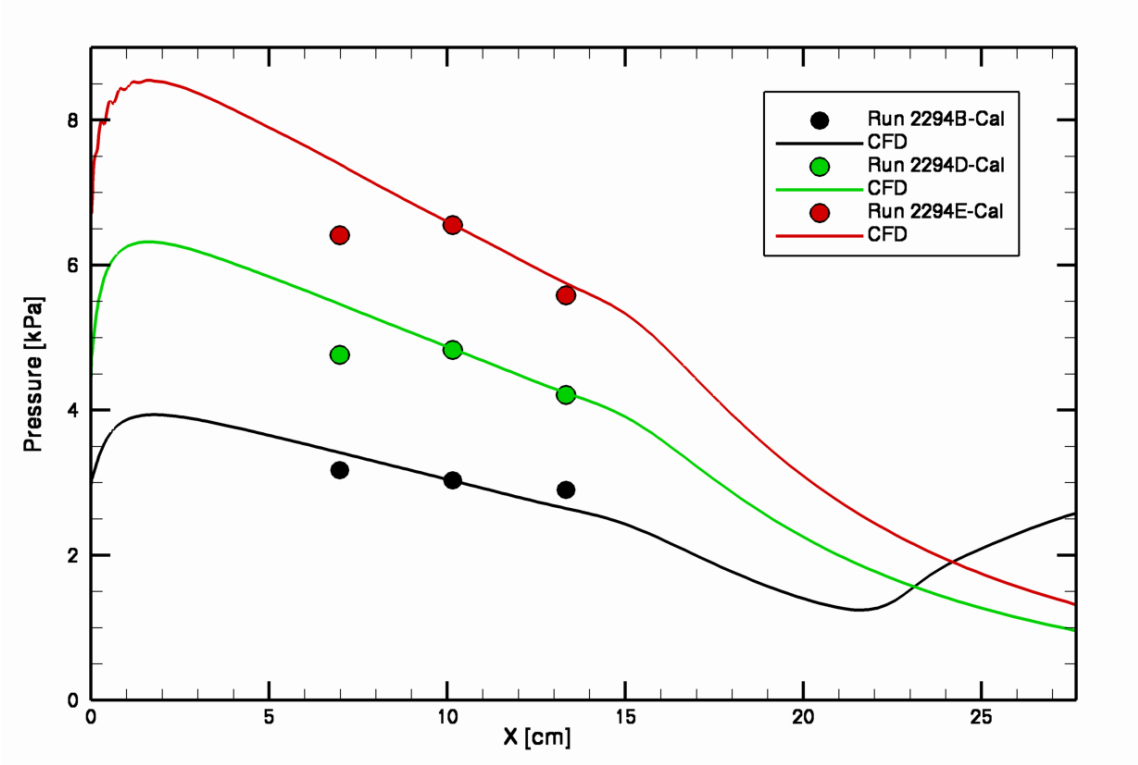

Figure 101: Centerline pressure comparison for the calibration plate (cold/flat).

The heat flux distributions down the centerline of the cold flat surface are compared in Figure 102. The CFD predicts a nearly linear decreasing heat flux over the sample length for each test condition. The simulations were forced to match the center measurement. The first heat flux measurement for the two higher heat flux conditions corroborates the pressure data in that it is less than the center measurement. The corresponding wall shear is plotted in Figure 103 and follows similar trends.

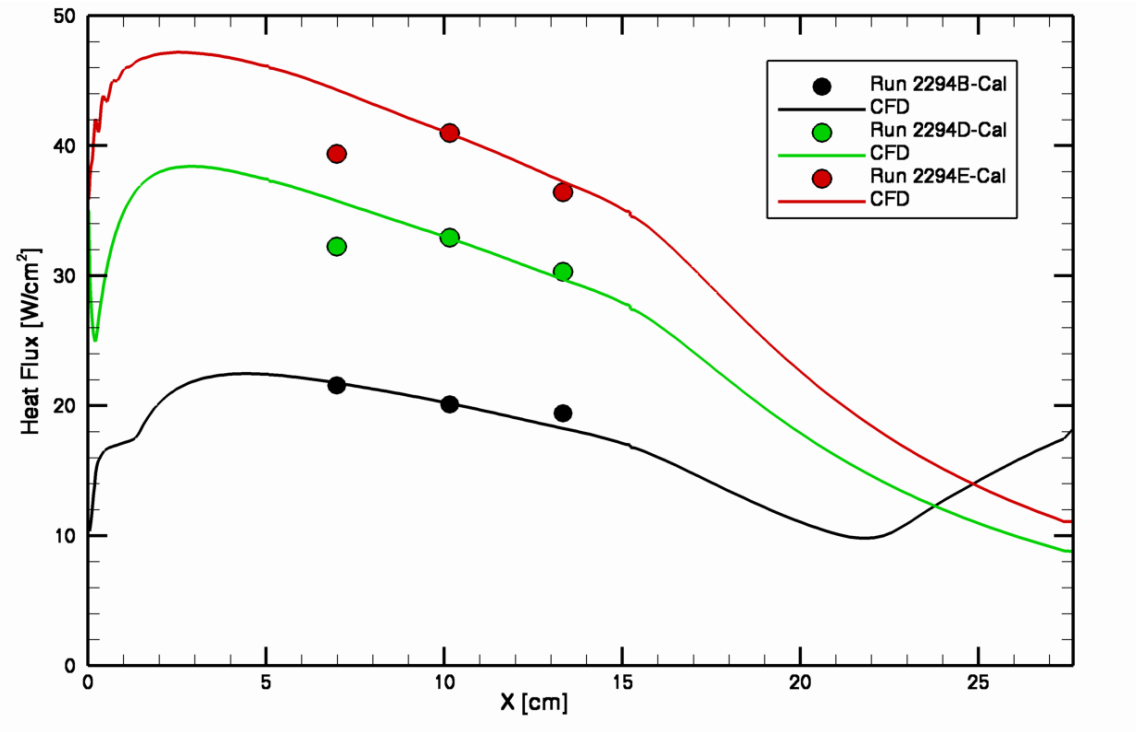

Figure 102: Centerline heat flux comparison for the calibration plate (cold/flat).

Boundary layer properties were extracted from each simulation. As shown in Figure 104, the boundary layer becomes slightly thinner as the test condition pressure increases. At the centerline the boundary layer thickness varies from 10.6 – 15.8 mm over the sample length for all test conditions. The displacement thickness variations along the centerline are included in Figure 105. Nearly the same displacement thickness is predicted for the two higher pressure test conditions. At these conditions, a displacement thickness of 2.2 mm is predicted at the center of the sample area. The momentum thickness and enthalpy thickness, Figures 106 and 107, follow trends similar to the boundary layer thickness over the length of the sample, but at a reduced value.

The cold wall heat flux and shear results were non-dimensionalized using locally varying boundary layer edge conditions. Figure 108 shows that the Stanton number trend with test condition is opposite to the heat transfer trend (compare to Figure 102) so that the highest heat transfer condition produces the lowest heat transfer coefficient over the sample length. The skin friction coefficient results show the same trend in Figure 109. However, calculation of a Reynolds analogy factor collapses these results to nearly a single curve. The low pressure test condition produces a slightly lower factor over the sample length. The average of all cases at the sample center is 1.26. Therefore, for similar test configurations, the shear can be inferred from heat transfer data without the need for additional CFD simulations.

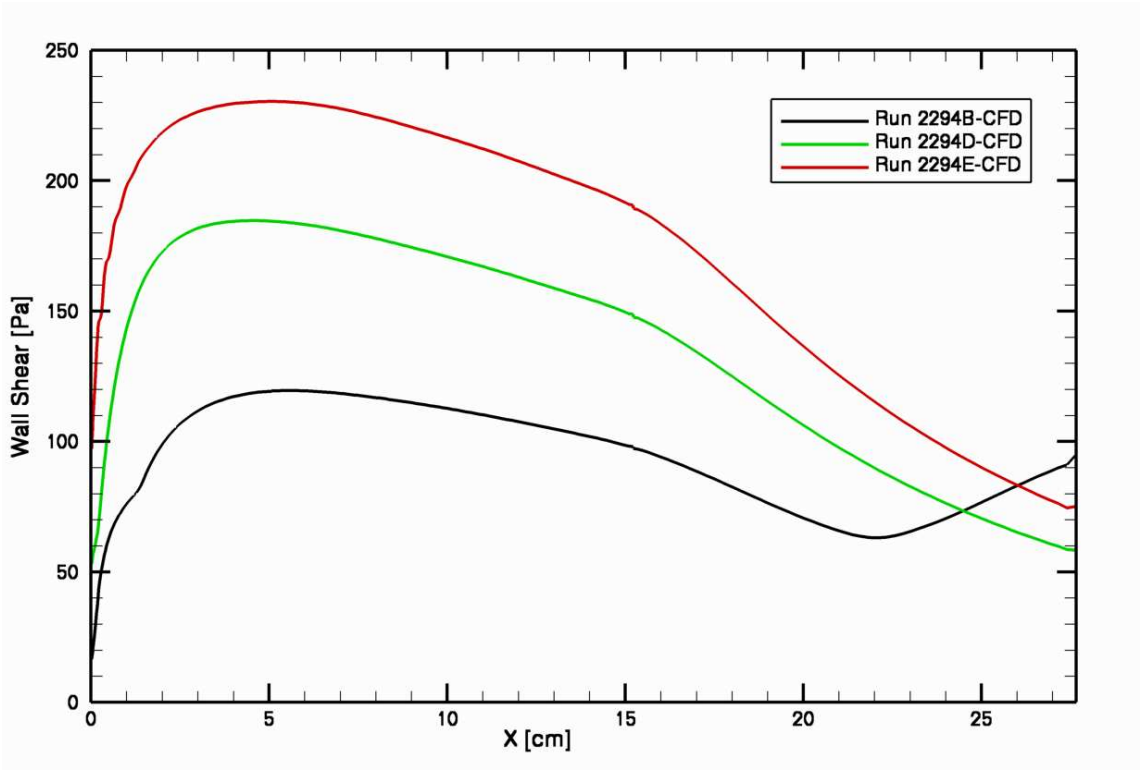

Figure 103: Centerline wall shear comparison for the calibration plate (cold/flat).

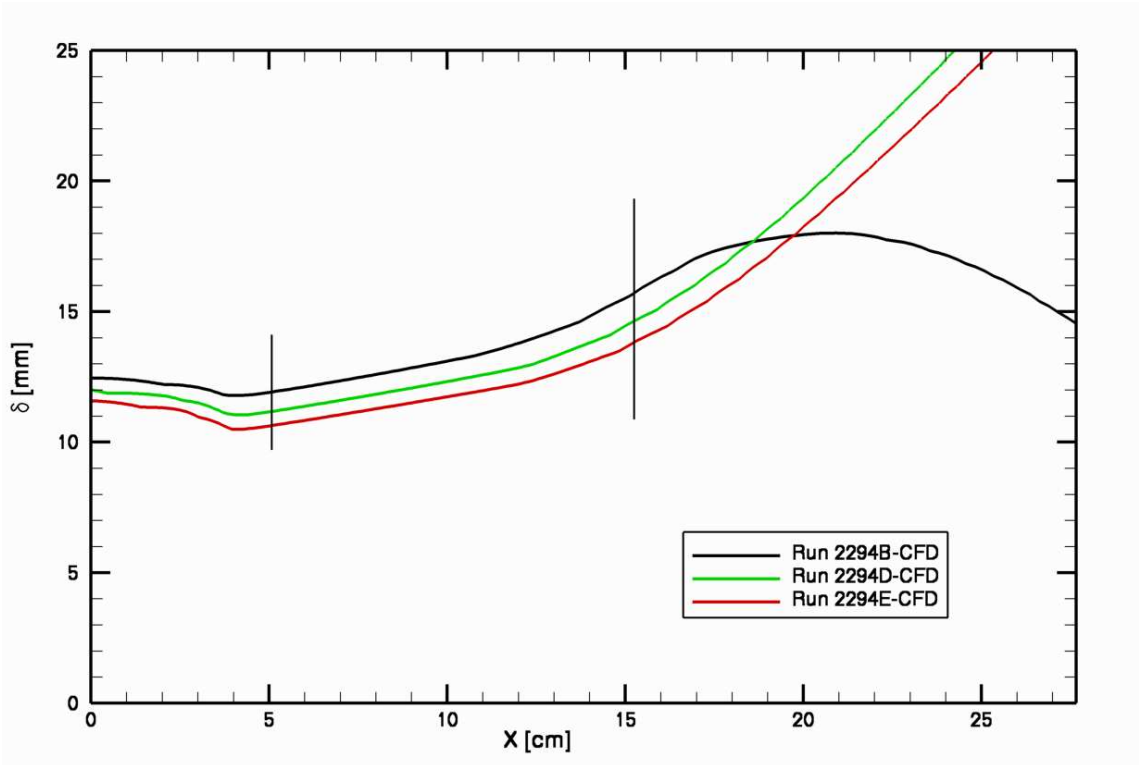

Figure 104: Centerline boundary layer thickness comparison for the calibration plate.

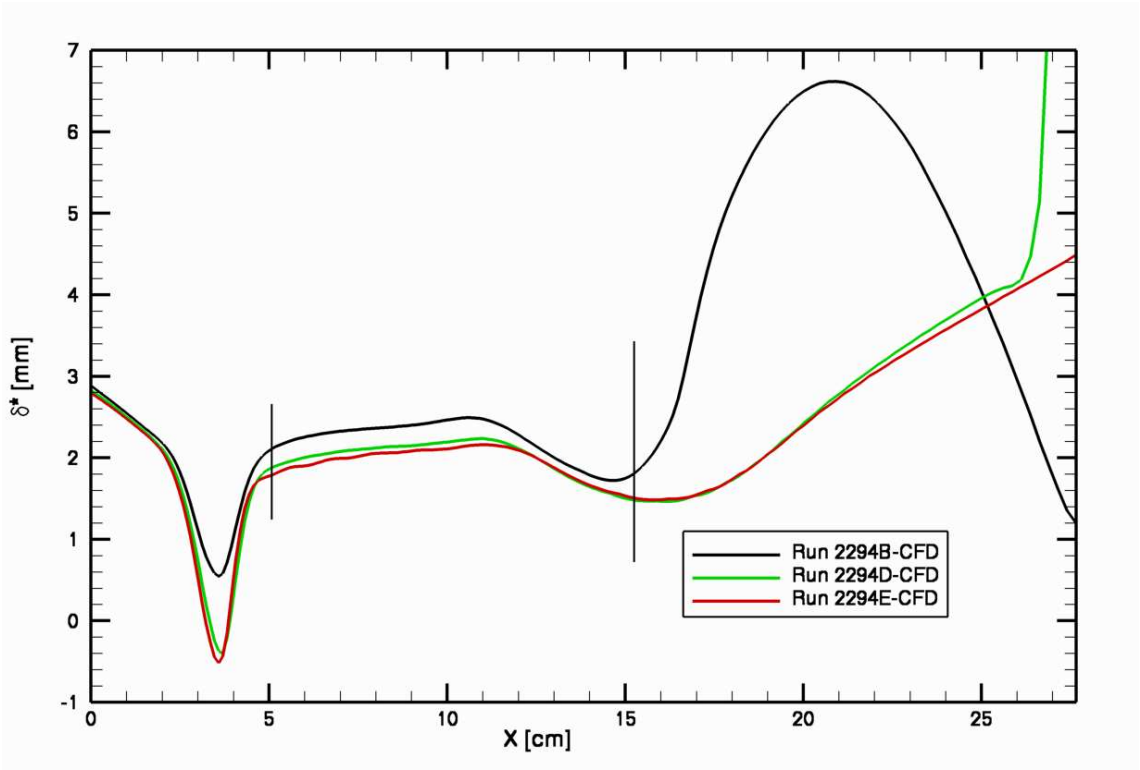

Figure 105: Centerline boundary layer displacement thickness comparison.

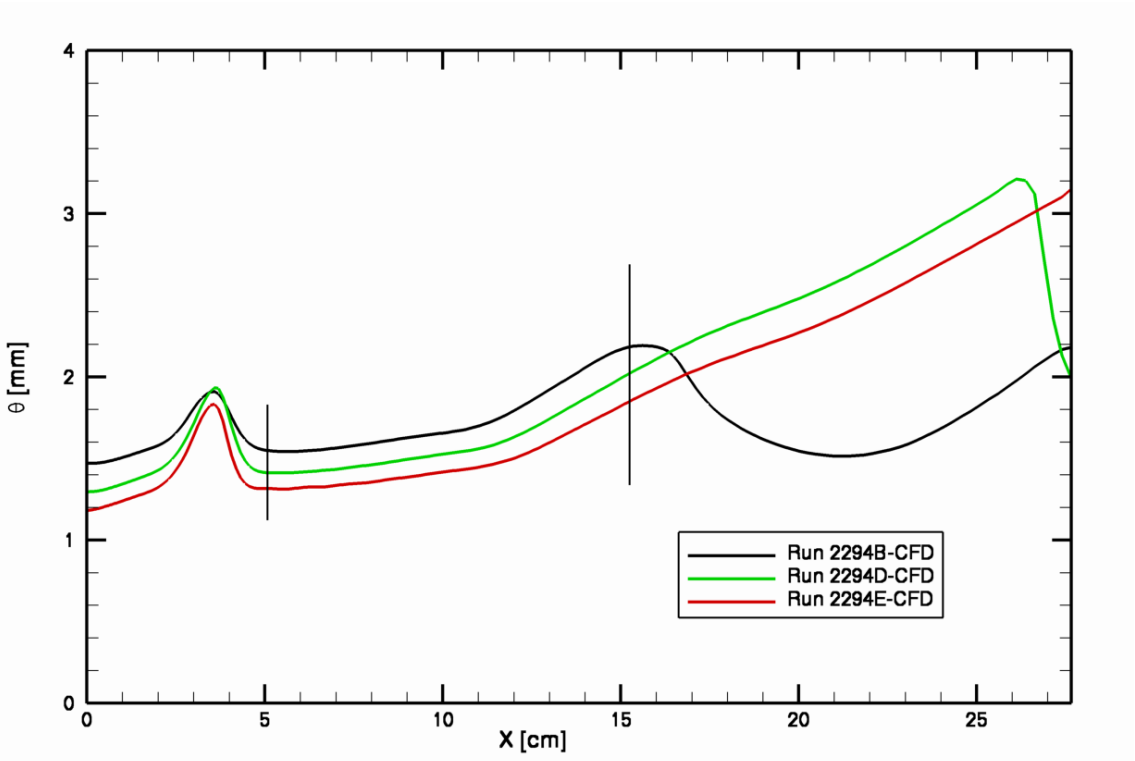

Figure 106: Centerline boundary layer momentum thickness comparison.

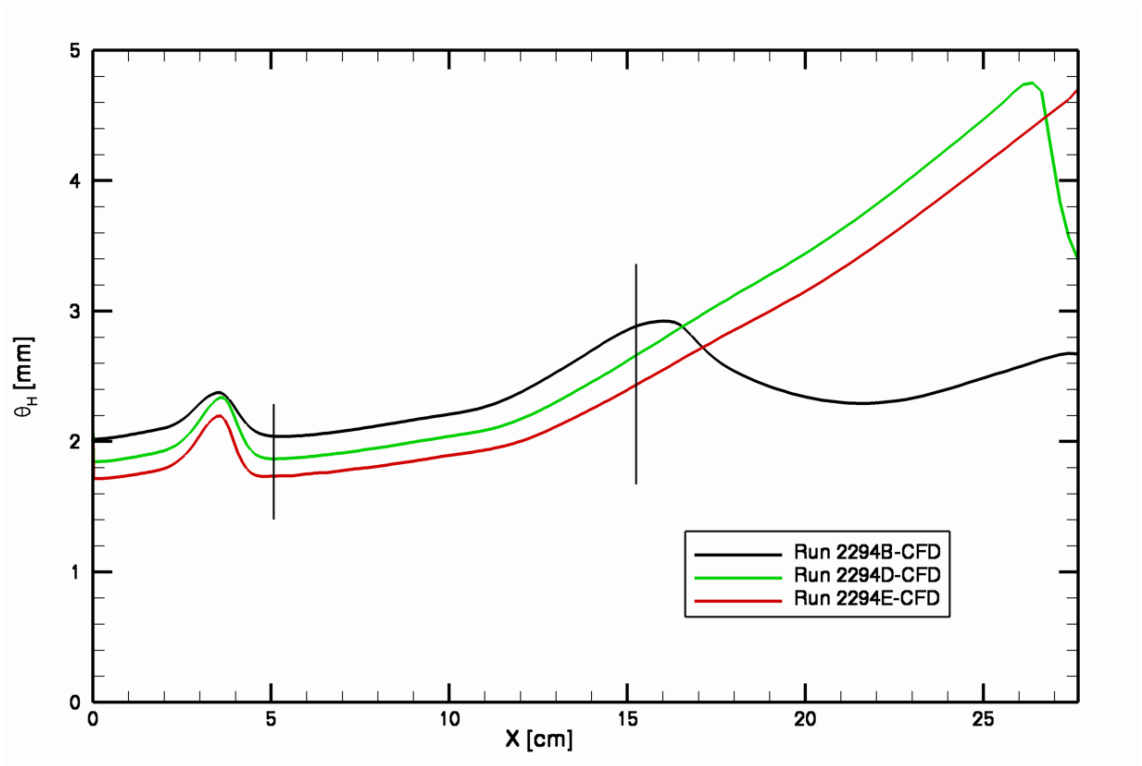

Figure 107: Centerline boundary layer enthalpy thickness comparison.

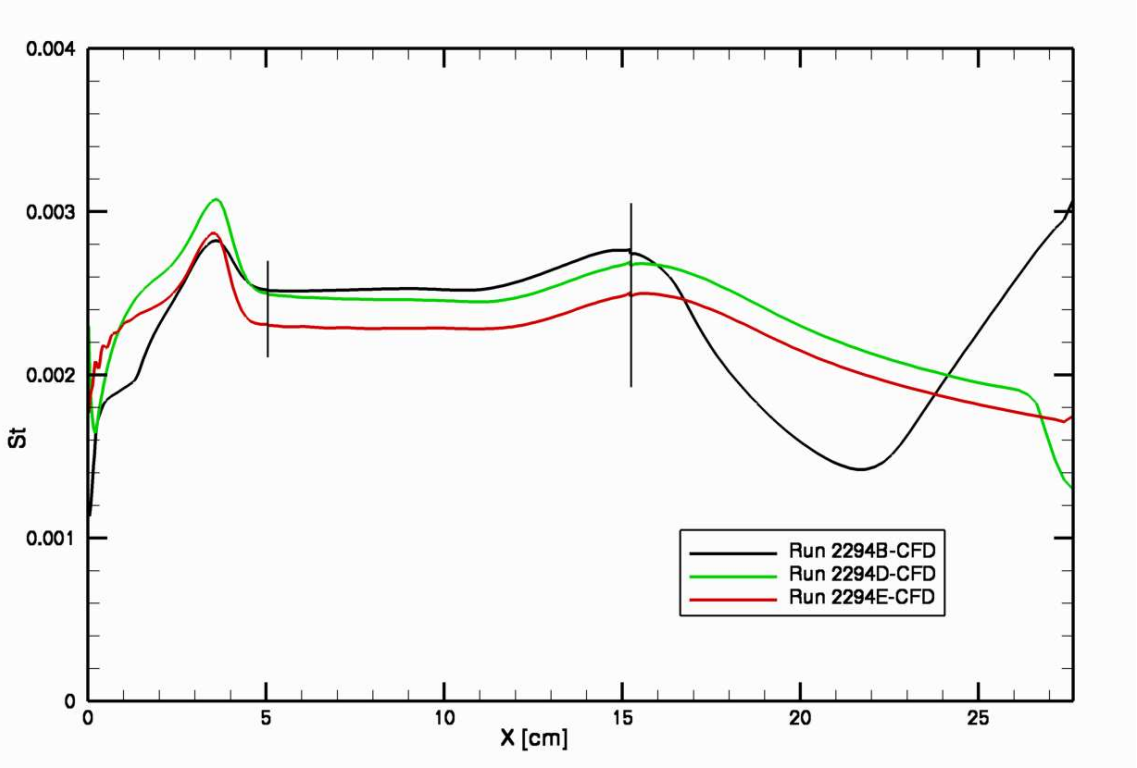

Figure 108: Centerline heat transfer coefficient comparison.

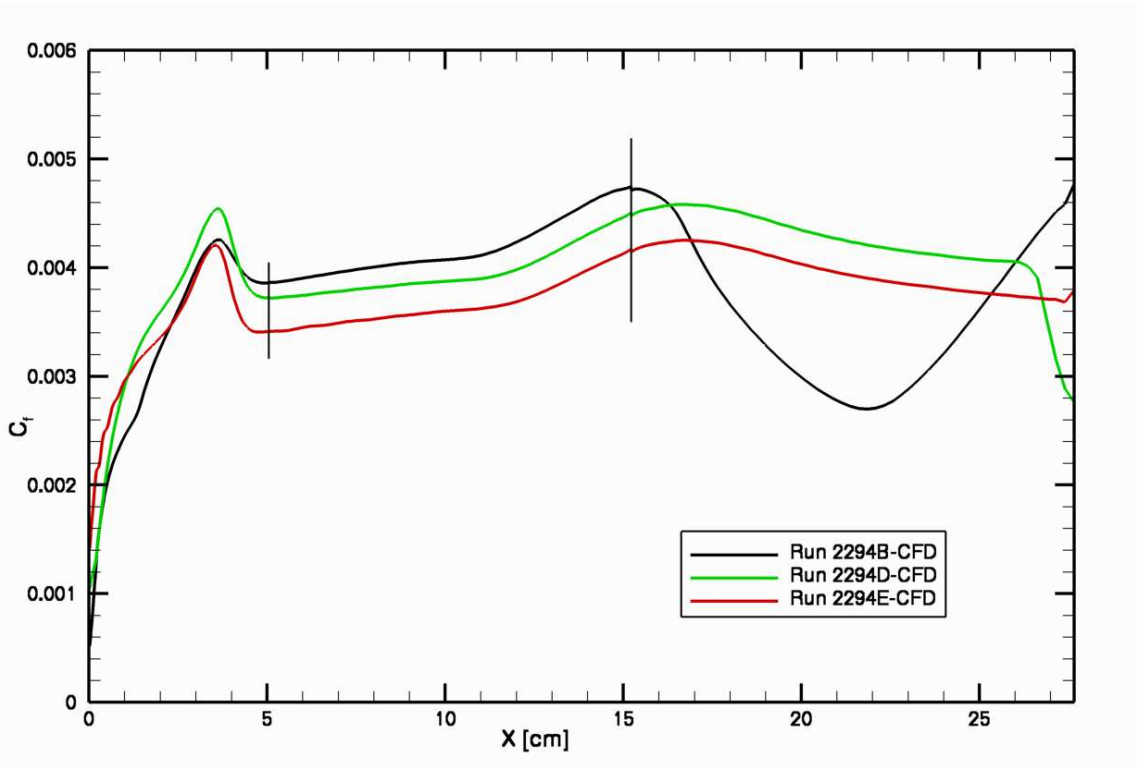

Figure 109: Centerline skin friction coefficient comparison.

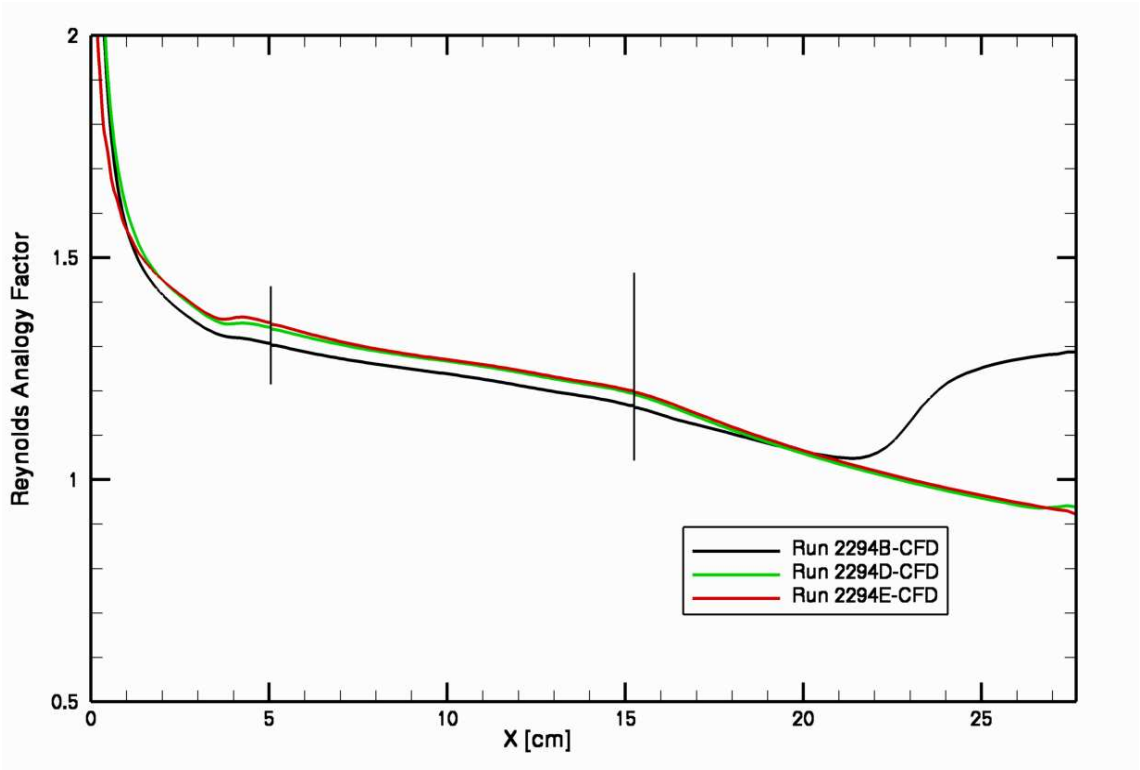

Figure 110: Centerline Reynolds analogy factor comparison.

Conclusions

The calibration plate center pressure and heat flux data from three test conditions were used to determine uniform facility nozzle plenum conditions for the current computational model of FTPS shear (wedge) testing in the LCAT facility. While the other eight pressure measurements and eight heat flux measurements for each test condition did not all follow the predicted trends of the current CFD simulations, the following conclusions are made:

1.) The plume from the LCAT semi-elliptical nozzle expansion section produced fairly uniform loads laterally to the FTPS sample area. Samples as wide as 5.5 inches could be tested.

2.) All loads were predicted to decrease significantly with streamwise distance. For example, the maximum pressure difference along the sample area centerline for Run 2294B (3.67 – 2.39 = 1.28 kPa) was 42% of the center pressure.

3.) At the center of the calibration plate the three test conditions produced the following pressure, heat flux, and wall shear loads: (3.03 kPa, 20.1 W/cm^2, 113 Pa), (4.83 kPa, 32.9 W/cm^2, 171 Pa), and (6.55 kPa, 41.0 W/cm^2, 216 Pa).

4.) A consistent Reynolds analogy factor of 1.26 at the center of the sample area could be used to infer the wall shear from heat flux data acquired at other similar test conditions.

Some of the FTPS samples have been observed to pillow out during testing. In order to investigate the resulting pressure, heat flux, and shear variation three bump geometries were created. These were 0.05, 0.10, and 0.15 inches tall at the center. The following affects were observed:

1.) While the pressure, heat flux, and wall shear at the center of the sample area were not strongly affected by bump size, the loads increased on the upstream side of the bump and decreased on the downstream side. This further increased the streamwise variation of each load.

2.) The existence of a bump also introduced a significant lateral variation to all quantities, particularly to the first half of the sample area.

3.) The predicted sample center Reynolds analogy factor was not affected by bump size.

An additional twelve simulations were performed to model the FTPS area with zero heat flux for each of the four geometries at each of the three test conditions. This resulted in the prediction of adiabatic surface temperature distributions for each case. Observations included:

1.) The peak predicted adiabatic surface temperature occurred at the end of the sample area along the centerline and was ~3000 degrees K.

2.) The hot surface temperature increased the pressure and decreased the shear compared to the specified cold wall results.

3.) A significant spike in shear was predicted at the surface temperature discontinuity at the sample area leading edge.

4.) The boundary layer enthalpy thickness increased significantly at the hotter surface temperature.

References

1 Hughes, S. J., Cheatwood, F. M., Dillman, R. A., Wright, H. S., Del Corso, J. A., Calomino, A. M., "Hypersonic Inflatable Aerodynamic Decelerator (HIAD) Technology Development Overview", AIAA 2011-2524, May 2011.

2 Del Corso, J. A., Cheatwood, F. M., Bruce III, W. E., Hughes, S. J., Calomino, A. M., "Advanced High-Temperature Flexible TPS for Inflatable Aerodynamic Decelerators", AIAA 2011-2510, May 2011.

3 Del Corso, J. A., Bruce III, W. E., Hughes, S. J., Dec, J. A., Rezin, M. D., Meador, M. B., Hiaquan, G., Fletcher, D. G., Calomino, A. M., Cheatwood, F.M., "Flexible Thermal Protection System Development for Hypersonic Inflatable Aerodynamic Decelerators", 9th International Planetary Probe Workshop, 16-22 June 2012, Toulouse, France.

4 Bruce III, W. E., Mesick, N. J., Ferlemann, P. G., Siemers III, P. M., Del Corso, J. A., Hughes, S. J., Tobin, S. A., Kardell, M. P., "Aerothermal Ground Testing of Flexible Thermal Protection Systems for Hypersonic Inflatable Aerodynamic Decelerators", 9th International Planetary Probe Workshop, 16-22 June 2012, Toulouse, France.

5 White, J. A., and Morisson, J. H., "Pseudo-Temporal Multi-Grid Relaxation Scheme for Solving the Parabolized Navier-Stokes Equations," AIAA Paper 99-3360, June 1999.

6 VULCAN, Ver. 6.1.1., http://vulcan-cfd.larc.nasa.gov/, NASA Langley Research Center, Hampton, VA, May 2012.

7 Pointwise Inc. http://www.pointwise.com/pw/, May 2012.

REPORT DOCUMENTATION PAGE

Form Approved
OMB No. 0704-0188

1. REPORT DATE *(DD-MM-YYYY)*	2. REPORT TYPE	3. DATES COVERED *(From - To)*
01- 05 - 2014	Contractor Report	

4. TITLE AND SUBTITLE

CFD Analysis of Flexible Thermal Protection System Shear Configuration Testing in the LCAT Facility

5a. CONTRACT NUMBER

NNL12AA09C

5b. GRANT NUMBER

5c. PROGRAM ELEMENT NUMBER

6. AUTHOR(S)

Ferlemann, Paul G.

5d. PROJECT NUMBER

5e. TASK NUMBER

5f. WORK UNIT NUMBER

475122.02.07.09

7. PERFORMING ORGANIZATION NAME(S) AND ADDRESS(ES)

NASA Langley Research Center
Hampton, Virginia 23681

8. PERFORMING ORGANIZATION REPORT NUMBER

9. SPONSORING/MONITORING AGENCY NAME(S) AND ADDRESS(ES)

National Aeronautics and Space Administration
Washington, DC 20546-0001

10. SPONSOR/MONITOR'S ACRONYM(S)

NASA

11. SPONSOR/MONITOR'S REPORT NUMBER(S)

NASA/CR-2014-218258

12. DISTRIBUTION/AVAILABILITY STATEMENT

Unclassified - Unlimited
Subject Category 31
Availability: NASA CASI (443) 757-5802

13. SUPPLEMENTARY NOTES

Langley Technical Monitor: Richard L. Gaffney, Jr.

14. ABSTRACT

This paper documents results of computational analysis performed after flexible thermal protection system shear configuration testing in the LCAT facility. The primary objectives were to predict the shear force on the sample and the sensitivity of all surface properties to the shape of the sample. Bumps of 0.05, 0.10,and 0.15 inches were created to approximate the shape of some fabric samples during testing. A large amount of information was extracted from the CFD solutions for comparison between runs and also current or future flight simulations.

15. SUBJECT TERMS

Computational fluid dynamics; HIAD; Surface properties; Thermal protection

16. SECURITY CLASSIFICATION OF:			17. LIMITATION OF ABSTRACT	18. NUMBER OF PAGES	19a. NAME OF RESPONSIBLE PERSON
a. REPORT	b. ABSTRACT	c. THIS PAGE			STI Help Desk (email: help@sti.nasa.gov)
					19b. TELEPHONE NUMBER *(Include area code)*
U	U	U	UU	72	(443) 757-5802